DOI: 10.2478/ata-2021-0001



Acta Technologica Agriculturae 1
Nitra, Slovaca Universitas Agriculturae Nitriae, 2021, pp. 1–7

# PERFORMANCE OPTIMIZATION OF GROUNDNUT SHELLING USING RESPONSE SURFACE METHODOLOGY

Aliyu Idris MUHAMMAD[1, 2]*, Moshud ISIAKA[3], Muhammed Lawal ATTANDA[2], Sarafadeen Kolawole SHITTU[2], Ibrahim LAWAN[2], Muhammad Isa BOMOI[4]

[1]Zhejiang University, Hangzhou, China
[2]Bayero University Kano, Kano, Nigeria
[3]Ahmadu Bello University, Zaria, Nigeria
[4]Federal Ministry of Science and Technology, Abuja, Nigeria

This study evaluated the influence of drum speed, moisture content, and feed rate on the performance indices of groundnut sheller using Ex-Dakar groundnut variety. Response surface methodology was used to study the influence of input variables and optimize the processing conditions. The developed second-order polynomial model adequately described the performance responses, including output capacity, shelling and cleaning efficiencies, and kernel damage. The input variables indicated significant influences on performance responses. The optimized processing variables for the responses were drum speed of 210 rpm, moisture content of 8%, and feed rate of 350 kg·h$^{-1}$. The optimum responses obtained were output capacity of 302.52 kg·h$^{-1}$, shelling efficiency of 97.61%, cleaning efficiency of 53.16%, and kernel damage of 4.04%. These performance responses were validated experimentally and were close to the observed results.

**Keywords:** Box-Behnken design; optimum responses; performance evaluation; groundnut processing

Population growth has resulted in the development of indigenous technologies at small and medium scale levels to boost agricultural production. This led to the development and modification of various technologies, such as groundnut shellers. Groundnut (*Arachis hypogaea*), or peanut, is a leguminous crop grown for its edible seeds, oil, and protein-rich kernels (Muhammad et al., 2015). In the last decade, the demand for groundnut has increased to 47.1 million tons within an area of 2.8 million hectares due to domestic and industrial usage (Pandit et al., 2020). However, its processing is still practiced using traditional methods of hand shelling or beating the groundnut heap with sticks on hard ground surfaces. These methods are associated with contamination with soil and kernel damage to as high as 22% (Paulsen et al., 2015), low output depending on the worker's health and motivation (Kołodziej and Ligarski, 2017), and are inefficient with high drudgery and time-consuming (Oluwole et al., 2007).

Meanwhile, commercial shellers are beyond the reach of small and medium-scale processors due to their exorbitant prices and higher output capacity of up to 23 MT·h$^{-1}$ (Butts et al., 2016). Therefore, the need for lower capacity shellers for medium scale processing enterprises that can handle the processing of 100 kg to 1 ton of groundnuts per hour are needed to minimize the losses. Because of these challenges, local fabricators took up the opportunity of fabricating local shellers to address the problems mentioned above. This could not solve the problem completely. Research institutes and universities were tasked with the responsibility to identify the locally fabricated shellers that fall short of processing requirements in terms of output capacity, shelling and cleaning efficiency, and kernel damage. These shellers were modified, and new ones were also developed to meet the requirements and demands of the processing industry. A Bambara groundnut sheller of 96% shelling efficiency, 97.3% cleaning efficiency, 3.4% breakage, and 0.6% unshelled pods at a feed rate of 215.8 kg·h$^{-1}$ was reported by Oluwole et al. (2007). Gitau et al. (2013) also reported shelling efficiency of 88.73% and kernel damage of 4% achieved with a sieve size of 11 mm and clearance of 16 mm. These shellers have their limitations ranging from crop suitability to weaknesses in the shelling mechanism design, which hinder the attainment of intended performances. Therefore, the Agricultural and Environmental Engineering Department of Bayero University Kano, Nigeria, modified a locally developed groundnut sheller that needed a comprehensive performance evaluation to establish its performance indices.

The objective of this study is to carry out a performance evaluation of the groundnut sheller and optimize its performance indices (output capacity, shelling and cleaning efficiencies, and kernel damage) based on the Box-Behnken design of response surface methodology (RSM).

**Contact address:** Aliyu Idris Muhammad, Bayero University Kano, Department of Agricultural and Environmental Engineering, Nigeria, e-mail: aimuhammad.age@buk.edu.ng

## Material and methods

### Sample preparation

Ex-Dakar groundnut pods were purchased from Dawanau international grain market, Nigeria, and soaked in clean water for 24 h. The pods were then spread out under shed in a thin layer to dry naturally with ambient air until desired moisture levels were achieved by measuring with a digital seed moisture meter (Scientech SE-233, India). The groundnut pods with desired moisture levels were sealed in marked polythene bags to maintain stable and uniform moisture content. A similar procedure was reported elsewhere (Gitau et al., 2013).

### Groundnut sheller description

The groundnut sheller comprises shelling and cleaning units attached to a blower, seeds, and chaffs outlets, as shown in Fig. 1. The detailed sheller design has been reported by Muhammad and Isiaka (2019).

### Sheller performance and evaluation parameters

The prototype groundnut sheller was started and allowed to stabilize. The speed was adjusted by setting the throttle at the desired drum speed level. A known quantity of groundnut pods was placed into the hopper and controlled via a feed gate device attached to the hopper. The groundnut kernels shelled were collected at the seed outlet, and the time between the feeding and shelling was measured and recorded with a stopwatch. Similarly, the unshelled groundnut pods and the chaffs were collected and weighed separately. The prototype groundnut sheller performance was evaluated based on output capacity, shelling and cleaning efficiencies, and kernel damage.

**Table 1** Experimental design variables for the study

| S/N | Factors | Units | Levels | | |
|---|---|---|---|---|---|
| | | | -1 | 0 | +1 |
| 1 | Shelling drum speed (A) | rpm | 180 | 220 | 260 |
| 2 | Moisture content (B) | % | 8 | 10 | 12 |
| 3 | Feed rate (C) | kg·h$^{-1}$ | 150 | 250 | 350 |

### Experimental design and statistical analysis

A three-factor and three-level design was employed. The factors were shelling drum speed denoted (A), moisture content (B), and feed rate (C), as presented in Table 1. For each factor, the experimental ranges were selected based on the preliminary trial results. These factors were used to design and optimize the performance parameters of the groundnut sheller using response surface methodology (RSM) of Design-Expert software (Design-Expert v11.0.5, Stat-Ease Inc., Minneapolis, USA). The RSM has the advantage of reducing the number of experimental runs needed to evaluate multiple parameters and their interactions. A Box-Behnken design was utilized, because it is a unique three-level design that generates a higher-order response with few required runs to maintain the higher-order surface response. A total of 17 experimental runs and 5 replicates at centre points were performed (Table 2). A second-order polynomial model was used to optimize these responses, as demonstrated in Eq. (1) (Jafari et al., 2020; Khayer et al., 2019).

$$Y = \beta_o + \sum_{i=1}^{n} \beta_i X_i + \sum_{i=1}^{n} \beta_{ii} X_i^2 + \sum_{i=1}^{n-1} \sum_{j=i+1}^{n} \beta_{ij} X_i X_j \quad (1)$$

where:

$Y$ – predicted response
$\beta_o$ – constant
$\beta_i$, $\beta_{ii}$, $\beta_{ij}$ – linear, quadratic and interaction coefficients, respectively
$X_i$, $X_j$ – levels of the independent variables

Using the analysis of variance (ANOVA), the goodness of fit of the developed non-linear models were assessed by lack of fit, *R*-squared values ($R^2$, adjusted $R^2$, and predicted $R^2$), adequate precision, and coefficient of variation (*CV*).

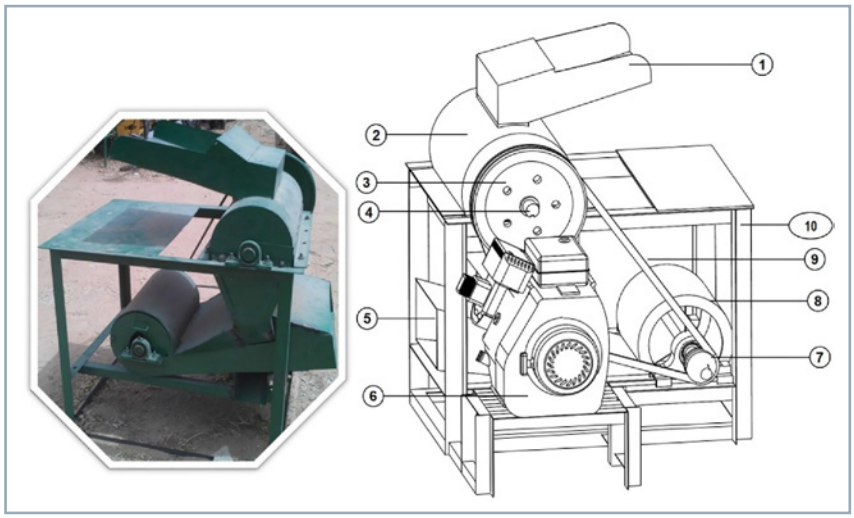


**Fig. 1** Developed groundnut sheller and components
1 – hopper, 2 – shelling chamber, 3 –driven pulley, 4 – driven shaft, 5 – chaff outlet, 6 – prime mover, 7 – driving pulley, 8 – blower, 9 – belt, 10 – frame

## Results and discussion

### Model fitting and statistical analysis

A total of 17 runs of Box-Behnken design and observed response data for the performance evaluation of groundnut sheller are presented in Table 2. These observed response data were statistically analysed (Table 3) to generate the best-predicted quadratic models that define the correlation between the experimental variables and the responses. The developed models in terms of coded

**Table 2** Box-Behnken design showing the experimental results responses and variables

| Run | Input variables | | | Responses | | | |
|---|---|---|---|---|---|---|---|
| | A: drum speed (rpm) | B: moisture content (%) | C: feed rate (kg·h$^{-1}$) | output capacity (kg·h$^{-1}$) | shelling efficiency (%) | cleaning efficiency (%) | kernel damage (%) |
| **1** | 260 | 10 | 350 | 342.3 | 95.2 | 50.0 | 5.4 |
| **2** | 220 | 12 | 150 | 121.4 | 90.5 | 42.4 | 2.9 |
| **3** | 220 | 10 | 250 | 225.6 | 96.7 | 51.3 | 3.5 |
| **4** | 220 | 8 | 350 | 310.3 | 98.2 | 55.6 | 4.3 |
| **5** | 220 | 10 | 250 | 243.1 | 97.9 | 51.6 | 4.0 |
| **6** | 220 | 10 | 250 | 242.8 | 98.1 | 51.2 | 3.6 |
| **7** | 220 | 8 | 150 | 147.0 | 97.1 | 53.1 | 3.7 |
| **8** | 260 | 8 | 250 | 245.9 | 97.9 | 56.1 | 5.6 |
| **9** | 180 | 12 | 250 | 138.7 | 84.0 | 32.3 | 3.4 |
| **10** | 220 | 12 | 350 | 281.8 | 85.4 | 39.2 | 5.6 |
| **11** | 220 | 10 | 250 | 243.1 | 97.6 | 52.3 | 3.9 |
| **12** | 180 | 10 | 150 | 120.4 | 95.4 | 40.3 | 1.1 |
| **13** | 260 | 12 | 250 | 218.6 | 90.5 | 44.8 | 6.0 |
| **14** | 180 | 10 | 350 | 234.6 | 91.7 | 39.1 | 3.6 |
| **15** | 220 | 10 | 250 | 243.8 | 98.0 | 51.4 | 3.8 |
| **16** | 180 | 8 | 250 | 205.9 | 96.0 | 49.9 | 3.3 |
| **17** | 260 | 10 | 150 | 141.2 | 97.7 | 50.2 | 4.1 |

**Table 3** ANOVA for response surface quadratic model of the performance evaluation of the groundnut sheller

| Source | df | Output capacity (kg·h$^{-1}$) | | Shelling efficiency (%) | | Cleaning efficiency (%) | | Kernel damage (%) | |
|---|---|---|---|---|---|---|---|---|---|
| | | sum of squares | *p*-value | sum of squares | *p*-value | sum of squares | *p*-value | sum of squares | *p*-value |
| **Model** | 9 | 67626.24 | <0.0001 | 326.58 | <0.0001 | 728.10 | <0.0001 | 22.22 | <0.0001 |
| **A: drum speed** | 1 | 7708.47 | <0.0001 | 25.10 | <0.0001 | 193.95 | <0.0001 | 12.01 | <0.0001 |
| **B: moisture content** | 1 | 2796.40 | 0.0003 | 188.28 | <0.0001 | 393.82 | <0.0001 | 0.1058 | 0.1108 |
| **C: feed rate** | 1 | 51171.20 | <0.0001 | 12.95 | 0.0007 | 0.5725 | 0.1755 | 6.23 | <0.0001 |
| **AB** | 1 | 398.60 | 0.0437 | 5.22 | 0.0083 | 9.86 | 0.0004 | 0.0324 | 0.3462 |
| **AC** | 1 | 1888.77 | 0.0011 | 0.3969 | 0.3490 | 0.2756 | 0.3304 | 0.3600 | 0.0120 |
| **BC** | 1 | 1.0000 | 0.9056 | 9.55 | 0.0017 | 8.27 | 0.0007 | 1.04 | 0.0007 |
| **$A^2$** | 1 | 1916.15 | 0.0010 | 11.84 | 0.0009 | 75.95 | <0.0001 | 0.0469 | 0.2639 |
| **$B^2$** | 1 | 1089.07 | 0.0048 | 63.44 | <0.0001 | 10.08 | 0.0004 | 2.07 | <0.0001 |
| **$C^2$** | 1 | 321.65 | 0.0632 | 3.79 | 0.0172 | 24.95 | <0.0001 | 0.4033 | 0.0092 |
| **Residual** | 7 | 462.73 | | 2.76 | | 1.76 | | 0.2224 | |
| **Lack of fit** | 3 | 214.07 | 0.4317 | 1.48 | 0.3344 | 1.02 | 0.2801 | 0.0285 | 0.8944 |
| **Pure error** | 4 | 248.66 | | 1.28 | | 0.7409 | | 0.1939 | |
| **$R^2$** | | 0.9932 | | 0.9933 | | 0.9976 | | 0.9901 | |
| **Adjusted $R^2$** | | 0.9845 | | 0.9847 | | 0.9945 | | 0.9774 | |
| **Predicted $R^2$** | | 0.9440 | | 0.9557 | | 0.9760 | | 0.9662 | |
| **C.V. %** | | 3.73 | | 0.56 | | 1.05 | | 4.47 | |
| **Adequate precision** | | 36.19 | | 33.13 | | 62.03 | | 35.46 | |

factors obtained after screening out the insignificant terms are presented in Eq. (2) to Eq. (5). The influence of input variables on the response variables were plotted using the three-dimensional (3D) and contour plots.

$$\text{Output capacity (kg·h}^{-1}) = 239.69 + \\ + 31.04A - 18.7B + 79.98C + 9.98AB + \\ + 21.73AC - 49.88A^2 - 16.08B^2 \quad (2)$$

$$\text{Shelling efficiency (\%)} = 97.65 + \\ + 1.62A - 4.37B - 1.69C + \\ + 0.8475AB - 2.38BC - 1.86A^2 - \\ - 3.4B^2 - 0.7642C^2 \quad (3)$$

$$\text{Cleaning efficiency (\%)} = 51.57 + \\ + 4.92A - 7.02B + 1.57AB - 1.44BC - \\ - 4.25A^2 - 1.55B^2 - 2.43C^2 \quad (4)$$

$$\text{Kernel damage (\%)} = 3.75 + 1.23A + \\ 0.8825C - 0.3AC + \\ + 0.51BC + 0.7005B^2 - 0.3095C^2 \quad (5)$$

The analysis of variance (ANOVA) used to fit the developed model showed that all the quadratic models were significant ($p$ <0.0001), as evident from the p values for all the responses in Table 3. This showed that the developed models could explain the variations between the input variables and responses. The coefficient of determination ($R^2$) explains the precision with which the developed models fitted the experimental data. A high $R^2$ value closer to 1 indicates a good correlation of the input variables and response variable (Kamal et al., 2019). In this study, the $R^2$ value for output capacity, shelling and cleaning efficiencies, and kernel damage were 0.9932, 0.9933, 0.9976, and 0.9901, respectively. Similarly, the adjusted $R^2$ values for all the response variables were greater than 0.9 (Table 3). The predicted $R^2$ values for output capacity (0.9440), shelling efficiency (0.9557), cleaning efficiency (0.9760), and kernel damage (0.9662) were in reasonable agreement with the adjusted $R^2$ values. A difference of less than 0.2 demonstrates a high degree of correlation between the experimental and predicted values. Therefore, the insignificant ($p$ >0.05) lack of fit observed in all the responses indicates the goodness of fit of the models relative to pure error. Thus, all the models are acceptable. Figs. 2 a–d illustrate the graphical representation of the correlation analysis for the performance parameters.

The coefficient of variance (*CV*) highlighted the extent of deviation of the experimental data from the predicted values. A *CV* of less than 10% exhibited better reliability (Islam Shishir et al., 2016). As shown in Table 3, the *CV* values for the output capacity, shelling efficiency, cleaning efficiency, and kernel damage were below 10%. Thus, it demonstrated that the developed models for all the responses were of high reliability and precision. For adequate precision, a value greater than 4 is desirable and showed the consistency of the predicted models to describe the experimental process (Islam Shishir et al., 2016; Manivannan and Rajasimman, 2011)processing time (30–150 min. As pointed out in Table 3, all the responses of performance parameters had adequate precision greater than 4, which suggested that the predicted models were consistent with the performance parameters.

## Influence of input variables on the sheller performance responses

### Output capacity

Output capacity is a performance parameter that measures the quantity of groundnut the sheller can handle for specific input variables. From Table 3, the ANOVA indicated that the input variables A, B, C, the linear-quadratic terms, AB and AC, and square terms $A^2$ and $B^2$ are significant ($p$ <0.05). The 3D and contour plots of output capacity versus moisture content and drum speed are shown in Fig. 3a. The response surface plots are used to acquire the optimum set of input variables that give a maximum or minimum value of the response (Ramakrishnan and Arumugam, 2012). The output capacity ranged from 120.4 to 250.3 kg·h$^{-1}$ (Fig. 3). The effect of input variables reveals that the output capacity increased with increases in drum speed and feed rate, and a reduction in moisture content. However, under extreme processing conditions of 260 rpm drum speed and 12% moisture content, the output capacity of the groundnut sheller declined (Fig. 3). This could be due to the high moisture level of the groundnut pods, which increased the pods' resistance to be processed by the sheller. Previous studies have reported

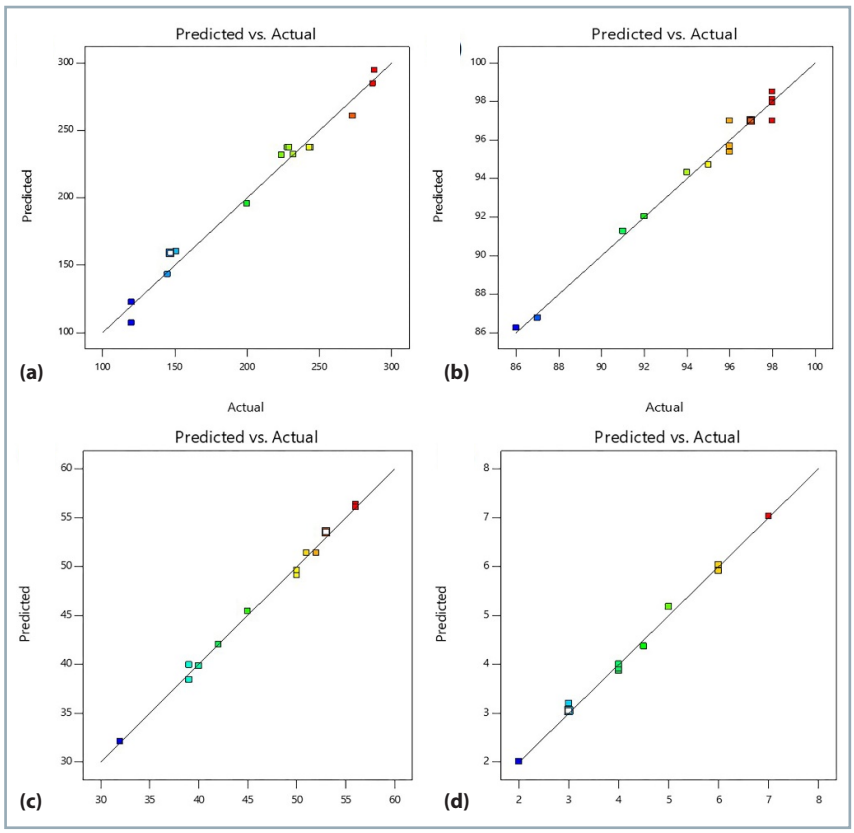


**Fig. 2** Correlation between the predicted and actual values of (a) output capacity, (b) shelling efficiency, (c) cleaning efficiency and (d) kernel damage

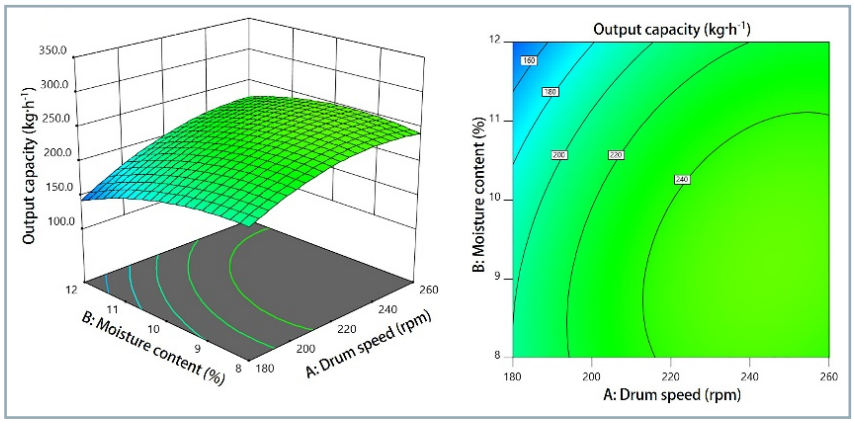


**Fig. 3** Response surface and contour plots showing the effects of variables on output capacity

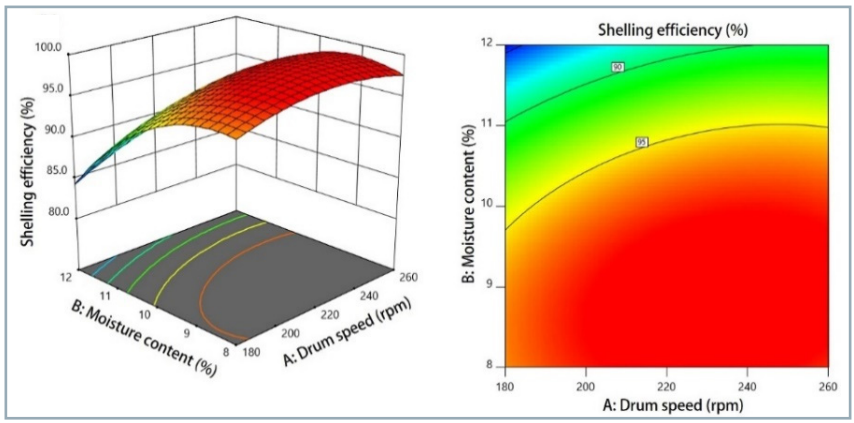


**Fig. 4** Effects of the input variables on shelling efficiency

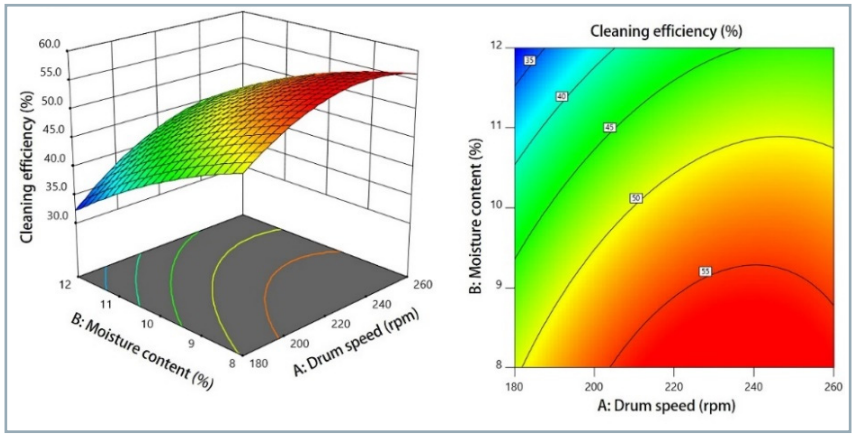


**Fig. 5** Influence of the input variables on the cleaning efficiency

that moisture content significantly affects the quantity of shelled Bambara groundnut (Atiku et al., 2004). Singh et al. (2008) reported a threshing capacity of 64.6 kg·h$^{-1}$ during the performance evaluation of paddy thresher.

### Shelling efficiency

Shelling efficiency is an important performance parameter that estimates the volume of groundnut kernels separated from the groundnut pods. The input variables A, B, and C, the linear-quadratic terms (AB and BC), and square terms $A^2$, $B^2$, and $C^2$ have significant effects on shelling efficiency (Table 3). The 3D and contour plots generated for the fitted model to visualize the effect of input variables on shelling efficiency were showcased in Fig. 4. The shelling efficiency ranged from 84.0 to 98.2%. The minimum shelling efficiency was observed with the lowest drum speed of 180 rpm, highest moisture content of 12%, and 250 kg·h$^{-1}$ feed rate, whereas the maximum shelling efficiency was recorded with the lower moisture level of 8%, drum speed of 220 rpm, and feed rate of 350 kg·h$^{-1}$, as established in Fig. 4. The shelling efficiency rises with increased drum speed and a decrease in the moisture content of the groundnut pods. At low moisture level, groundnut pods are brittle what makes the shelling easier. A shelling efficiency of 98% was reported elsewhere (Chilur and Kumar, 2018). Certain researchers have reported that parameters such as concave size, shelling drum clearance, cylinder speed, the width of the feed gate, and moisture content of groundnuts influence the shelling efficiency of groundnut shellers (Butts et al., 2009; Muhammad and Isiaka, 2019).

### Cleaning efficiency

Cleaning efficiency is a performance parameter that determines the cleanliness of the processed groundnut kernels. Higher cleaning efficiency is desirable for groundnut processing because it increases its market value. The cleaning efficiency is significantly affected by the input variables, including A, B, and the linear-quadratic terms, AB and BC, as well as the square terms $A^2$, $B^2$, and $C^2$ (Table 3). The cleaning efficiency recorded in this study ranged from 32.3 to 56.1% (Fig. 5). A maximum cleaning efficiency of 56.1% was achieved at the lowest moisture level of 8% and drum speed of 260 rpm, as shown in 3D and contour plots (Fig. 5). The cleaning efficiency increased with a drop in the moisture content of the groundnut pods and an increase in drum speed. At lower moisture content, the groundnut chaffs become lighter in weight and thereby easily blown out of the chaff outlet by the air stream from the blower. A previous study reported a maximum cleaning efficiency of 87.3% at a moisture content of 5.3% (Oluwole et al., 2007). Atiku et al. (2004) reported the winnowing efficiency of the Bambara groundnut decrease with increased moisture content. The accumulation of moisture in the

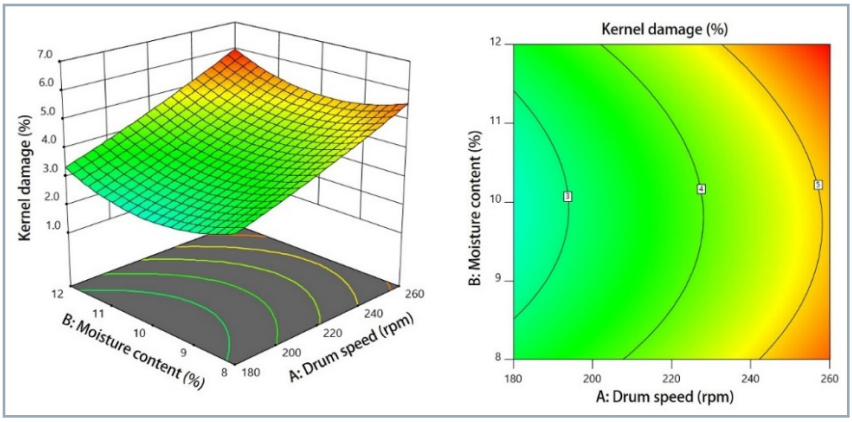


**Fig. 6** Influence of input variables on the kernel damage

groundnut pods could have increased the shell bulk density, which might increase pods' resistance to pneumatic separation.

### Kernel damage

The input variables A, B, C, linear quadratic terms AC and BC, and the square terms $B^2$ and $C^2$ significantly influenced the kernel damage of groundnut sheller (Table 3). Kernel damage in agricultural product processing must be kept to the minimum to avoid quality deterioration during storage. This performance response determines the quality (intact seed and seed viability) and the market value of groundnut commodity. Groundnut kernels with minimum damage can be kept for an extended period without pest and insect attack. As shown in the 3D and contour plots in Fig. 6, the kernel damage declined with decreased moisture content for the groundnut pods and drum speed. The highest kernel damage (6%) was obtained at moisture level and drum speed of 12% and 260 rpm, respectively (Fig. 6). However, the lowest kernel damage of 1.1% was obtained with input parameters of 180 rpm drum speed, 10% moisture level, and a feed rate of 150 kg·h$^{-1}$. According to Oluwole et al. (2004), moisture content significantly influenced the kernel damage of shea nuts. Sudajan et al. (2002) reported an increase in grain damage following an increase in drum speed and feed rate of sunflower during threshing. A kernel breakage of 3.4% for the Bambara groundnut was recorded at a feed rate of 215.8 kg·h$^{-1}$ after shelling (Oluwole et al., 2007).

### Optimization of the groundnut sheller performance

The quadratic models obtained in this study were employed to optimize process conditions for the performance evaluation of the groundnut sheller. The input variables, including drum speed, moisture content, and feed rate used, were in the range of 180–260 rpm, 8–12%, and 150–350 kg·h$^{-1}$, respectively. In this study, the aim is to obtain the maximum output capacity, shelling, and cleaning efficiencies, whereas the kernel damage is kept to the minimum. Numerical optimization of the process conditions using Stat-Ease Design-Expert software was conducted to get the optimum solutions. The software desirability function was used in achieving the optimum process conditions. These predicted optimum input variables were drum speed of 209.28 rpm, moisture content of 8.44%, and feed rate of 350 kg·h$^{-1}$. The optimum performance responses for the predicted input variables are shown in Table 4.

**Table 4** Predicted and experimental values of the performance responses at optimum conditions of the groundnut sheller

| Performance responses | Comparison | |
|---|---|---|
| | predicted values | experimental test values |
| **Output capacity (kg·h$^{-1}$)** | 302. 52 | 297.82 0.13 |
| **Shelling efficiency (%)** | 97.61 | 98.21 0.17 |
| **Cleaning efficiency (%)** | 53.16 | 52.33 0.25 |

values are means ±SD of three replicates

### Models verification

Three independent performance tests were conducted for model verification. The recommended optimum input variables for drum speed, moisture content, and feed rate were adjusted to approx. values of 210 rpm, 8%, and 350 kg·h$^{-1}$, respectively, for the convenience of taking the measurement. The performance test results corresponded with the predicted optimum responses, as presented in Table 4. Goyal et al. (2008) reported similar conformity between predicted and experimental values after the performance evaluation of a dehulling machine. From our study, the optimum performance indices recorded were 302.52 kg·h$^{-1}$ for output capacity, 97.61% for shelling efficiency, 53.16% for cleaning efficiency, and 4.04% for kernel damage. The closeness of these values to the predicted values demonstrated the developed models' suitability.

### Conclusion

Response surface methodology was employed to optimize the input parameters (drum speed, moisture content, and feed rate) for optimum performance of a groundnut sheller in terms of output capacity, shelling efficiency, cleaning efficiency, and kernel damage. The optimum performance responses were achieved at drum speed of 210 rpm, moisture content of 8%, and feed rate of 350 kg·h$^{-1}$ and were similar to the predicted values from the RSM numerical optimization. This indicated that the RSM adequately described the developed models within the acceptable range of performance responses. Meanwhile, the performance of the sheller can be improved by redesigning the cleaning unit and increasing the clearance between the shelling drum and the concave to address the low cleaning efficiency and high kernel damage recorded, respectively.

**Acknowledgments**

The authors acknowledged financial support from Bayero University, Kano, Nigeria.

## References

ATIKU, A. A. – AVIARA, N. A. – HAQUE, M. A. 2004. Performance evaluation of a Bambara ground nut sheller. In Agricultural Engineering International: the CIGR, vol. VI, pp. 1–18.

BUTTS, C. L. – SORENSEN, R. B. – LAMB, M. C. 2016. Evaluation of a small-scale peanut sheller. In Peanut Science, vol. 43, no. 1, pp. 67–73.

BUTTS, C. L. – SORENSEN, R. B. – NUTTI, R. C. – LAMB, M. C. – FAIRCLOTH, W. H. 2009. Performance of equipment for in-field shelling of peanut for biodiesel production. In Transactions of the American Society of Agricultural and Biological Engineers, vol. 52, no. 5, pp. 1461–1469.

CHILUR, R. – KUMAR, S. 2018. Design and development of maize dehusker cum sheller: a technology for northern transition zone of Karnataka, India. In Journal of The Institution of Engineers (India): Series A, vol. 99, no. 2, pp. 231–243.

GITAU, A. N. – MBOYE, P. – NJOREOGE, B. N. K. – MBURU, M. 2013. Optimizing the performance of a manually operated groundnut (*Arachis hypogaea*) decorticator. In Open Journal of Optimization, vol. 02, pp. 26–32.

GOYAL, R. K. – VISHWAKARMA, R. K. – WANJARI, O. D. 2008. Optimisation of the pigeon pea dehulling process. In Biosystems Engineering, vol. 99, no. 1, pp. 56–61.

ISLAM SHISHIR, M. R. – TAIP, F. S. – AZIZ, N. A. – TALIB, R. A. – HOSSAIN SARKER, M. S. 2016. Optimization of spray drying parameters for pink guava powder using RSM. In Food Science and Biotechnology, vol. 25, no. 2, pp. 461–468.

JAFARI, F. – MOVAGHARNEJAD, K. – SADEGHI, E. 2020. Infrared drying effects on the quality of eggplant slices and process optimization using response surface methodology. In Food Chemistry, vol. 333, p. 127423.

KAMAL, M. M. – ALI, M. R. – SHISHIR, M. R. I. – SAIFULLAH, M. – HAQUE, M. R. – MONDAL, S. C. 2019. Optimization of process parameters for improved production of biomass protein from *Aspergillus niger* using banana peel as a substrate. In Food Science and Biotechnology, vol. 28, no. 6, pp. 1693–1702.

KHAYER, S. – PATEL, T. – DEWANGAN, K. N. 2019. Structural design optimization for pedal operated paddy thresher using response surface methodology. In Agricultural Engineering International: CIGR Journal, vol. 21, no. 1, pp. 67–73.

KOŁODZIEJ, S. – LIGARSKI, M. J. 2017. The influence of physical fatigue on work on a production line. In Acta Technologica Agriculturae, vol. 20, no. 3, pp. 63–68.

MANIVANNAN, P. – RAJASIMMAN, M. 2011. Optimization of process parameters for the osmotic dehydration of beetroot in sugar solution. In Journal of Food Process Engineering, vol. 34, no. 3, pp. 804–825.

MUHAMMAD, A. I. – ISIAKA, M. 2019. Modification of locally developed groundnut sheller. In Bayero Journal of Engineering and Technology, vol. 14, no. 2, pp. 169–182.

MUHAMMAD, A. I. – ISIAKA, M. – FAGGE, A. A. – ATTANDA, M. L. – LAWAN, I. – DANGORA, N. D. 2015. Some engineering properties of three varieties of groundnut pods and kernels. In Arid Zone Journal of Engineering, Technology and Environment, vol. 11, pp. 61–75.

OLUWOLE, F. A. – ABDULRAHIM, A. T. – OUMAROU, M. B. 2007. Development and performance evaluation of impact bambara groundnut sheller. In International Agrophysics, vol. 21, pp. 269–274.

OLUWOLE, F. A. – AVIARA, N. A. – HAQUE, M. A. 2004. Development and performance tests of a sheanut cracker. In Journal of Food Engineering, vol. 65, no.1, pp. 117–123.

PANDIT, P. – JOSE, S. – PANDEY, R. 2020. Groundnut testa: An industrial agro-processing residue for the coloring and protective finishing of cotton fabric. In Waste and Biomass Valorization. https://doi.org/10.1007/s12649-020-01214-y

PAULSEN, M. R. – KALITA, P. K. – RAUSCH, K. D. 2015. Postharvest losses due to harvesting operations in developing countries: a review. In American Society of Agricultural and Biological Engineers Annual International Meeting 2015. New Orleans, USA, pp. 562–596.

RAMAKRISHNAN, R. – ARUMUGAM, R. 2012. Optimization of operating parameters and performance evaluation of forced draft cooling tower using response surface methodology (RSM) and artificial neural network (ANN). In Journal of Mechanical Science and Technology, vol. 26, no. 5, pp. 1643–1650.

SINGH, K. P. – PARDESHI, I. L. – KUMAR, M. – SRINIVAS, K. – SRIVASTVA, A. K. 2008. Optimisation of machine parameters of a pedal-operated paddy thresher using RSM. In Biosystems Engineering, vol. 100, no. 4, pp. 591–600.

SUDAJAN, S. – SALOKHE, V. M. – TRIRATANASIRICHAI, K. 2002. Effect of type of drum, drum speed and feed rate on sunflower threshing. In Biosystems Engineering, vol. 83, no. 4, pp. 413–421.

DOI: 10.2478/ata-2021-0002



Acta Technologica Agriculturae 1
Nitra, Slovaca Universitas Agriculturae Nitriae, 2021, pp. 8–13

# ORGANIC WASTE CONVERSION VIA CONTINUOUS ANAEROBIC CO-DIGESTION OF OIL PALM EMPTY FRUIT BUNCHES AND COW MANURE: EVALUATION OF FEEDING REGIME ON METHANE PRODUCTION

DARWIN*, Atmadian PRATAMA, MARDHOTILLAH

Syiah Kuala University, Banda Aceh, Indonesia

Anaerobic co-digestion of oil palm empty fruit bunches with cow manure was studied. The research focus was on the evaluation of feeding different solid concentrations of the substrate in the on-going process of anaerobic digestion. The solid concentrations ranged from 0.5 to 12% TS. Results of the study showed that the maximum methane production could be reached with the reactor digesting substrates with 4 to 8% TS, in which the methane produced was from 1300 to 1400 mL per day. A significant drop of pH from 7.02 to 5.97 occurred when the reactor was digesting substrates with 10 and 12% TS. Acidic condition caused by organic matter overloads lowered the efficiency of organic conversion represented in the low removal of COD, which was only 22.4%. This finding is highly significant for the waste management industries in terms of dealing with the digester upset due to the digestion of large amount of organic wastes.

**Keywords:** solid concentration; methane inhibition; acid accumulation

The oil palm (*Elaeis guineensis*) is the main crop in Indonesia. As a vital industry for supporting the economy, the oil palm trees have been massively cultivated in many parts of Indonesia's islands, such as Sumatera, Kalimantan and Sulawesi. The extraction of oil palm fruits and kernel generates a valuable vegetable oil. Currently, the vegetable oil produced from the oil palm has dominated the world vegetable oil market (USDA, 2007; Nieves et al., 2011). A third of the world vegetable oil consumption has been derived from the palm oil and is expected to increase within the next 20 to 30 years (Corley, 2009; Walter et al., 2009).

During the oil manufacturing process, large amounts of lignocellulosic wastes, such as empty fruit bunches, mesocarp fibres and shells, are generated. The wastes are periodically produced when palm oil and kernel oil are extracted from the pulp (endocarp) of oil palm fruits (Walter et al., 2009). Oil palm empty fruit bunch is the major lignocellulosic waste in the oil palm industry, which is commonly burned and/or incinerated, what can pollute the environment around the palm oil industry areas. As a non-wood lignocellulosic biomass, oil palm empty fruit bunch can potentially be used as a feedstock for bio-energy production (i.e. biogas). Biogas is a renewable energy produced biologically via anaerobic digestion process. Typical feedstock that can be used for biogas production includes energy crops and waste materials, such as wastewater, animal manure and agricultural wastes (Rahimi-Ajdadi and Esmaili, 2020). The major component of biogas is methane, which is clean and flammable gas containing high calorific value (55 $MJ \cdot kg^{-1}$) (Dinçer and Zamfirescu, 2014), and thereby can potentially be used as a gaseous biofuel for power generation (Aguilar-Virgen et al., 2014; Uddin et al., 2016).

As the palm oil manufacturer would continuously generate large amounts of organic wastes, managing the wastes properly is crucial for protecting the environment from the pollution and sustaining the operation of palm oil industry as a vital industry. The application of anaerobic digestion (AD) technology for treating the organic wastes from the palm oil industry is feasible, because the AD can effectively decompose the organic wastes and generate valuable gas (i.e. methane) from the energy-rich by-products (Nasir et al., 2012). Several studies (Aslanzadeh et al., 2014; Darwin et al., 2019) dealing with the operational systems and reactor design for running the process of anaerobic digestion have been carried out. Selection of a system for operating the AD highly depends on the existing reactor infrastructures. The types of biodegradable feedstock and their availability in a sufficient amount are important factors to be considered prior to establishing the process of anaerobic digestion on a small and/or large scale (Bacenetti et al., 2013; Naik et al., 2014; Liu et al., 2015). The study presented aims to evaluate the methane production in anaerobic co-digestion of oil palm empty fruit bunches with cow manure, and to investigate the effects of solid content in the continuous process of AD towards the daily methane production. The effectiveness of AD process is also investigated through the assessment of methane yield, productivity and the organic removal.

**Contact address:** DARWIN, Syiah Kuala University, Department of Agricultural Engineering, Banda Aceh 23111, Indonesia, e-mail: darwin_ae@unsyiah.ac.id

## Material and methods

### Material preparation

Oil palm empty fruit bunches used for this research were obtained from a palm oil mill in PPKS Bukit Sentang, Babalan-District of Langkat, North Sumatera. The collected feedstock was ground using a laboratory grinder to an average particle size of 1 ±0.2 mm. Cow manure utilized for the experiment was taken from the farm at Limpok, Darussalam, Banda Aceh, Indonesia. The manure was screened to remove any contaminants (e.g. sands, gravels, woods, metals and plastics), and stored in the fridge at the temperature of 4–5 °C prior to using it.

### Experimental design and procedures

Experiments of AD process were conducted at the Laboratory of Post-Harvest Technology and Bioprocess, Department of Agricultural Engineering, Syiah Kuala University. Several sample analysis measurements were carried out at the Institute for Research and Standardization of Industry, Banda Aceh. Two identical bioreactors made of acrylic were used for operating the AD process. The two reactors were continuously stirred at 100 rpm. The first reactor operated the process of anaerobic co-digestion of oil palm empty fruit bunches with cow manure, while the second reactor performed as the control reactor operating the AD of cow manure only. Both reactors ran under the steady state condition, in which the operational temperature was maintained under the mesophilic condition of 35 ±1 °C by using thermostatic water bath.

The working volume of the reactor was 4000 ml. The hydraulic retention time (HRT) applied for this experiment was 25 days. The loading rate applied for this experiment was 160 mL/day. To accomplish continuous operation, each reactor was equipped with the influent and effluent sample ports on the top of the reactors. To evaluate the performance of digesters, samples of the effluent from each reactor were withdrawn daily for further analysis. In order to ensure the process of anaerobic digestion under the continuous operation working properly, pH of the samples including influent as well as effluent was monitored periodically during the feeding and decanting periods. As pH was not controlled during the process, no alkaline and acid was added to the digesters. Methane production was measured daily using a gas meter based on the water displacement method.

Five hundred ml of 4 Molar NaOH was filled in a filter flask, which was then connected to the gas meters and reactors to purify the gas produced from the digester, and to entrap the contaminant gases (i.e. $CO_2$, $H_2S$). Prior to the experiment start, the culture was acclimated under the anoxic and mesophilic conditions until reaching the steady state condition with pH ranging between 6.8 and 7.2 (Darwin et al., 2018a). During the acclimation process, there were no substrates, alkaline and/or acid solutions added, and no effluent discarded.

### Investigation of feeding characters in anaerobic co-digestion

Effects of changing the substrate solid concentration fed into the on-going anaerobic co-digestion of oil palm empty fruit bunches (OPEFB) and cow manure were investigated via chemostat tests or continuous operating digesters. The reactors were operated within two cycles of HRT, i.e. 50 days. Firstly, 0.5% TS of the ground oil palm empty fruit bunch was added to the anaerobic co-digestion reactor, and the culture was acclimatized under the anaerobic condition for 10 days. During the acclimatization process, the culture in reactor was neither fed nor discharged.

Tests of the effects of different solid concentrations on the on-going process of anaerobic co-digestion of the OPEFB and cow manure were carried out after 10-day digestion, in which the reactor was fed with 0.5% TS of the ground OPEFB for 5 days since day 11. Since day 15, the reactor was fed with 1% TS of the ground OPEFB for 5 days. From day 20 to day 25, the reactor was fed with 2% TS of the ground OPEFB. From day 25 to day 30, the reactor was fed with 4% TS of the ground OPEFB. From day 30 to day 35, the reactor was fed with 8% TS of the ground OPEFB. From day 35 to day 40, the reactor was fed with 10% TS of the ground OPEFB. From day 40 to day 50 and/or the rest of experimental time, the reactor was fed with 12% TS of the ground OPEFB. During the process, pH was not adjusted and/or controlled.

### Analytical methods

The samples of influent and effluent were analysed for total solids (TS), volatile solids (VS), total dissolved solids (TDS), moisture content (MC), pH, chemical oxygen demand (COD), alkalinity, total Kjeldahl nitrogen (TKN). All analysed parameters were measured according to the Standard Method (Rice et al., 2017). In order to evaluate the presence of organic components in the culture and their utilization, the analysis of solid content and its removal was measured. To evaluate the efficiency of biodegradation during the process of anaerobic digestion, the percentage of volatile solid reduction and COD removal was assessed. The rates of methane production were measured as the volume of methane produced per day. To evaluate the effectiveness of substrate utilization with the production of methane as the end-product, methane yield was determined as the total methane produced per gram of volatile solids added (Gontupil et al., 2012; Darwin et al., 2016).

## Results and discussion

In order to evaluate the methane potential of OPEFB co-digested with cow manure, two identical anaerobic stirred reactors were utilized. The process of anaerobic digestion was operated in continuous mode to evaluate whether the addition of fresh substrates and effluent discharged could optimize the methane productivity and minimize the risk of digester failure. The physicochemical characteristics of the input materials used for anaerobic digestion were shown in Table 1.

Results show that the anaerobic culture of cow manure only possessed low pH of 6.02, which was too acidic for

AD. Hence, anaerobic co-digestion of OPEFB with cow manure could potentially stabilize the process of AD, as its alkalinity is higher (3941 mg·l$^{-1}$) than it would be in the AD of only cow manure as a single substrate (2605 mg·l$^{-1}$). The experiment results showed that the digestion of solely cow manure would have approx. four times lower organic loading rates (0.31 g·VS·l$^{-1}$·day$^{-1}$) compared to the reactor processing the OPEFB co-digested with cow manure, which had a significant amount of organic matters loaded into the reactor (1.4 g·VS·l$^{-1}$·day$^{-1}$).

Results show that, within initial 10 days of incubation, anaerobic co-digestion of the OPEFB and cow manure did not produce any significant amount of methane. In this period, the culture was in the lag phase, in which the microbial culture acclimatized to the anaerobic condition. During the acclimatization process, the anaerobic co-digestion reactor produced small amount of methane that was between 50 and 90 ml per day, while no methane was produced in the control reactor (Fig. 1). Started at day 11 of incubation, chemostat test had been applied, in which 0.5% TS of the substrate was loaded into the anaerobic co-digestion reactor. From day 11 to day 15, methane production increased from 50 to 630 ml in the anaerobic co-digestion reactor. A dramatical increase of methane production occurred from day 15 (630 ml) to day 20 (1320 ml). This suggests that the sufficient amount of organic matters loaded into the digestion system can significantly enhance the methane production.

The result is quite different from the previous study revealing that 2% TS of the substrate fed to the digester could generate more methane yield compared to the digester fed with 3 and 4% TS (Darwin et al., 2016). The differences found

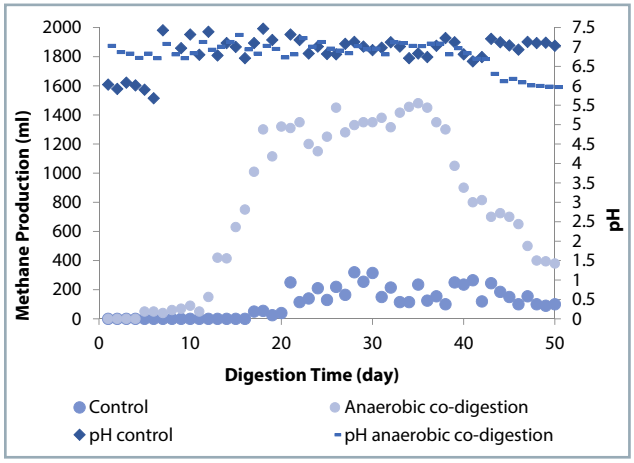


**Fig. 1** Daily methane production of anaerobic co-digestion of oil palm empty fruit bunches and cow manure under the continuous operation

can be attributed to the different operational system and different types of substrate used for the experiments. The current study was operated in the continuous system and 1% TS was applied from day 15 to day 20 of the incubation period and, within that period, the methane yield obtained was approx. 176.33 ml $CH_4$·g$^{-1}$·VS$^{-1}$, while the previous study was performed in the batch mode and generated the methane yield of 60.25 ml $CH_4$·g$^{-1}$·VS$^{-1}$ added after 35 days of fermentation. Furthermore, the substrates used in the previous study were swine manure co-digested with cocoa husk, while the present study deals with cow manure co-digested with the OPEFB.

**Table 1** Characteristics of the substrates

| Parameters | Unit | Cow manure | Oil palm empty fruit bunches |
|---|---|---|---|
| **Total solids** | % | 0.988 | 18.764 |
| **Volatile solids** | % | 47 | 70 |
| **Moisture content** | % | 99.01 | 81.24 |
| **Total Kjeldahl nitrogen** | mg·l$^{-1}$ | 410 | - |
| **Chemical oxygen demand** | mg·l$^{-1}$ | 9120 | - |
| **Alkalinity** | mg·l$^{-1}$ | 2600 | - |
| **Total dissolved solids** | mg·l$^{-1}$ | 2710 | - |
| **pH** | - | 6.02 | - |

**Table 2** Influent data of anaerobic digestion process

| Parameters | Unit | Control (cow manure) | Oil palm empty fruit bunches co-digested with cow manure |
|---|---|---|---|
| **Total solids** | % | 2.253 | 5.96 |
| **Volatile solids** | % | 46.92 | 78.5 |
| **Moisture content** | % | 97.75 | 94.04 |
| **Total Kjeldahl nitrogen** | mg·l$^{-1}$ | 414 | 435 |
| **Chemical oxygen demand** | mg·l$^{-1}$ | 9130 | 9874 |
| **Alkalinity** | mg·l$^{-1}$ | 2605 | 3941 |
| **Total dissolved solids** | mg·l$^{-1}$ | 2730 | 4.25 |
| **Organic loading rate** | g·VS·l$^{-1}$·day$^{-1}$ | 0.317 | 1.402 |
| **pH** | – | 6.08 | 7.03 |

Results show that the methane production tended to decrease when the substrate concentration was increased from 8 to 10% TS. From day 36 of the incubation when the reactor was loaded with the substrate 10% TS, the daily methane production tended to decline. As depicted in Fig. 1, from day 37 to 38 when the reactor was fed with 10% TS of the substrate, the pH culture dropped from 7.09 to 6.81. This condition continuously occurred until the rest of the experiment, in which the organic acids accumulated in the digester, and sharply dropped the pH to 5.9 on day 50. This suggests that 10% TS of the substrate loaded to the reactor disturbed the AD process due to organic acid build-up, and thereby led to the digester upset, which totally prevented the methane production.

As presented in Table 3, the results show that effluent pH of the anaerobic co-digestion reactor (pH 5.97) was lower than effluent pH of the control reactor (7.02). This occurred as an excessive amount of organic materials was loaded to the reactor (Fig. 1). The study also reveals that, at the early stage of the experiment, the organic loading rate introduced to the reactor was 1.402 g·VS·$l^{-1}$·$day^{-1}$, which was approx. four times higher than the organic loading rate applied to the control reactor (0.3 g·VS·$l^{-1}$·$day^{-1}$).

The assessment of biodegradation efficiency indicates that anaerobic co-digestion of the OPEFB with cow manure could significantly enhance the methane production in comparison to AD of cow manure only. The results suggest that the methane productivity obtained from the anaerobic co-digestion reactor was approx. seven times higher (795 ml $CH_4$·$day^{-1}$) than from the control reactor (109.9 ml $CH_4$·$day^{-1}$). Even if the gradual increase of the organic loads had been applied, the conversion of organic solid materials was still somewhat high, in which the volatile solids (VS) reduction obtained was at approx. 80%. This is quite different from the study by Bujoczek et al. (2000), who reported that VS reduction would be low with an increase in organic acids and/or volatile fatty acids (VFA) in the digester. The difference occurred, as high percentage of VS reduction reported in Table 4 was obtained from the total organic solid reduction after 50 days of incubation.

The characteristics of substrates presented in Table 1 reveal that the OPEFB contained a lot of organic materials, representing 70% of volatile solids (VS). High percentage of VS indicates that the substrate contains a significant amount of organic matters (Darwin et al., 2016), which was required as a source of carbon and/or energy for the microbial growth and metabolism (Yu et al., 2015). This suggests that the OPEFB can be potential substrate used in AD to enhance the methane productivity.

The study shows that pH of cow manure was somewhat too acidic (pH 6.02). The low pH can be an inhibitory factor when the single substrate is used as the only substrate for AD. Ye et al. (2012) mentioned that low pH can hinder methane production through direct inhibition of methanogenesis pathways and indirect effects on fermentation. The study reported that increasing pH enhances the efficiency of methane production, as well as fermentative activity, and increase the availability of substrates (i.e. acetate and/or H2) for methanogens, resulting in significant increase in methane productivity (Ye et al., 2012).

Lana et al. (1998) revealed that a drop of pH from 6.5 to 5.7 would significantly decrease the methane production. Authors found that low pH would dramatically lower buffering capacity in the culture. Since buffering capacity is essential to stabilize the AD process, enhancing buffering capacity in the culture is vital for improving the digestion performance (Zhu et al., 2010; Wang et al., 2014). The current study reveals that the OPEFB used as a co-substrate in AD of

**Table 3** Effluent data of anaerobic digestion process

| Parameters | Unit | Control | Oil palm empty fruit bunches co-digested with cow manure |
|---|---|---|---|
| **Total solids** | % | 1.88 | 7.22 |
| **Volatile solids** | % | 23.73 | 41.7 |
| **Moisture content** | % | 98.12 | 92.8 |
| **Total Kjeldahl nitrogen** | mg·$l^{-1}$ | 390 | 417 |
| **Chemical oxygen demand** | mg·$l^{-1}$ | 7237 | 7661 |
| **Alkalinity** | mg·$l^{-1}$ | 2220 | 3210 |
| **Total dissolved solids** | mg·$l^{-1}$ | 2900 | 2.4 |
| **pH** | | 7.02 | 5.97 |

**Table 4** Biodegradation efficiency of anaerobic digestion process operated in continuously stirred reactors

| Parameters | Unit | Control | Oil palm empty fruit bunches co-digested with cow manure |
|---|---|---|---|
| **COD removal** | % | 20.73 | 22.41 |
| **Nitrogen removal** | % | 5.80 | 4.14 |
| **Volatile solids reduction** | % | 64.8 | 80.41 |
| **Total methane production** | ml | 5495 | 39750 |
| **Methane productivity** | ml $CH_4$·$day^{-1}$ | 109.9 | 795 |
| **Methane yield** | ml $CH_4$·$g^{-1}$·$VS^{-1}$ | 129.95 | 212.4 |

cow manure can potentially enhance the buffering capacity, and thereby can significantly improve methane productivity.

The influent data shown in Table 2 reveal that the characteristics of the OPEFB co-digested with cow manure culture can be used to optimize the methane production. This is due to the fact that the pH culture was of the neutral level (7.03). Liu et al. (2008) mentioned that the appropriate pH level for methane production is from 6.6 to 7.8 with an optimum of 6.8. The digester failure would occur once pH in the digester was lower than 6.1 and/or higher than 8.3 (Liu et al., 2008).

The OPEFB co-digested with cow manure had a significant amount of organic materials represented by 80% VS, while the control reactor digesting cow manure only had volatile solid content less than 50%. The organic content in substrates used for AD is significantly affected by the organic materials loaded into the reactor (Jiang et al., 2013; Darwin et al., 2017). This is significant, as the composition of the organic matters loaded to the digester would considerably affect the microbial growth rates, as well as the rates of methane production (Hallaji et al., 2019; Berberich et al., 2019).

The results suggest that, from day 11 to day 20, the anaerobic culture ran into an exponential or logarithmic phase, in which the production of methane increased significantly from 50 to 1350 ml. When the substrate concentration increased from 1% TS (day 20) to 8% TS (day 35), no significant increase in methane production was observed. The results indicate that, within the time of incubation from day 20 to day 35, the anaerobic culture was in the stationary phase despite the fact that the substrate concentration was increased, and methane production fluctuated between 1350 and 1450 ml (Fig. 1). This complies with findings of several authors (Kolter et al., 1992; Rallu et al., 1996; Heller, 2001), who revealed that microbes from the logarithmic phase would be much more susceptible to the environmental stresses in comparison to the microbes from the stationary phase.

The results also show that a lot of organic materials loaded into the anaerobic co-digestion reactor lowered the buffering capacity – the alkalinity dropped from 3941 to 3210 $mg \cdot l^{-1}$. This condition led to a dramatic drop of pH due to the increase of proton concentration as a result of organic acids build-up. This agrees with the study by Xu et al. (2014): the high organic loads cause the excessive accumulation of organic acids, especially volatile fatty acids (VFA), and thereby can intensively inhibit the AD. The study found that acetic acid was the primary inhibitor for methanogenesis. With an increase in organic loads, acetoclastic methanogenesis would be more sensitive to acetic acid in comparison to hydrogenotrophic methanogenesis (Xu et al., 2014).

The evidence obtained from the anaerobic co-digestion reactor was that the total solids of effluent were higher (7.22%) than total solids of influent (5.96%), suggesting that the low pH caused by organic acids build-up can inhibit the conversion of the substrate loaded (Table 1 and 2). This agrees with several studies (Veeken et al., 2000; Darwin et al., 2018b) revealing that high concentration of VFA accompanied by low pH can inhibit hydrolysis and can completely inhibit fermentation process to certain extent.

Since the anaerobic co-digestion reactor ran into substrate overloading that caused the organic acids accumulation, the decomposition process of organic materials to methane as the end-product was slowed down. The acidic condition had inhibited the growth of anaerobic microbes, as well as their activity, and thereby the conversion rates of all organic materials to methane gas were lowered. This phenomenon led to the low biodegradation efficiency, resulting in the COD removal from the anaerobic co-digestion reactor of approx. 22%. This agrees with the study by Bujoczek et al. (2000), who observed that the efficiency of organic matter conversion decreased with the decreased feeding of organic loads to the digesters.

The result of COD removal suggests that the conversion of organic matters to methane had been hindered by the low pH (pH <6.0). The study results also reveal that an overloading of substrate reduces the methane yield. This agrees with the study by Dai et al. (2013) showing that high organic loading rates applied to the anaerobic digester would potentially generate high risk of souring the culture, and thereby could inhibit the oxidation of organic materials to methane. As depicted in Table 4, the methane yield obtained from the anaerobic co-digestion reactor operated for 50 days of incubation was higher only by 39% than methane yield of the control reactor. This indicates that the anaerobic co-digestion of the OPEFB with cow manure should not be performed with solid concentrations lower than 8% TS in order to avoid organic acids accumulation in the digester that would suppress methanogens.

## Conclusion

The current study results show that the addition of OPEFB as co-substrate in AD of cow manure resulted in higher methane productivity (795 ml $CH_4 \cdot day^{-1}$) in comparison to the digestion of cow manure only (109.9 ml $CH_4 \cdot day^{-1}$). The increase of organic loads by feeding the substrate with 10% TS into the anaerobic co-digestion reactor could gradually generate acids in the culture. A dramatic drop of pH due to acid accumulation in the digester led to the low efficiency of the organic matter conversion, in which the COD removal was less than thirty percent, and thereby the methane production was severely hindered.

## Acknowledgements

We kindly thank Universitas Syiah Kuala, Banda Aceh, Indonesia for financial support through the H-index research program coordinated by LPPM, UNSYIAH.

## References

AGUILAR-VIRGEN, Q. – TABOADA-GONZÁLEZ, P. – OJEDA-BENÍTEZ, S. – CRUZ-SOTELO, S. 2014. Power generation with biogas from municipal solid waste: Prediction of gas generation with *in situ* parameters. In Renewable and Sustainable Energy Reviews, vol. 30, pp. 412–419.

ASLANZADEH, S. – RAJENDRAN, K. – TAHERZADEH, M. J. 2014. A comparative study between single-and two-stage anaerobic digestion processes: Effects of organic loading rate and hydraulic retention time. In International Biodeterioration and Biodegradation, vol. 95, pp. 181–188.

BACENETTI, J. – NEGRI, M. – FIALA, M. – GONZÁLEZ-GARCÍA, S. 2013. Anaerobic digestion of different feedstocks: impact on energetic

and environmental balances of biogas process. In Science of the Total Environment, vol. 463, pp. 541–551.

BERBERICH, M. E. – BEAULIEU, J. J. – HAMILTON, T. L. – WALDO, S. – BUFFAM, I. 2019. Spatial variability of sediment methane production and methanogen communities within an eutrophic reservoir: Importance of organic matter source and quantity. In Limnology and Oceanography, vol. 9999, pp. 1–23.

BUJOCZEK, G. – OLESZKIEWICZ, J. – SPARLING, R. – CENKOWSKI, S. 2000. High solid anaerobic digestion of chicken manure. In Journal of Agricultural Engineering Research, vol. 76, pp. 51–60.

CORLEY, R. H. V. 2009. How much palm oil do we need? In Environmental Science and Policy, vol. 12, pp. 134–139.

DAI, X. – DUAN, N. – DONG, B. – DAI, L. 2013. High-solids anaerobic co-digestion of sewage sludge and food waste in comparison with mono digestions: stability and performance. In Waste Management, vol. 33, pp. 308–316.

DARWIN – TRIOVANTA, U. – RINALDI, R. 2019. Two-stage anaerobic co-digestion of landfill leachate and starch wastes using anaerobic biofilm reactor for methane production. In Progress in Agricultural Engineering Sciences, vol. 15, pp. 53–70.

DARWIN – ILHAM, M. – FAZIL, A. 2018a. Performance and kinetic study of the anaerobic co-digestion of cocoa husk and digested cow manure with high organic loading rate. In INMATEH-Agricultural Engineering, vol. 55, pp. 131–140.

DARWIN – CHARLES, W. – CORD-RUWISCH, R. 2018b. Ethanol and lactic acid production from sugar and starch wastes by anaerobic acidification. In Engineering in Life Sciences, vol. 18, pp. 635–642.

DARWIN – CHENG, J. J. – LIU, Z. – GONTUPIL, J. 2016. Anaerobic co-digestion of cocoa husk with digested swine manure: evaluation of biodegradation efficiency in methane productivity. In Agricultural Engineering International: The CIGR Journal, vol. 18, pp. 147–156.

DARWIN – FAZIL, A. – ILHAM, M. – SARBAINI – PURWANTO, S. 2017. Kinetics on anaerobic co-digestion of bagasse and digested cow manure with short hydraulic retention time. In Research in Agricultural Engineering Journal, vol. 63, pp. 121–127.

DINÇER, I. – ZAMFIRESCU, C. 2014. Advanced power generation systems. In Academic Press, pp. 129–133.

GONTUPIL, J. – DARWIN – LIU, Z. – CHENG, J. J. – CHEN, H. 2012. Anaerobic co-digestion of swine manure and corn stover for biogas production. In Annual International Meeting Conference, American Society of Agricultural and Biological Engineers, July 29–August 1, 2012, Dallas, U.S.A.

HALLAJI, S. M. – KUROSHKARIM, M. – MOUSSAVI, S. P. 2019. Enhancing methane production using anaerobic co-digestion of waste activated sludge with combined fruit waste and cheese whey. In BMC biotechnology, vol. 19, pp. 19.

HELLER, K. J. 2001. Probiotic bacteria in fermented foods: product characteristics and starter organisms. In The American Journal of Clinical Nutrition, vol. 73, pp. 374–379.

JIANG, J. – ZHANG, Y. – LI, K. – WANG, Q. – GONG, C. – LI, M. 2013. Volatile fatty acids production from food waste: effects of pH, temperature, and organic loading rate. In Bioresource Technology, vol. 143, pp. 525–530.

KOLTER, R. – SIEGELE, D. A. – TORMO, A. 1992. The stationary phase of the bacterial life cycle. In Annual Review of Microbiology, vol. 47, pp. 855–874.

LANA, R. P. – RUSSELL, J. B. – VAN AMBURGH, M. E. 1998. The role of pH in regulating ruminal methane and ammonia production. In Journal of Animal Science, vol. 76, pp. 2190–2196.

LIU, X. – BAYARD, R. – BENBELKACEM, H. – BUFFIÈRE, P. – GOURDON, R. 2015. Evaluation of the correlations between biodegradability of lignocellulosic feedstocks in anaerobic digestion process and their biochemical characteristics. In Biomass and Bioenergy, vol. 81, pp. 534–543.

LIU, C. F. – YUAN, X. Z. – ZENG, G. M. – LI, W. W. – LI, J. 2008. Prediction of methane yield at optimum pH for anaerobic digestion of organic fraction of municipal solid waste. In Bioresource Technology, vol. 99, pp. 882–888.

NAIK, L. – GEBREEGZIABHER, Z. – TUMWESIGE, V. – BALANA, B. B. – MWIRIGI, J. – AUSTIN, G. 2014. Factors determining the stability and productivity of small scale anaerobic digesters. In Biomass and Bioenergy, vol. 70, pp. 51–57.

NASIR, I. M. – GHAZI, T. I. M. – OMAR, R. 2012. Production of biogas from solid organic wastes through anaerobic digestion: a review. In Applied Microbiology and Biotechnology, vol. 95, pp. 321–329.

NIEVES, D. C. – KARIMI, K. – HORVÁTH, I. S. 2011. Improvement of biogas production from oil palm empty fruit bunches (OPEFB). In Industrial Crops and Products, vol. 34, pp. 1097–1101.

RAHIMI-AJDADI, F. – ESMAILI, M. 2020. Effective pre-treatments for enhancement of biodegradation of agricultural lignocellulosic wastes in anaerobic digestion-a review. In Acta Technologica Agriculturae, vol. 23, no. 3, pp. 105–110.

RALLU, F. – GRUSS, A. – MAGUIN, E. 1996. Lactococcus lactis and stress. In Antonie van Leeuwenhoek, vol. 70, pp. 243–251.

RICE, E. W. – BAIRD, R. B. – EATON, A. D. 2017. Standard Methods for the Examination of Water and Wastewater. 23rd edition. In American Public Health Association, Washington, D.C., U.S.A. ISBN 9780875532875.

UDDIN, W. – KHAN, B. – SHAUKAT, N. – MAJID, M. – MUJTABA, G. – MEHMOOD A. – ALI, S. M. – YOUNAS, U. – ANWAR, M. – ALMESHAL, A. M. 2016. Biogas potential for electric power generation in Pakistan: A survey. In Renewable and Sustainable Energy Reviews, vol. 54, pp. 25–33.

USDA. 2007. Indonesia: Palm Oil Production Prospects Continue to Grow, Foreign Agricultural Service. Commodity Intelligence Report. In The United States Department of Agriculture.

VEEKEN, A. – KALYUZHNYI, S. – SCHARFF, H. – HAMELERS, B. 2000. Effect of pH and VFA on hydrolysis of organic solid waste. In Journal of Environmental Engineering, vol. 126, pp. 1076–1081.

WALTER, A. – FRANKE-WHITTLE, I. H. – WAGNER, A. O. – INSAM, H. 2009. Methane yields and methanogenic community changes during co-fermentation of cattle slurry with empty fruit bunches of oil palm. In Bioresource Technology, vol. 175, pp. 619–623.

WANG, D. – AI, J. – SHEN, F. – YANG, G. – ZHANG, Y. – DENG, S. – ZHANG, J. – ZENG, Z. – SONG, C. 2014. Improving anaerobic digestion of easy-acidification substrates by promoting buffering capacity using biochar derived from vermicompost. In Bioresource Technology, vol. 227, pp. 286–296.

XU, Z. – ZHAO, M. – MIAO, H. – HUANG, Z. – GAO, S. – RUAN, W. 2014. *In situ* volatile fatty acids influence biogas generation from kitchen wastes by anaerobic digestion. In Bioresource Technology, vol. 163, pp. 186–192.

YU, B. – LOU, Z. – ZHANG, D. – SHAN, A. – YUAN, H. – ZHU, N. – ZHANG, K. 2015. Variations of organic matters and microbial community in thermophilic anaerobic digestion of waste activated sludge with the addition of ferric salts. In Bioresource Technology, vol. 179, pp. 291–298.

YE, R. – JIN, Q. – BOHANNAN, B. – KELLER, J. K. – MCALLISTER, S. A. – BRIDGHAM, S. D. 2012. pH controls over anaerobic carbon mineralization, the efficiency of methane production, and methanogenic pathways in peatlands across an ombrotrophic–minerotrophic gradient. In Soil Biology and Biochemistry, vol. 54, pp. 36–47.

ZHU, J. – WAN, C. – LI, Y. 2010. Enhanced solid-state anaerobic digestion of corn stover by alkaline pretreatment. In Bioresource Technology, vol. 101, pp. 7523–7528.

DOI: 10.2478/ata-2021-0003



Acta Technologica Agriculturae 1
Nitra, Slovaca Universitas Agriculturae Nitriae, 2021, pp. 14–19

# STUDYING THE EFFECT OF BALANCER ON ENGINE VIBRATION OF MASSEY FERGUSON 285 TRACTOR

Niusha FARROKHI ZANGANEH, Gholamhossein SHAHGHOLI*, Soleiman AGH

University of Mohaghegh Ardabili, Ardabil, Iran

The mechanical vibration causes health issues to drivers, such as backache, spinal cord injury, etc. In this regard, a tractor engine plays important role. Tractors without chassis are equipped with a balancer unit reducing the secondary engine vibrating force and decreasing the engine and tractor vibration. The paper presented investigates the effects of balancer on secondary vibration. In this research, the root mean square (RMS) of vibration was computed for specific periods of engine work. Effects of rotational speed and engine load on engine vibration in two modes with and without balancer were investigated. The results showed that, at full engine load, increasing the engine speed resulted in increasing the vibration in both observed modes. Balancer utilization reduced the vibration by 22.3% on average. At fixed rotational speed, increasing load caused an increase in vibration in both observed modes. At 1400 rpm rotational speed and 125 Nm torque, balancer utilization managed to reduce the RMS of secondary vibration by 38.9%. Furthermore, at 250 Nm, RMS vibrations were reduced by 21.3% in comparison to no balancer mode. At full load, variable rotational speed, the balancer significantly reduced vibration by 29% on average. The balancer proved to be more efficient at lower torques.

**Keywords:** vibration; load; rotational speed; root mean square

As the most important agricultural machinery, tractor plays a main role in planting and harvesting operations and especially in mechanized agriculture. One of the most frequently used tractors in Iran is Massey Ferguson 285 (MF285) produced by Iranian Tractor Company, which is the biggest manufacturing factory in Iran and Middle East.

One of the factors reducing mental and physical health is vibration (Bellman, 2002). Vibration is investigated by a wide range of engineering sciences and studied in different aspects (Bulgakov et al., 2017). Tractors and agricultural implements are used for conducting field operations and the fatigue and discomfort are not the only results of physical work; moreover, these can be caused by exposure to vibration (Taghizadeh et al., 2007).

Apart from the side effects of vibration in terms of health risks to entire body, this phenomenon has also negative mental effects. The operators working under influence of vibration tend to retire earlier than expected and if they continue to work under such conditions, health risk probability increases during their work. A tired operator is less efficient and imposes higher costs to employer. On the other hand, for the employer, paying the disability insurance is one of the other side losses caused by vibration. Therefore, reducing the vibration resulting from operation of mechanical tools and its side effects on human body is necessary as one of the characteristics of evaluating devices. The vibration, however, does not show any destructive effects on human organs in short-term and only reduces the human efficiency (Babakhani et al., 2010). It causes numerous side complications in the long term to the operators who are daily exposed to vibration of high domain. The threshold of complications resulting from vibration varies for different people and depends on factors such as exposure time, vibration domain, frequency, etc. Therefore, it is impossible to define a specific threshold point for a specific person, however, the Society of Automobile Engineers (SAE), International Standard Organization (ISO) and British Standard (BS) defined a series of thresholds. It has been shown that the tractor vibration under different operation conditions usually exceeds the defined thresholds of ISO2631-1 (2018). Accordingly, exposure to tillage operation conditions should not exceed 2.5 hours. High domain and low frequency vibration are factors constituting physical health risks to operator in the long term (Babakhani et al., 2010). The vibration side effects to entire body occur when the working time exceeds the defined working times (ISO2631-1, 2018).

The main source of vibration in agricultural tractors is the engine. Engine vibration results from cylinder firing, impacts due to piston clearances (piston slaps), fuel injection pressure, high rise of gas pressure during combustion and the impacts of admission and exhaust valves (Carlucci et al., 2006). Moreover, considering the tractor vibration, there is a direct relation to its engine, which transfers the vibration to operator's seat. Therefore, the effects of each engine part on its overall function and vibration should be studied in detail. Therefore, recognition, studying and optimization of different parts related to establishing and propagation of vibration are very important. The engine is balanced if the forces on supports are constant under ordinary engine

**Contact address:** Gholamhossein Shahgholi, University of Mohaghegh Ardabili, Ardabil, Iran, e-mail: gshahgoli@yahoo.com

work conditions in terms of quantity and their direction. In unbalanced engine, the pressure at supports varies frequently, causing engine vibration, which ultimately leads to vibration of the entire vehicle (Juan et al., 2017).

Vibration occurs in engines due to three main reasons (manufacturers consider these in designing and balancing the engine in order to reduce the vibration):

- vibration due to unbalance of rotatory parts: there is centrifugal force in each rotating part such as crankshaft, flywheel and clutch;
- vibration due to piston impact during crankshaft rotation (the crankshaft does not rotate at uniform speed because of external impacts), which can cause rotating vibration;
- vibration due to inertia of reciprocating parts – it occurs mostly due to piston's inertia especially in lower and upper parts of cylinder, where piston tends to continue motion; when piston reaches the TDS (top dead centre) and BDC (bottom dead centre), an inertia force produced engine vibration. This depends on increasing the engine speed (Breeze, 2018).

Gas pressure of combustion creates two force components, which is the main reason for engine vibration. There are two important factors for vibration production in internal combustion engines. The first factor is related to unbalance of torque and forces due to circulating or reciprocal movement of crankshaft and its parts. These issues can be balanced in six-cylinder engines or higher. In engines with less than six cylinders, there is always resistance or coupling force, which cannot be removed via balancing. The primary vibration established by these imbalances occurs at frequency uniform with engine speed and it is called first rank vibration. Vibration harmonics (also called second rank/third rank vibration) occur two or three times per engine rotation frequency. Due to the number of cylinders and arrangement of cranks, the resistance forces are retrofitted or removed upon changing the angle and it has lesser vibration domain. The second source of engine vibration produced by torque pulses results from increasing the gas pressure in combustion (Taghizadeh, 2011).

The weights are used for neutralizing the rotational inertia force. Bush bearings of shafts are lubricated by pressure, and the roller bearings of pump actuator shaft and idle gear are lubricated by spraying. Oil pump, balancer and pressure breaker valve are integrated. Rotating force of crankshaft rotates the crankshaft gear connected to the idle gear of balancer. On the other hand, this gear is connected to gear of balancer shaft and rotates the balancer weight via connecting pin on the shaft. The weights are connected via gear to each other, and rotation of one leads to rotation of the other. These weights rotate opposite to each other to eliminate the vibration. At both ends of two shafts, there are two needle roller bearings. At the end of balancer shaft, there is an oil pump gear operating the oil pump. The rotational speed of balancer shaft is twice the engine rotational speed to remove the secondary vibrating force of four-cylinder engine. However, regarding the design of crankshaft, connecting rod, piston and engine speed, the value of vibrating force is not specified. The balancer synchronizes with crankshaft in a manner that, when the centrifugal weights reach the low death point, a pair of pistons are located at the top death point (Goering and Hansen, 2014). Without the balancer, there occurs tractor vibration due to unavailability of damper and direct connection of engine to chassis (MF285 tractor engine is part of tractor chassis).

Ettefagh et al. (2008) studied knocking in petrol engines upon vibrating, analysing the cylinder block, and presented a parametrical model; they modelled vibrating signal of cylinder block with ARMA (Auto Regressive Moving Average) parametrical model. Moving average (MA) parameters, which were estimated, are very sensitive to knocking. Having revealed such parameters, it may be possible that knocking appears in primary function stages in spark ignition engines. The results show that the proposed method can reveal knocking with low sampling frequency via a simple software, which reduces the computation time and software costs. In this research, a new method of synchronous tachometer pulses with accelerometer sensor is introduced for estimating the knock-sensitive window (KSW). Taghizadeh et al. (2007) simulated the vibration of six-cylinder diesel engine using mixtures of diesel fuel and biodiesel via neural network. The results showed that the vibration remarkably decreases after engine serving, the fuel mixture has significant effect on vibration: B20 and B40 mixtures showed the least vibration; the most vibration occurred using B15 and B30 mixtures. The results showed that the best topology for predicting the RMS is neural network with 40-30-30-1 structure with trainlm training algorithm and logsis, tansig and pureline threshold functions.

Guzzomi et al. (2007) proved that torsional vibration in engines show certain phenomena, which are not common about vibration. These effects result from reciprocal mechanism geometry and are revealed with dynamic and kinematic analyses. Moment of inertia varies with crankshaft rotating and the results showed that vibration is influenced by the friction between cylinder and piston.

The goals of this research are as follows:

1. determining the relationship between different engine speeds and balancer function on those speeds;
2. determining the relationship between different engine loads and balancer function under these loads;
3. studying the vibration of MF285 tractor engine with and without balancer.

## Material and methods

Imbalance in rotating machines is one of the main factors of vibration. Simplified model of such devices is shown in Fig. 1. The entire device mass is M and there are two centrifugal masses of $m/2$, which rotate in opposite directions at constant angular velocity of $\omega$. Centrifugal force of $\frac{me\omega^2}{2}$ causes device mass stimulation. Two equal masses $m/2$ rotating in opposite directions are chosen from this direction and horizontal stimulation components are gathered and neutralize each other. However, vertical stimulation components are gathered and act along A-A axis in Fig. 1.

The total acting force of components along the vertical axis was calculated as follows:

$$F(t) = me\omega^2 \sin \omega t \qquad (1)$$

where:

$\omega$ – rotation velocity of balancing masses, rad·s$^{-1}$

$e$ – mass rotation radius, m

Tractors without chassis are equipped with a balancer unit (Fig. 2), which is installed in carter and moves via timing gears located in engine front. Fig. 2 shows that the balancer is composed of balancer shell, balancer weights, idle gear, spiral gear, spur gears of balancer weights, and balancer shaft. Balancer weights were installed on the shafts.

Single differential MF-285 tractor produced by Iran Tractor Company was used in this research. Table 1 displays the tractor technical details. This research utilizes a four-cylinder and four-stroke engine made by Motorsazan Company.

**Table 1** Technical details of engine in MF-285 tractor

| | |
|---|---|
| Made by Iran, Motorsazan Co., MTI440C-105AD Model | Weight: 380 kg |
| type of diesel Direct spraying:<br>Number of cylinders: 4 : 4<br>Compression ratio: 17.5 : 1<br>Cylinder diameter: 100 mm<br>Piston course: 127 mm<br>Volumetric capacity: 3.99 L | General dimensions<br>Length: 720 mm<br>Width: 550 mm<br>Height: 980 mm |
| Standard of pollution limitation<br>ECE-R96-Stage 2<br>ECE-R24 | Air inlet system: turbo charge and air to air cooler<br>Rotation direction: clockwise in front side<br>Cooling system: via water and equipped with oil cooling<br>Electrical system: 24 Volt |
| | Maximum power: 78 KW in 2200 rpm<br>Maximum torque: 375 NM in 1400 rpm |

In order to measure the torque (load), eddy-current dynamometer (E400 model) by Pouya microtools industries development company with capacity of 7000 rpm; the maximum torque of 400 Nm; and the maximum power of 150 hp was used and connected to flywheel. For the purposes of collecting the engine vibration signals, vibrometer equipped with piezoelectric sensor (Model AC102-1A) made by VMI factory was used (Fig. 3); this device comes with accuracy of 100 mv·g$^{-1}$ and sensitivity

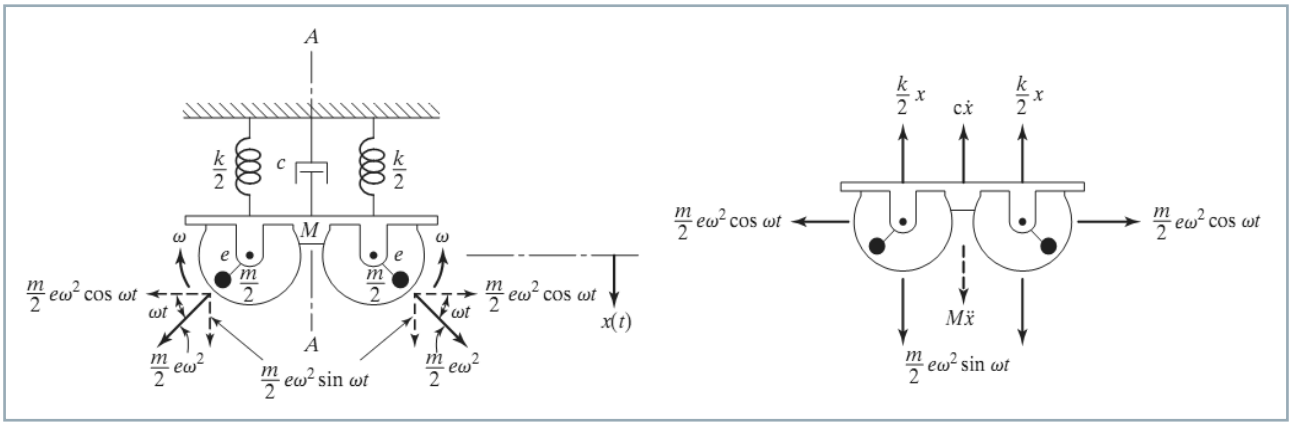


**Fig. 1** Total acting forces on rotating unbalanced masses (top) and acting forces in horizontal and vertical directions (bottom)

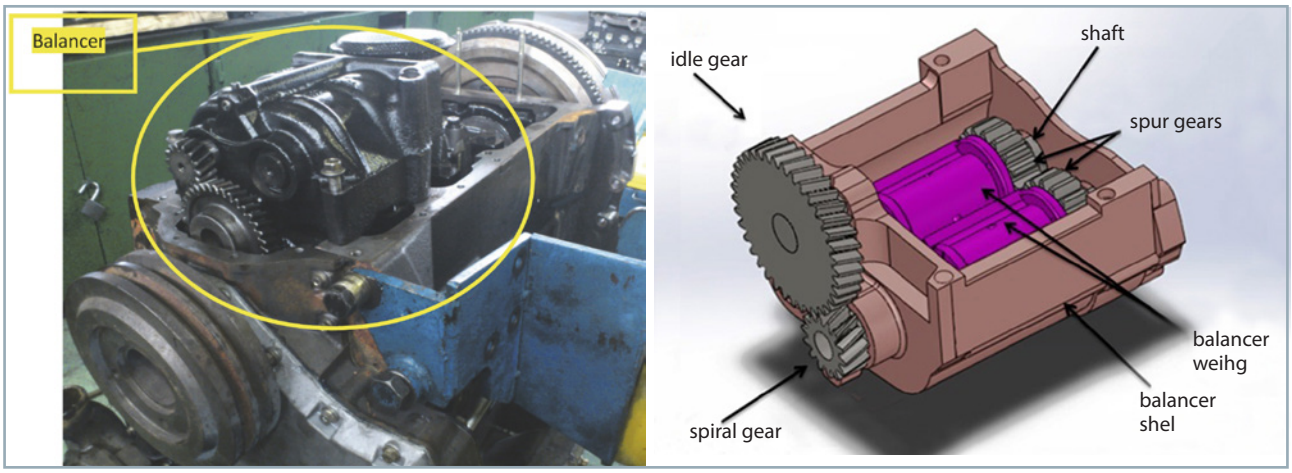


**Fig. 2** Balancer unit location in MF-285 tractor engine (left); View of balancer with its composing parts (right)

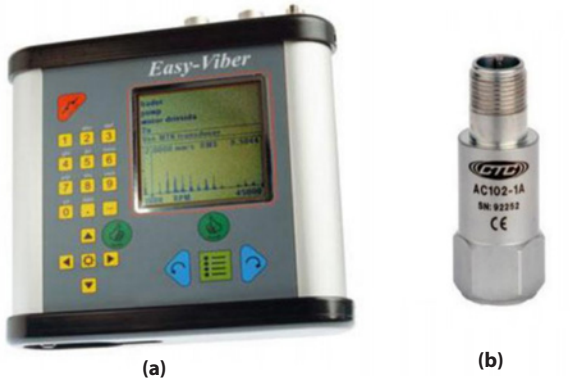


**Fig. 3** a) Vibrometer device; b) Vibrometer sensor

**Fig. 4** Vibrometer connection to engine

of ±10% and it can measure frequencies ranges from 0.5 to 15000 Hz. Its main advantages include that it has no compression, and high frequency domain and precision (Ahirrao et al., 2018).

The vibrometer connection was performed magnetically – there is no loosing between vibrometer and engine body, and the connecting place was fully clear. The connecting place of vibrometer to cylinder lies in fixed crankshaft bearing on flywheel side (ISO 8528-9, 2017), located 17 cm from cylinder side and 9 cm from cylinder floor in engine (Fig. 4). Calibration was performed according to the manufacturer's calibration certification, inserting relevant coefficients in the software.

Experiments were conducted at Motorsazan Company of Tabriz. Tractor engine was inside test cell platform under controlled conditions (Fig. 5). The engine studied was tested in full-load mode (mode in which the vehicle uses majority of power or torque of engine; it is like the vehicle would be going uphill) and no-load mode (no power is taken from engine, which means that the vehicle is either in neutral state or is going downhill). Firstly, in no-load mode, the vibration value was measured at engine speeds of 750 and 2400 rpm; subsequently, in full-load mode, the vibration value was measured at rotational speeds of 1400 and 2200 rpm. Finally, at a constant engine speed of 1400 rpm, the load on engine was decreased to half value, in order to compare the results of engine vibration with and without

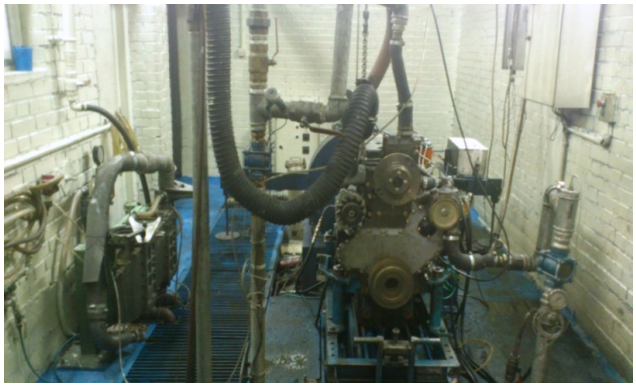

**Fig. 5** Test cell used for conducting experiments at Tabriz Motorsazan Company

balancer. The experiments mentioned were conducted for both modes with and without balancer. According to the claims of Tabriz Motorsazan Company, these modes have critical points allocating more vibration than other modes.

In order to express the RMS (root mean square) value of engine vibration, it is possible to employ three vibration parameters: displacement signal, vibrating speed signal and vibrating acceleration signal (Taghizadeh, 2011). For the purposes of analysis, the output signal RMS value of speed was obtained and used to investigate the engine vibration ($mm \cdot s^{-1}$). The RMS value of vibration was calculated as follows:

$$a_{RMS} = \sqrt{\frac{1}{n}\sum_{i=1}^{N} a_i^2}$$

where:

$a_{RMS}$ – root mean square of vibration values, $mm \cdot s^{-1}$
$a$ – vibrating data, $mm \cdot s^{-1}$
$N$ – total number of vibration data

## Results and discussion

For all modes, vibration data were recorded, and all graphs were extracted. Fig. 6 shows a sample of the results of vibrating speed signal of engine at 1400 rpm and load of 125 Nm.

### Laboratory results of balancer performance in different speeds with no load

Fig. 7 shows the engine operation in two modes with and without balancer at 750 rpm and 2400 rpm, and no load. In no-load mode and at 750 rpm, the balancer reduced the RMS of secondary vibration by 40.4%; at 2400 rpm and no load, it reduced the RMS value by up to 12.733%. Therefore, using balancer in no-load mode is more effective at lower speeds. In general, balancer helped to reduce the vibration by 28.8% on average. Kumhar et al. (2016) concluded that internal combustion engine on dynamics generates the first-order and second-order inertial forces depending upon the configuration. These are transmitted through the engine to vehicles' structure and finally to the driver compartment and cause discomfort. The secondary inertial forces from

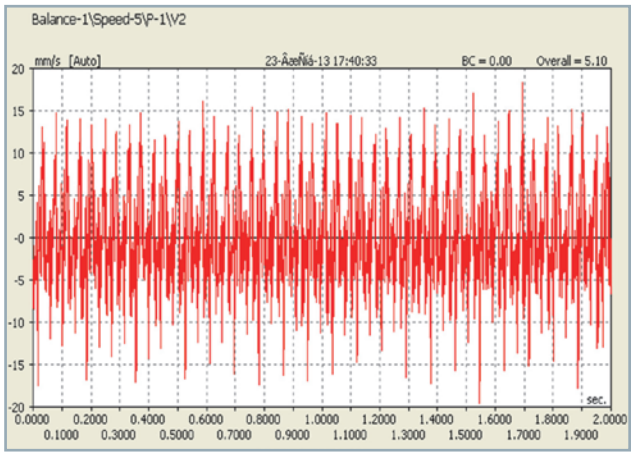


**Fig. 6** Vibrating speed (vertical axis) signal in experiment vs time (horizontal axis) at rotational speed of 1400 rpm and load of 125 Nm

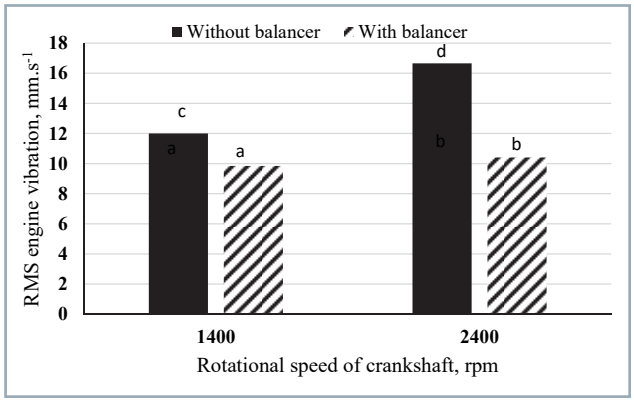


**Fig. 7** Balancer effect on decreasing engine vibration at two engine speeds (750 and 2400 rpm) without load – different alphabets of a, b, c, d show significant difference between treatments

in-line four-cylinder engine cause the vibration, which can be attenuated by installing the twin secondary balancer shaft rotating in opposite directions at twice the speed of crankshaft. Utilizing balancer at 2200 rpm, Kumhar et al. (2016) observed vibration reduction by 95%; at lower speed/high torque and high speed/low torque conditions at 1400 rpm and 2750 rpm, the vibration decrements were 90.82% and 94.4%, respectively. Gravalos et al. (2014) measured two types of tractor acceleration using the PSV-400 scanning laser vibrometer (Polytec) and the 4500A piezoelectric accelerometer, observing that the fibre-reinforced plastic hood (Lamborghini R6) showed the maximum vibration levels at 800 rpm, while the average acceleration values were greatly diminished at speed values exceeding 1000 rpm. The steel sheet hood of Renault 361 tractor showed similar vibration behaviour. Furthermore, Freydooni et al. (2012) came to similar results as previous authors – the minimum value of tractor vibration occurred at engine rotational speed of 1300–1400 rpm; after exceeding these values, the vibration increased proportionally to engine speed.

### Laboratory results of balancer function at different loads (125 and 250 Nm) and constant speed (1400 rpm)

Fig. 8 shows the engine operation in two modes – with and without balancer – and at torques of 250 and 125 Nm, and constant rotational speed of 1400 rpm. Fig. 8 indicates that increasing the load resulted in increased engine vibration. In this case, balancer utilization at 1400 rpm rotational speed and 125 Nm torque helped to reduce the RMS of secondary vibration by 38.9%. Meanwhile, RMS vibration reduction at 250 Nm was by 21.3% in comparison to no balancer mode. Therefore, using balancer at lower torque values was more effective for vibration reduction. Generally, in this mode, balancer helped to reduce the vibration by 29.6% on average. The vibration increment with increase in the engine load can be caused by increasing the intensity and pressure of combustion inside the cylinder, which results from more intense fuel spraying to combustion chamber and more significant piston impacts.

### Balancer effects on engine RMS vibration at full load and different rotational speeds

Fig. 9 presents the engine vibration in two modes (with and without balancer) at full load of 250 Nm, and rotational

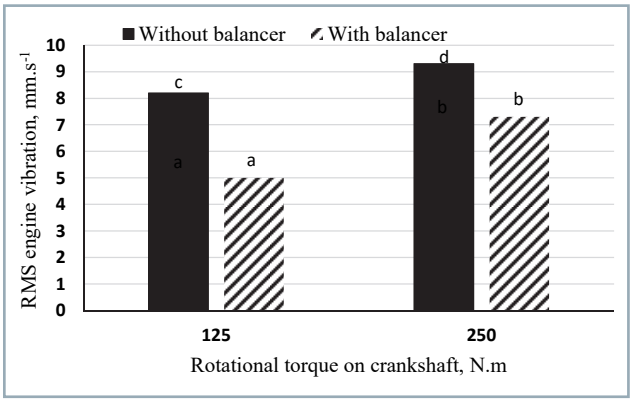


**Fig. 8** Balancer function at different loads and rotational speed of 1400 rpm – different alphabets of a, b, c, d show significant difference between treatments

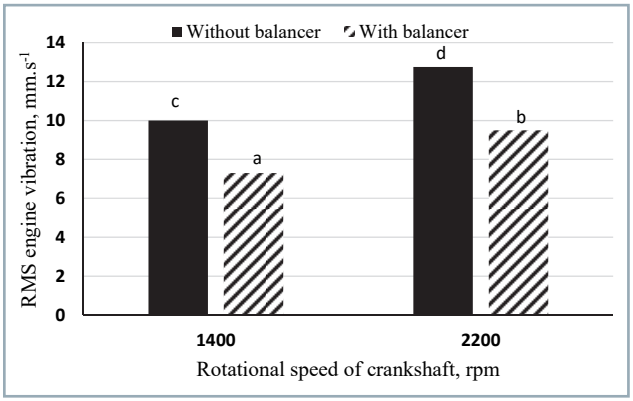


**Fig. 9** Balancer effects on decreasing the vibration at full load (250 Nm) at two rotational speeds (2200 and 1400 rpm) – different alphabets of a, b, c, d show significant difference between treatments

speeds of 1400 rpm and 2200 rpm. As it can be seen, increasing the rotational speed from 1400 to 2200 rpm increased the vibration in both modes – with and without balancer. Balancer utilization at full load helped to decrease the RMS of secondary vibration by 21.3% at 1400 rpm. At 2200 rpm, the decrement was 23.1%. Generally, in this mode, balancer utilization helped to reduce the vibration by 22.3% on average, and it was found that, in full-load mode, the balancer was more efficient at higher rotational speeds.

According to Fig. 9, in full-load mode, increasing the engine speed increased the RMS vibration of engine. Taghizadeh (2011) observed similar results in this area. Increase in vibration occurring while increasing the speed can be due to higher intensity and pressure of combustion inside the cylinder; in order to increase the engine speed, more fuel is sprayed to combustion chamber, resulting in increased combustion energy that inducts more force to engine body, which leads to amplifying of engine body vibration.

## Conclusion

- In terms of no-load mode, balancer utilization significantly helped to reduce the vibration in contrast to mode without balancer. Increasing the rotational speed caused the engine vibration to increase as well. Balancer utilization in no-load mode was more efficient at lower speeds. Generally, results showed that balancer is capable of vibration reduction by 28.8% in no-load mode.
- In terms of full-load mode, increasing the rotational speed resulted in increment in vibration in both modes with and without balancer. Generally, balancer helped to reduce the vibration by 22.3%. Results showed that the balancer was more efficient at high rotational speeds in full-load mode.
- At rotational speed of 1400 rpm, increasing the load from 125 to 250 Nm led to vibration increment in both modes with and without balancer. On average, balancer utilization helped to reduce the vibration by 29%. Under such conditions, balancer is more efficient at lower torques.

## References

AHIRRAO, N. S. – BHOSLE, S. P. – NEHETE, D. V. 2018. Dynamics and vibration measurements in engines. In Procedia Manufacturing, vol. 20, pp. 434–439.

BABAKHANI, N. G. – GHOBADIAN, B. – SALAHSHOOR, K. – MOHTASEBI. S. 2010. Vibration suppression and safety seat motion design of a hyper active seat. In Journal of Vibro engineering, vol. 2, no. 1, pp. 57–66.

BELLMANN, M. A. 2002. Perception of Whole Body Vibration: From Basic Experiments to Effects of Seat and Steering Wheel Vibrations on Passenger's Comfort Inside Vehicles. PhD Thesis, University of Oldenburg, Germany.

BREEZE, P. 2018. Piston Engine-Based Power Plants, Academic Press. 102 pp. ISBN 9780128129043.

BULGAKOV, V. – ADAMCHUK, V. – NOZDROVICKÝ, L. – IHNATIEV, Y. 2017. Theory of vibrations of sugar beet leaf harvester front-mounted on universal tractor. In Acta Technologica Agriculturae, vol. 20, no. 4, pp. 96–103.

CARLUCCI, A. P. – CHIARA, F. F. – LAFORGIA, D. 2006. Analysis of the relation between injection parameter variation and block vibration of an internal combustion diesel engine. In Journal of Sound and Vibration, vol. 295, no. 1–2, pp. 141–164.

ETTEFAGH, M. M. – SADEGHI, M. H. – PIROUZPANAH, V. – ARJMANDI-TASH, H. 2008. Knock detection in spark ignition engines by vibration analysis of cylinder block: A parametric modeling approach. In Mechanical Systems and Signal Processing, vol, 22, pp. 1495–1514.

FREYDOONI, M. – LORESTANI, A. N. – RABBANI, H. – JAVADIKIA, P. 2012. Measurement and analysis of vibration of operator in Universal 650, Massey Ferguson 285 & MF 299 Tractors. In International Journal of Mechanics and Applications, vol. 2, no. 5, pp. 88–92.

GOERING, C. E. – HANSEN, A. S. 2014. Engine power and tractor. American Society of Agricultural and Biological Engineers (ASABE), 4th edition, St. Joseph, Michigan.

GRAVALOS, I. – LOUTRIDIS, S. – GIALAMAS, T. – AUGOUSTI, A. – KATERIS, D. – XYRADAKIS, P. – TSIROPOULOS, Z. – LIBRA, M. 2014. Vibrational behavior of tractor engine hood. In Fine Mechanics and Optics, vol. 3, pp. 69–71

GUZZOMI, A. – HESTERMAN, D. – STONE, B. 2007. The effect of piston friction on the torsional natural frequency of a reciprocating engine. In Mechanical Systems and Signal, vol. 21, pp. 2833–2837.

ISO 8528–9. 2017. Reciprocating internal combustion engine driven alternating current generating sets – Part 9: Measurement and evaluation of mechanical vibrations.

ISO 2631–1. 2018. Mechanical vibration and shock – Evaluation of human exposure to whole-body vibration – Part 1: General requirements.

JUAN, X. – XUEHUI, Z. – JIANJUN, Z. – XUAN, L. 2017. Vibration characteristics of unbalance response for motorized spindle system. In Procedia Engineering, vol. 174, pp. 331–340.

KUMHAR, G. K. – SINGH, S. K. – BABHALE, T. 2016. Design and analysis of four cylinder diesel engine balancer shaft. In International Journal of Engineering Research & Technology, vol. 5, no. 8, pp. 103–108.

TAGHIZADEH, A. – TAVAKOLI HASHCHIN JASHGIN, T. – GHOBADIAN, B. 2007. Analyzing the daily exposure of user with two-wheel tractor vibrations. In Agricultural Engineering Researches Journal, vol. 8, no. 4, pp. 18–30.

TAGHIZADEH, A. 2011. Studying the Parameters of MF 399 Tractor Vibrations Signal via Diesel and Biodiesel Fuels. PhD dissertation, University of Tarbiat Modarres, Tehran.

DOI: 10.2478/ata-2021-0004



Acta Technologica Agriculturae 1
Nitra, Slovaca Universitas Agriculturae Nitriae, 2021, pp. 20–26

# MODELLING THE EFFECTS OF $AL_2O^3$-$SIO_2$ NANOCOMPOSITE ADDITIVE IN BIODIESEL–DIESEL FUEL ON DIESEL ENGINE PERFORMANCE USING HYBRID ANN-ABC

Maryam JABRAEILI, Razieh POURDARBANI*, Bahman NAJAFI, Ali NEMATOLLAHZADEH

University of Mohaghegh Ardabili, Ardabil, Iran

Yearly, large amounts of waste cooking oil are produced, which are discharged to urban sewage system. However, majority of them is recyclable and can be re-used as biodiesel fuel. When using biodiesel fuels, one way to improve the engine performance is to use nano additives. This study investigates the biodiesel fuel with different ratios of $Al_2O_3$-$SiO_2$ nanocomposite additive ($Al_{0\%}$-$Si_{100\%}$, $Al_{25\%}$-$Si_{75\%}$, $Al_{50\%}$-$Si_{50\%}$, $Al_{75\%}$-$Si_{25\%}$ and $Al_{100\%}$-$Si_{0\%}$) at full load and four different nanocomposite concentrations (30, 60, 90 and 120 ppm). The Hybrid ANN-ABC modelling was conducted for two cases: a) finding and applying the most effective properties as network inputs; and b) total properties as inputs showed that the most effective properties have higher performance. The fuels $B_5Al_{60}Si_{60}$ and $B_5Al_9Si_{21}$ showed the highest brake power; the fuels $B_5Al_0Si_{60}$ and $B_5Al_{120}Si_0$ showed the lowest brake power, indicating that the interactions of nanoparticles in the composite mode had positive effects on brake power. The performance improvement using nano-composite additive was more than that of the nanoparticles individually.

**Keywords:** brake power; biofuel; performance; oil

The decline in fossil energy sources and their environmental impacts have led communities to consider renewable energy alternatives. One of these renewable sources is biodiesel fuel, which has various methods of production; and various experiments have been conducted on its effects on diesel engine performance and emissions (Alibaba et al., 2020; Čedík et al., 2018). Furthermore, nano-based science is rapidly advancing in all fields, including biofuels. Diesel fuel shows a different behaviour when combined with additives, which can improve the performance and emission in specific cases (Khalife et al., 2017).

Sajith et al. (2010) investigated the effect of Cerium oxide nanoparticles (CeNPs) on biodiesel in single-cylinder direct injection diesel engines at 1500 rpm. An increasing trend in the physical and chemical properties of fuel, such as flash point, viscosity and oscillation, was observed. The results showed that there was an average reduction of 25% in HC emissions. CeNPs additive reduced $NO_x$ emissions by 30%. However, the effect of fuel additives on CO reduction was not significant. Bhagwat et al. (2015) investigated graphene nanoparticles additive to diesel--biodiesel blended fuel (25 and 50 ppm) in a single cylinder diesel engine. Fangsuwannarak and Triratanasirichai (2013) evaluated the properties of biodiesel and $TiO_2$ additive impacts on the diesel engine. The results showed that the performance and emissions were improved; the fuel quality increased by 0.1%. In addition, kinematic viscosity was decreased and cetane number was increased. Silva et al. (2015) used $TiO_2$ nanoparticles additive in diesel engine. The results show improvement in fuel properties. Aalam and Saravan (2017) reported significant increase in thermal efficiency and a slight decrease in harmful emissions (such as CO, HC and soot) using $Al_2O_3$ NPs additive to the $B_{20}$ biodiesel blend. Prabu and Anand (2015) reported an improvement in performance of a single-cylinder diesel engine when they used $Al_2O_3$ and $CeO_2$. Aghbashlo et al. (2019) investigated the effect of diesel-biodiesel fuel with CeNPs additive (0 and 90 ppm) on engine performance. The results showed that engine load and fuel type strongly influence the exergy-based stability indices. In general, increasing the engine load continuously decreases the exergy efficiency. Their proposed blended fuel showed much better environmental performance than pure diesel fuel.

According to previous research, performance improvement using nanoparticle additives to biodiesel fuel is obvious, however, there is lack of information in terms of direct addition of nanocomposites to diesel-biodiesel fuel. Therefore, this study investigates the addition of $Al_2O_3$-$SiO_2$ nanocomposite (at different ratios) to disesel-B5 blended fuel and its effect on diesel engine performance.

## Material and methods

### Fuel sample preparation

Biodiesel fuel was produced from waste cooking oil by transesterification, and conventional Iranian diesel fuel was used for referential purposes. Fuel specifications complied with ASTMD 6751-20a. After ensuring that the produced biofuel meets the required standards, the diesel-biodiesel

**Contact address:** Razieh Pourdarbani, University of Mohaghegh Ardabili, Department of Biosystem Engineering, Ardabil, Iran

**Table 1** Fuel samples and ratio of nanoparticle composition

| No. | Sample | Final ppm | Al (ppm) | Al% | Si (ppm) | Si% | Biodiesel% |
|---|---|---|---|---|---|---|---|
| 1 | $B_5Al_{30}Si_0$ | 30 | 30 | 100 | 0 | 0 | 5 |
| 2 | $B_5Al_{21}Si_9$ | | 21 | 75 | 9 | 25 | |
| 3 | $B_5Al_{15}Si_{15}$ | | 15 | 50 | 15 | 50 | |
| 4 | $B_5Al_9Si_{21}$ | | 9 | 25 | 21 | 75 | |
| 5 | $B_5Al_0Si_{30}$ | | 0 | 0 | 30 | 100 | |
| 6 | $B_5Al6_0Si_0$ | 60 | 60 | 100 | 0 | 0 | 5 |
| 7 | $B_5Al_{42}Si_{18}$ | | 42 | 75 | 18 | 25 | |
| 8 | $B_5Al_{30}Si_{30}$ | | 30 | 50 | 30 | 50 | |
| 9 | $B_5Al_{18}Si_{42}$ | | 18 | 25 | 42 | 75 | |
| 10 | $B_5Al_0Si6_0$ | | 0 | 0 | 60 | 100 | |
| 11 | $B_5Al_{90}Si_0$ | 90 | 90 | 100 | 0 | 0 | 5 |
| 12 | $B_5Al6_3Si_{27}$ | | 63 | 75 | 27 | 25 | |
| 13 | $B_5Al_{45}Si_{45}$ | | 45 | 50 | 45 | 50 | |
| 14 | $B_5Al_{27}Si6_3$ | | 27 | 25 | 63 | 75 | |
| 15 | $B_5Al_0Si_{90}$ | | 0 | 0 | 90 | 100 | |
| 16 | $B_5Al_{120}Si_0$ | 120 | 120 | 100 | 0 | 0 | |
| 17 | $B_5Al_{84}Si_36$ | | 84 | 75 | 36 | 25 | |
| 18 | $B_5Al_{60}Si_{60}$ | | 60 | 50 | 60 | 50 | |
| 19 | $B_5Al_36Si_{84}$ | | 36 | 25 | 84 | 75 | |
| 20 | $B_5Al_0Si_{120}$ | | 0 | 0 | 120 | 100 | |
| 21 | $B_5$ | | --- | 0 | --- | 0 | 5 |
| 22 | D | | --- | 0 | --- | 0 | 0 |

blended fuel was prepared ($B_5$). Different ratios of $Al_2O_3$ and $SiO_2$ were composited at 30, 60, 90 and 120 ppm. Desired concentrations of each nanoparticle were measured by digital scale (Sartorius Corporation) and added to the fuel, and an ultrasonic probe (Ultrasonic Homogenizer 300R) was used for homogenization. Different capacities of ultrasonic waves were tested in order to disperse these nanoparticles, and finally, ultrasonic waves of 400 W were used for each sample for 3 minutes. Ultimately, the 22 fuel samples (Table 1) were prepared for the experiments. The nanoparticles were made in Merck CO. The physical properties of these nanoparticles are presented in Table 2. The engine tested was the single-cylinder Kirloskar Oil Engines Ltd made in India (Fig. 1) that was coupled to a jb/t-200 power generator, which was connected to a load cell by an arm. The electricity generated was transmitted to a power heater consumer. As the power consumption changed, the engine came under

**Table 2** Characteristics of the nanoparticles used

| Characteristics | $SiO_2$ | $Al_2O_3$ |
|---|---|---|
| Pure (%) | 99.5 | 99 |
| Size (nm) | 20 | 20 |
| Specific surface area ($m^2 \cdot g^{-1}$) | 210 | 200 |
| The amount of $O_2$ (%) | 53.26 | 47.07 |
| The amount of minerals (%) | 46.74 | 52.93 |
| Manufacturing country | Germany | Germany |

**Fig. 1** Diesel engine test stand

a load. Fuel consumption was also measured by a graduated cylinder. These experiments were performed under full load conditions at a constant speed of 1,500 rpm.

## Modelling using artificial neural network

### Extracted properties of each sample fuel

The properties used as predictor inputs were fuel type; density; cloud point; viscosity; flash point; heating value; oxygen in the exhaust gases; and oil temperature and relative humidity of the outdoor air.

### Method for the most efficient property selection

Since the measurement of all properties is costly and time consuming, finding the most effective among all properties can be both time and cost effective. For this reason, a hybrid Artificial Neural Network – Differential Evolution (ANN-DE) was used to select the most effective properties. Similarly to many other optimization algorithms, the DE algorithm is based on population and random behaviour proposed by Storn and Price (1996). This algorithm consists of two basic steps of initialization and evolution. While the optimization problem does not have any basic information, it must first generate a random population and then, to optimize the problem, the population members are improved through mutation, and selection process is conducted until the optimization is achieved. In order to select the effective feature, the extraction feature was firstly considered a vector. Subsequently, other vectors of different sizes were selected using DE algorithm and sent to ANN. Artificial Neural Network – Multi Layer Perceptron (ANN-MLP) divides all data into three categories; 1) the first contains 70% of the data for training, 2) the second contains 15% of the data for validation, and 3) the third contains 15% of the data for testing. Finally, the mean squared errors of each vector are sent to the ANN-MLP using the DE algorithm. Each vector with the least MSE was selected as the effective property. Table 3 shows the ANN-MLP properties used to select the effective properties.

**Table 3** Configuration of hidden layer ANN used to select the most effective properties

| Features | The value or type of feature |
|---|---|
| **Number of neurons** | 10 |
| **Number of layers** | 1 |
| **Transfer function** | tansig |
| **Back-propagation training network function** | trainlm |
| **Back-propagation weight/bias learning function** | learngdm |

### Predicting the brake power using total properties

Hybrid Artificial Neural Network – Artificial Bee Colony (ANN-ABC) was used to predict the brake power of different fuels. Hybrid ANN-ABC algorithm is inspired by the way of bee behaviour in nature. In the beehive, a number of bees are tasked with searching for food sources, which means producing initial responses in the optimized state. After identifying the food sources, the bees return to the hive and inform other bees, so-called 'scout bees' that are sent to these areas to check the amount of nutrients in areas and their quality, and then return to the hive. This will continue until the food source is identified in great quantity and quality. This operation in the optimization mode means finding the optimal points (Hussain et al., 2016). The ANN-MLP has 5 adjustable parameters including the number of neurons; number of layers; transfer function; back propagation training function; back propagation weight/bias learning function, optimal values of which guarantee high performance (Table 4).

**Table 4** Values of hidden layer of MLP-ANN for prediction of brake power using total properties

| Features | The value or type of feature |
|---|---|
| **Number of neurons** | first layer: 6<br>second layer: 9<br>third layer: 18 |
| **Number of layers** | 3 |
| **Transfer function** | first layer: netinv<br>second layer: satlins<br>third layer: compet |
| **Back propagation network training function** | traingdx |
| **Back-propagation weight/bias learning function** | learnlv1 |

### Brake power prediction using the most effective properties

The method used for this section is the same as in the previous section. Table 5 gives the optimal structure of the hidden layers of MLP-ANN arranged by ABC algorithm.

**Table 5** Hidden layer of MLP-ANN to predict brake power using the most effective properties

| Features | The value or type of feature |
|---|---|
| **Number of neurons** | first layer: 14<br>second layer: 18<br>third layer: 13 |
| **Number of layers** | 3 |
| **Transfer function** | first layer: radbas<br>second layer: hardlim<br>third layer: radbas |
| **Back propagation network training function** | traingda |
| **Back propagation weight/bias learning function** | learnlv2 |

### Performance evaluation parameters of hybrid ANN-ABC

Performance evaluation parameters of hybrid ANN-ABC to predict the brake power include the coefficient of determination ($R^2$); sum squared error (SSE); mean absolute error (MAE); mean square error (MSE); root mean square error (RMSE) (Sabzi et al., 2013; Javadikia et al, 2018).

## Results and discussion

### Performance of hybrid ANN-ABC in predicting brake power at 1000 iterations using total properties

According to Fig. 2, the coefficient of regression is above 0.982. MES, RMES, MAE, SSE and $R^2$ for the best training condition were 0.0091, 0.0956, 0.0533, 0.1188 and 0.9636, respectively. Fig. 3 represents the actual value versus the estimated value of the brake power using the total properties in the best state of training, indicating that the actual and estimated values are close to each other in majority of samples.

### Performance of hybrid ANN-ABC in brake power prediction in the best state of training using the most effective properties

Fig. 4 shows the scatter plot regression analysis estimated by the hybrid ANN-ABC using the most effective properties and the actual brake power of different fuels in the best state of training. The coefficient of regression value is above 0.999 for the best training mode. MES, RMES, MAE, SSE and $R^2$ were 0.0061, 0.0782, 0.0407, 0.094 and 0.9706, respectively.

Fig. 5 shows the actual value versus the mean value of brake power (test set) by the hybrid ANN-ABC using the most effective properties in the best state of training. According to Fig. 5, the actual and estimated values are close together, indicating that the proposed method can predict the brake power using the most effective properties.

### Comparison of the brake power predicted using total properties and the most effective properties

Table 6 gives the mean and standard deviations of performance evaluation parameters in estimating the brake power for two different input sets, including the total and most effective properties at 1000 iterations. As it can be observed, the performance of the most effective properties is higher than in the other mode, i.e., the expected brake power is closer to the actual value due to the contradiction between the total properties.

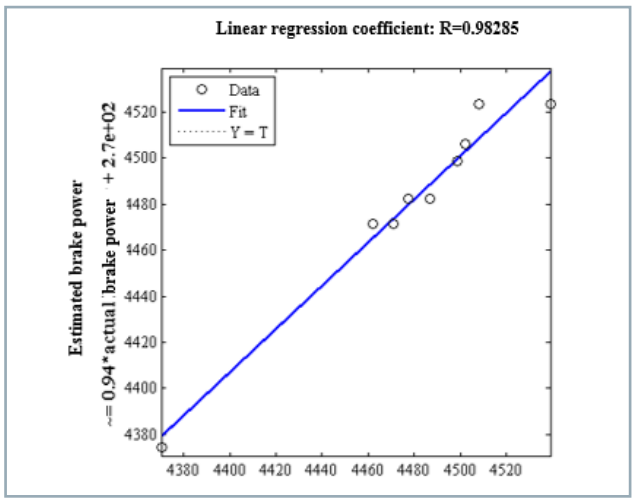


**Fig. 2** Scatter plot regression analysis estimated by the hybrid ANN-ABC using the total properties and the actual brake power of different fuels in the best state of training

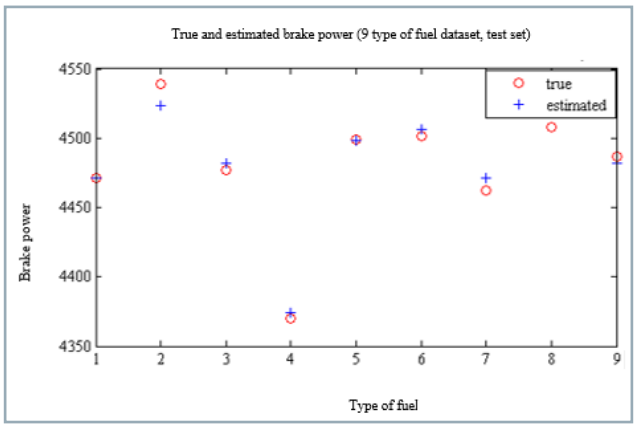


**Fig. 3** Actual value versus estimated value of the brake power by the hybrid ANN-ABC using the total properties in the best state of training

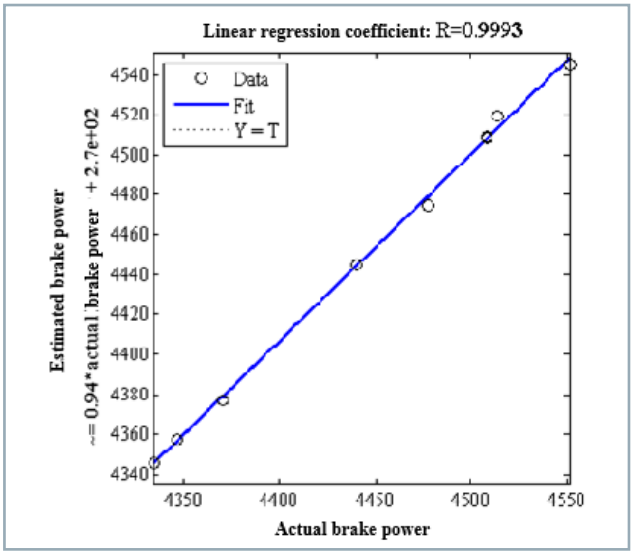


**Fig. 4** Scatter plot regression analysis estimated by the hybrid ANN-ABC using the most effective properties and actual brake power of different fuels in the best state of training

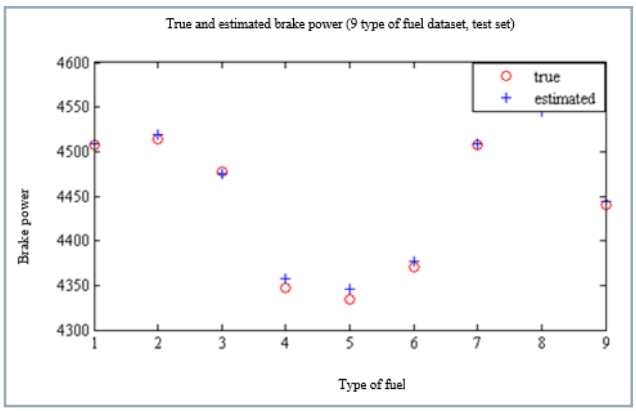


**Fig. 5** Actual value versus the mean value of brake power by hybrid ANN-ABC using the most effective properties in the best state of training

**Table 6** Comparison of predicted brake power using the total properties and most effective properties at 1000 iterations

| Properties | Criterion | MSE | RMSE | MAE | SSE | *R* | $R^2$ |
|---|---|---|---|---|---|---|---|
| **Total properties** | Mean | 0.0278 | 0.1598 | 0.1228 | 0.3611 | 0.9545 | 0.9114 |
| | SD | 0.0139 | 0.0474 | 0.0429 | 0.1809 | 0.0188 | 0.0360 |
| **Effective properties** | Mean | 0.0126 | 0.1076 | 0.0712 | 0.1645 | 0.9792 | 0.9590 |
| | SD | 0.0067 | 0.0326 | 0.0267 | 0.0909 | 0.0104 | 0.0203 |

**Table 7** Actual value, mean and standard deviation of the predicted brake power value of the 22 fuel samples using the total and most effective properties

| Fuel no. | Measured value | Predicted value using total properties | Predicted value using the most effective properties |
|---|---|---|---|
| **1** | 4477.33 | 4482.66 ±2.256 | 4476.59 ±3.38 |
| **2** | 4486.46 | 4473.28 ±10.66 | 4490.98 ±7.19 |
| **3** | 4498.65 | 4492.85 ±7.91 | 4496.34 ±3.66 |
| **4** | 4551.22 | 4541.52 ±4.61 | 4542.03 ±8.62 |
| **5** | 4440.55 | 4435.79 ±10.15 | 4433.11 ±12.23 |
| **6** | 4462.015 | 4479.66 ±15.57 | 4464.86 ±4.08 |
| **7** | 4471.13 | 4485.16 ±14.04 | 4473.71 ±4.00 |
| **8** | 4370.33 | 4371.34 ±17.74 | 4372.64 ±4.31 |
| **9** | 4492.66 | 4519.92 ±5.86 | 4494.76 ±4.76 |
| **10** | 4334.57 | 4345.56 ±9.13 | 4336.98 ±4.68 |
| **11** | 4416.33 | 4388.40 ±28.54 | 4420.58 ±18.96 |
| **12** | 4501.82 | 4498.96 ±5.82 | 4503.27 ±3.63 |
| **13** | 4504.87 | 4497.44 ±8.48 | 4494.76 ±4.76 |
| **14** | 4507.92 | 4512.59 ±6.29 | 4502.19 ±6.98 |
| **15** | 4507.92 | 4477.18 ±2.05 | 4503.66 ±3.61 |
| **16** | 4346.73 | 4351.00 ±6.14 | 4349.413 ±9.16 |
| **17** | 4477.33 | 4485.42 ±5.49 | 4488.28 ±7.25 |
| **18** | 4560.47 | 4542.90 ±4.65 | 4557.88 ±6.59 |
| **19** | 4507.92 | 4539.98 ±4.17 | 4505.39 ±28.84 |
| **20** | 4514.14 | 4495.78 ±5.61 | 4522.91 ±26.59 |
| **21** | 4538.87 | 4510.45 ±6.65 | 4533.75 ±10.72 |
| **22** | 4486.56 | 4482.84 ±2.17 | 4489.481 ±12.14 |

Table 7 gives the actual value, mean and standard deviations for the predicted brake power of 22 fuel samples using two different sets, including the total and most effective properties selected by the hybrid ANN-ABC. Since each execution contains 9 test samples, there would be 9,000 in 1,000 iterations, and since there were only 22 samples, there would be more than 409 iterations per sample. Finally, Fig. 6 illustrates the actual brake power minus the brake power estimated by hybrid ANN-ABC for 22 fuels using the total and most effective properties. Fig. 6 utilizes the most effective properties as inputs, and the samples have more compact box diagrams than the other mode, indicating that the most effective properties have higher performance than total properties.

### Effects of different ratios of $Al_2O_3$-$SiO_2$ composite additive to diesel-biodiesel fuel on brake power

In this study, $Al_2O_3$ and $SiO_2$ nanoparticles had similar size and specific surface area. Therefore, the chemical properties of nanoparticles are expected to be the only factors affecting the fuel properties and exhaust gases. Considering the Fig. 7, it is clear that $B_5Al_{60}Si_{60}$ and $B_5Al_9Si_{21}$ samples have the highest brake power, and $B_5Al_0Si_{60}$ and $B_5Al_{120}Si_0$ have the lowest brake power. Sample B5 improved the brake power compared to pure diesel fuel because of its oxygen content. At the concentration of 30, 60 and 90 ppm, the highest brake power was obtained in sample $B_5Al_9Si_{21}$ (70% $SiO_2$, 30% $Al_2O_3$ and 5% biodiesel). At 120 ppm, the highest brake power was obtained in the $B_5Al_{60}Si_{60}$ sample, i.e., addition of $Al_2O_3$-$SiO_2$ composite has improved the brake power more

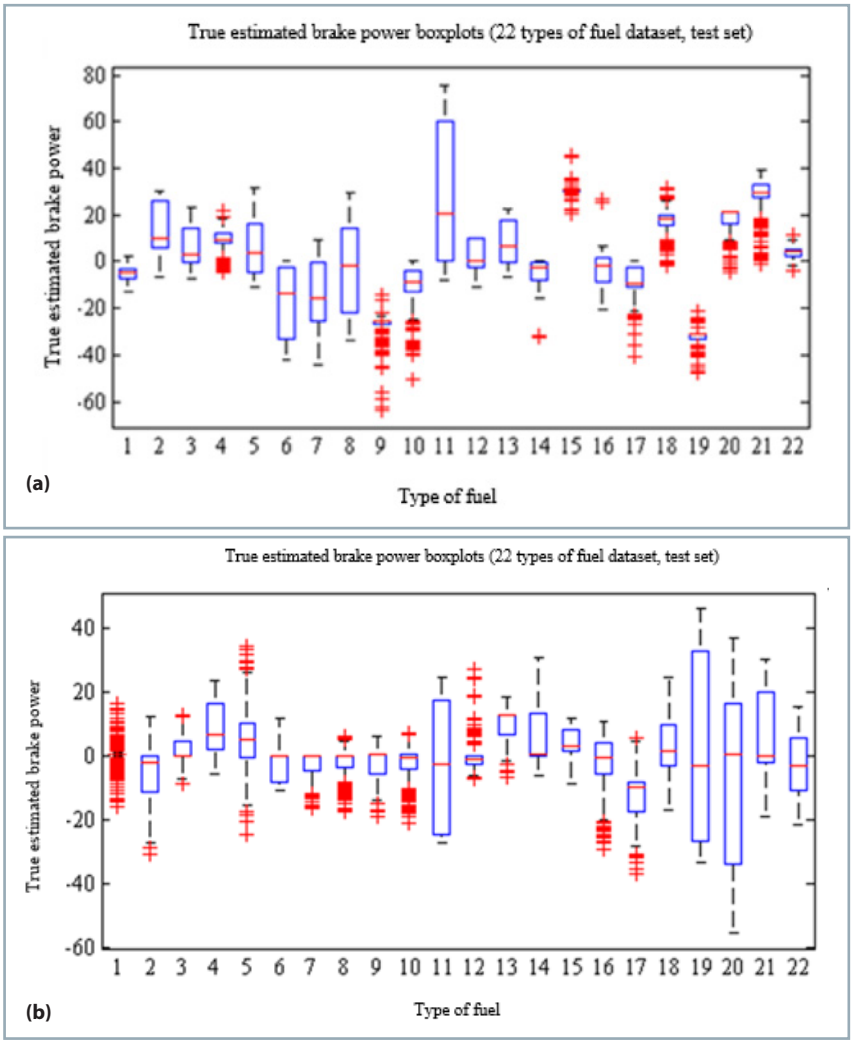


**Fig. 6** (a) Box diagrams of brake power for 22 fuel samples using total properties, (b) Box diagrams of brake power for 22 fuel samples using effective properties

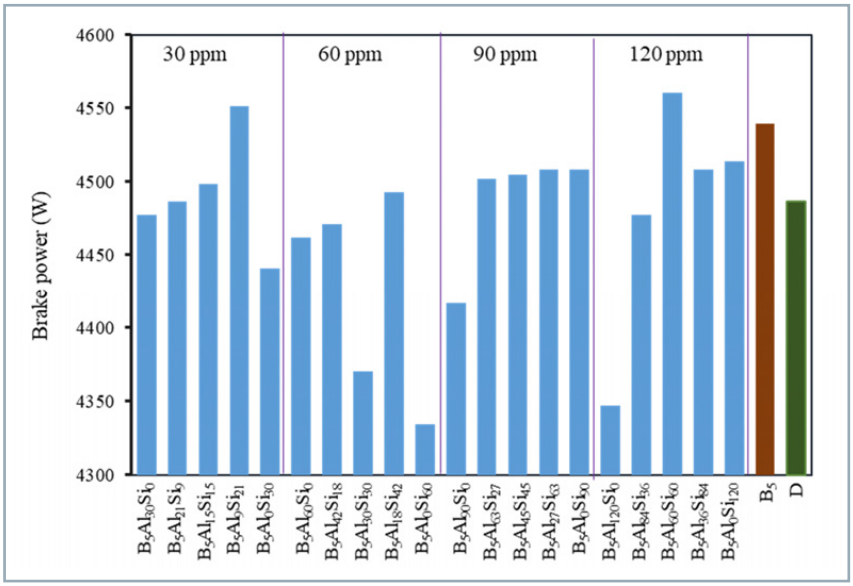


**Fig. 7** Effect of different ratios of $Al_2O_3$-$SiO_2$ nano-composite additive to diesel-biodiesel fuel on brake power

than separate addition of either $Al_2O_3$, or $SiO_2$. The nanoparticle interactions in the composite had positive effects on the brake power. Therefore, at 30 ppm, the brake power increased with increasing Si/Al ratio; however, at zero alumina content, the brake power decreased. This may be due to the elimination of the catalytic effect of $Al_2O_3$ nanoparticles. At 60 ppm, a similar increase was observed, with a significant decrease in brake power at 50% of the nanoparticles, which could be due to the accumulation of $SiO_2$ nanoparticles around the $Al_2O_3$, preventing catalytic activity. On the contrary, at 90 ppm, the increasing trend in brake power at high ratios of Si/Al has reached an almost constant value, which could be due to the catalytic compensation of alumina by the silica nanoparticles oxygen. However, at 120 ppm, when the nanoparticles were 50% ($B_5Al_{60}Si_{60}$), the increasing trend in brake power was associated with a jump, which could be a result of facilitating the dispersion and stabilization of $Al_2O_3$ nanoparticles by $SiO_2$ nanoparticles. In general, the effect of $Al_2O_3$ and $SiO_2$ nanoparticles can be a result of the simultaneous effect and sometimes aspects such as (1) the catalytic properties of $Al_2O_3$ nanoparticles; (2) oxygen supply by nanoparticles for CO oxidation and against the oxygen uptake for NO reduction; and 3) $SiO_2$ nanoparticles accumulation away from $Al_2O_3$ nanoparticles, which prevents the catalytic activity (Bielanski and Haber, 1990).

## Conclusion

Currently, one of the most important challenges is to maximize the brake power in diesel engines. The modelling results of brake power by ANN-ABC using the effective properties as the network input indicate that these samples had more compact box diagrams than the ones used for the total properties, suggesting the high performance.

The results showed that the highest brake power was obtained in $B_5Al_9Si_{21}$ at 30, 60 and 90 ppm. At 120 ppm, the highest brake power was obtained in $B_5Al_{60}Si_{60}$, leading to an increase of 1.44% in torque and an increase of 1.64% in the braking power relative to diesel fuel. On the other hand, it must

be mentioned that, unlike nano-alumina, there was no regular decreasing or increasing trend at different ratios of 30, 60, 90 and 120 with the addition of nanosilica. In contrast to alumina nanoparticles, silica nanoparticles improved the performance of diesel engine and achieved acceptable success in improving the level of produced pollutants. The interactions between the nanoparticles in the composite state had positive effects on the brake power.

## References


AALAM, C. S. – SARAVANAN, C. G. 2017. Effect of nano metal oxide blended Mahua biodiesel on CRDI diesel engine. In Ain Shams Engineering Journal, vol. 8, no. 4, pp. 689–696.

AGHBASHLO, M. – TABATABAEI, M. – KHALIFE, E. – NAJAFI, B. – MIRSALIM, M. – MOHAMMADI, P. – ROODBAR, T. – KHOUNANI, Z. 2019. A novel emulsion fuel containing aqueous nano cerium oxide additive in diesel–biodiesel blends to improve diesel engines performance and reduce exhaust emissions: Part II – Exergetic analysis. In Fuel, vol. 205, pp. 262–271.

ALIBABA, M. – POURDARBANI, R. – KHOSHGOFTARMANESH, M.H. – OCHOA, G.V. – DUARTE FORERO, J. 2020. Thermodynamic, exergo-economic and exergo-environmental analysis of hybrid geothermal-solar power plant based on ORC cycle using emergy concept. In Heliyon, vol. 6, no. 4, e03758.

ASTMD 6751-20a. Standard Specification for Biodiesel Fuel Blend Stock (B100) for Middle Distillate Fuels. Available at: https://www.astm.org/Standards/D6751.htm

BIELANSKI, A. – HABER, J. 1990. Oxygen in Catalysis. Boca Raton: CRC Press, 488 pp.

BHAGWAT, V. A. – PAWAR, C. – BANAPURMATH, N. R. 2015. Graphene nanoparticle – biodiesel blended diesel engine. In International Journal of Engineering Research & Technology (IJERT), vol. 4, no. 2, 75–78.

ČEDÍK, J. – PEXA, M. – PETERKA, B. – HOLŮBEK, M. – MADER, D. – PRAŽAN, R. 2018. Effect of biobutanol-sunflower oil-diesel fuel blends on combustion characteristics of compression ignition engine. In Acta Technologica Agriculturae, vol. 21, no. 4, pp. 130–135.

HUSSAIN, A. – ZHANG, M. – ÜCPUNAR, H. K. – SVENSSON, T. – QUILLERY, E. – GOMPEL, N. – IGNELL, R. – GRUNWARD, I. C. 2016. Ionotropic chemosensory receptors mediate the taste and smell of polyamines. In PLoS Biology, vol. 14, no. 5, e1002454.

JAVADIKIA, H. – SABZI, S. – ARRIBAS, J. 2018. An automatic and non-intrusive hybrid computer vision system for the estimation of peel thickness in Thomson orange. In Spanish Journal of Agriculture, vol. 16, no. 4, 15 pp.

FANGSUWANNARAK, K. – TRIRATANASIRICHAI, K. 2013. Improvements of palm biodiesel properties by using nano-$TiO_2$ additive, exhaust emission and engine performance. In Optics & Mechatronics, no. 43, pp. 111–118.

KHALIFE, E. – TABATABAEI, M. – NAJAFI, B. – MIRSALIM, S. M. – GHAREHGHANI, A. 2017. A novel emulsion fuel containing aqueous nano cerium oxide additive in diesel–biodiesel blends to improve diesel engine performance and reduce exhaust emissions: Part II – Exergetic analysis. In Fuel, vol. 205, pp. 262–271

PRABU, A. – ANAND, R. B. 2015. Emission control strategy by adding alumina and cerium oxide nano particle in biodiesel. In Journal of Energy Institute, vol. 89, no. 3, pp. 366–372.

SABZI, S. – JAVADIKIA, H. – RABBANI, H. – ADELKHANI, A. 2013. Mass modeling of Bam orange with ANFIS and SPSS methods for using in machine vision. In Measurement, vol. 46, no. 9, pp. 3333–3341.

SAJITH, V. – SOBHANN, C. B. – PETERSON, G. P. 2010. Experimental investigation on the effect of cerium oxide nanoparticle fuel additive on biodiesel. In Advances in Mechanical Engineering, vol. 47, no. 1, pp. 7–16.

SILVA, R. D. – BILNU, K. G. – BHAT, T. 2015. Performance and emission characteristics of a C.I. engine fuelled with diesel and $TiO_2$ nanoparticles as fuel additive. In Materials Today: Proceedings, vol. 2, no. 4, pp. 3728–3725.

STORN, R. – PRICE, K. 1996. Differential evolution – a simple and efficient heuristic for global optimization over continuous spaces. In Journal of Global Optimization, vol. 11, pp. 341–359.

DOI: 10.2478/ata-2021-0005



Acta Technologica Agriculturae 1
Nitra, Slovaca Universitas Agriculturae Nitriae, 2021, pp. 27–34

# DISTRIBUTED ACTIVATION ENERGY MODELLING USING A PARABOLIC HEATING PROFILE

Alok DHAUNDIYAL[1]*, Suraj B. SINGH[2]

[1]Szent István University, Gödöllő, Hungary
[2]Govind Ballabh Pant University of Agriculture and Technology, Pantnagar, UK, India

This work investigates the thermal decomposition of forest waste for a non-linear temperature distribution inside the pyrolysis reactor. Quantitative analysis of the distributed activation energy model is explained graphically. It has been assumed that thermal profile varies according to the general parabolic equation with the initial condition (0, $T_0$). The approximated solution of the non-analytical integral is determined by the Laplace integral method. The integral limit for the distributed activation energy model (DAEM) is found to vary from 211 to 810 kJ·mol$^{-1}$; whereas the frequency factor (the first-order reactions) for the corresponding range of the activation energy lies in the domain of 400–2000 min$^{-1}$. The acceleration in the char formation has been found for the reactions other than that of the first order.

**Keywords:** biomass; pyrolysis; distributed activation energy model; thermal history; kinetic parameters

There is an abundance of forestry residues that contains significant energy potential. However, the non-utilization of forest waste is causing ecological and financial complications. Pine needles are one of such waste materials that not only ruin the virgin forest through forest inferno, but also affect the fertility of forest land (Dhaundiyal and Gupta, 2014). Another scope of using biological waste (Lee et al., 2019) is to curtail the depletion of fossil fuel reservoirs. It has become difficult to curb emission for some of the fastest growing economies of the world like China and India. However, India introduced carbon taxation and other measures to limit its emission, which is well summarised by Dhaundiyal and Tewari (2015).

There are numerous possible ways to transform biomass into beneficial products. One of the possible ways is the thermochemical transformation of biomass into useful end products. During pyrolysis, biomass decomposes into liquid oils, volatile gases, and chars. The detailed study of pyrolysis has been reported by Di Blasi (2008) and White et al. (2011). These thermochemical processes depend on the intensive properties of a reactor used for thermal decomposition; therefore, it is necessary to examine the effect of thermal profile on the mass-loss pattern.

Practically, it has been found that the industrial reactors often work on higher thermal history, which may or may not be linear (Dhaundiyal et al., 2020; Dhaundiyal and Toth, 2020). It becomes necessary to model the pyrolysis reactions taking place at a higher thermal regime. For the cubic thermal profile in a pilot-scale reactor, the activation energy for the hardwood chips is 177.1 kJ·mol$^{-1}$, which is quite near to the values (173–176 kJ·mol$^{-1}$) obtained by other methodologies for the linear thermal profile (Dhaundiyal and Toth, 2020; Ding et al., 2017). However, the effect of the higher order thermal profile on the mathematical model must be investigated especially when it correlates with the experimental data obtained at a linear thermal history. In several other studies based on the linear thermal profile, the activation energy by the random pore model for different ranks of coke is found to vary from 144.31 to 209.31 kJ·mol$^{-1}$, whereas it is in the range of 159.8–254.1 kJ·mol$^{-1}$ for DAEM (Xu et al., 2019). There is a scope of improvement in the prevailing methodology by using the higher thermal history. It is clear that the range of variation between the values obtained by the DAEM for higher thermal profile and the other methodologies (isoconversional models) is shrunken by 0.5%. Therefore, how the model reacts to a thermal profile other than the linear thermal profile is important to be known. It is reported that a constant frequency factor is not obtained when a predicted solution from the Gaussian distribution models is fitted to the proposed method by Miura (1995). However, the excellence of any methodology depends upon how well it works for the other temperature histories apart from those used for the calibration.

In this paper, the distributed activation model is analysed for a nonlinear thermal history other than the ideal thermal history. Moreover, the parametric effect on the thermal decomposition of biomass upon varying the thermal history is also perused in this study. By this investigation, it would be easy to demarcate the behaviour of biomass at varying thermal histories.

**Contact address:** Alok Dhaundiyal, Institute of Process Engineering, Szent István University, Gödöllő, Hungary, e-mail: Alok.dext@hotmail.com

## Material and methods

### Mathematical model

Anthony et al. (1976) implemented the stochastic concept of distribution of activation energy for coal pyrolysis. It later became the most reliable and suitable modelling approach for describing the biomass pyrolysis. This model is a part of the multi-reaction models, as it postulates that many decomposition reactions of $n^{th}$ order occur simultaneously. It looks similar to the lumped kinetic model, but it could be distinguished from DAEM by the number of expected decomposition reactions (Dhaundiyal and Singh, 2017). Even though the DAEM is well defined, still, some computational difficulties must be adequately addressed. Solving the double exponential term (DExp), as well as the repetitive evaluation of the double integral of DAEM, are some of the computational problems that must be dealt with. In the subsequent sections, approximations to the double exponential part of DAEM are initially developed.

$$(1-X)=\begin{cases}\int_0^{\infty}\exp\left[-\int_0^{t}A\exp\left(\frac{-E}{RT(t)}\right)dt\right]p(E)dE \,\middle|\, \text{first order } (n=1)\\ \int_0^{\infty}\left[1-(1-n)\int_0^{t}A\exp\left(\frac{-E}{RT(t)}\right)dt\right]^{\frac{1}{1-n}}p(E)dE \,\middle|\, n^{th} \text{ order } (n\neq 1)\end{cases} \quad (1)$$

where:

$E$ – activation energy, kJ·mol$^{-1}$
$t$ – time
$n$ – reaction order
$A$ – frequency factor, min$^{-1}$
$R$ – universal gas constant, kJ·mol$^{-1}$·K$^{-1}$
$X$ – conversion

In Eq. (1), the first term represents the double exponential component of DAEM, whereas $p(E)$ represents the distribution pattern of the activation energy. As the motive of this paper is to find a fast and efficient method of computing the multi reaction model, the Laplace asymptotic approximation scheme is applied to derive the numerical solution of DAEM. However, several numerical schemes have been proposed to evaluate the thermo-chemical processes. Cai and Liu (2007) adopted a simple numerical technique (Simpson's method) to estimate the kinetic parameters for the non-isothermal problem of DAEM. The time and resources get minimized if a robust, precise and a simplified asymptotic technique is adopted to solve the predefined model that is based on the parallel reactions. Therefore, the DAEM has an advantage over the other methodologies for the rapid computation of kinetics of biomass thermal decomposition. In the subsequent sections, a suitable approximation for temperature-dependent part, the double exponential term, is done. Thereafter, it is incorporated with the distribution function to examine the significance of the relative width of the double exponential term with the normal distribution.

### Double exponential (DExp) function/temperature integral

The thermal profile must be well defined before initiating the experimental procedure at the thermogravimetric analyser (TGA). Here, the non-linear temperature profile with some initial temperature (intercept), $T_0$, is assumed to vary parabolically with time. Eq. (2) defines the parabolic profile for the given initial conditions.

$$T = f(t, T) = at^2 + T_0 \quad (2)$$

where:

$a$ – coefficient of higher degree parabolic equation, °C·min$^{-2}$
$T$ – temperature
$T_0$ – initial temperature

$$DExp = \exp\left(\int_0^{t_0} A\exp\left(-E/R(a\cdot t^2+T_0)\right)dt\right) \quad (3)$$

The integral in the exponent is approximated by using the conventional Laplace scheme for asymptotic problems. It is to be noted that the term $\frac{E}{R\left(a\cdot t_0^2+T_0\right)}$ is supposed to be large, therefore, the major contribution from the integral is when '$t$' is near '$t_0$' (where temperature is near its maximum). This provides the following well-defined asymptotic expression to the function Eq. (4):

$$DExp \sim \exp\left(\frac{-RA\left(at_0^2+T_0\right)^2}{2atE}\exp\left(-\frac{E}{R\left(a\cdot t_0^2+T_0\right)}\right)\right) \quad (4)$$
$$\text{as } \frac{E}{R\left(a\cdot t_0^2+T_0\right)}\to\infty$$

The above expression can be further simplified to the form of Eq. (5) of central value $E_s$ (kJ·mol$^{-1}$) of double exponential function with the step-size width of $E_w$ (kJ·mol$^{-1}$).

$$DExp \sim \exp\left(-\exp\left(\frac{E_s-E}{E_w}\right)\right) \quad (5)$$

From the given form of the double exponential function, it is clear that the function shifts swiftly from zero to one as $E$ increase around neighbourhood of the central value $E_s$ overstep-size width of $E_w$. It can be approximated using the Taylor series and the function values at $E_s$.

Assuming that $h(E)\equiv\left(\frac{E_s-E}{E_w}\right)$, then Eq. (5) can be written as:

$$DExp \sim \exp\left(-\exp\left(h(E)\right)\right) \quad (6)$$

Comparing Eqs. (4) and (6), we have:

$$h(E)\equiv -\frac{E}{R\left(a\cdot t^2+T_0\right)}+\ln\left(\frac{RA\left(at_0^2+T_0\right)^2}{2atE}\right) \quad (7)$$

Applying the Taylor series to expression $h(E)$ and expanding it for $E_s$, we get:

$$h(E) \sim h(E_s) + (E - E_s)\, h'(E_s) + \ldots \quad (8)$$

The initial conditions for function $h(E)$ at $E_s$ are defined as:

$$h(E_s) = 0 \text{ at } h'(E_s) = -\frac{1}{E_w}$$

After solving Eqs. (7) and (8), we get:

$$E_s = R\left(at^2 + T_0\right) W\left(\frac{\left(at_0^2 + T_0\right)A}{2a \cdot t}\right)$$

$$E_w = \frac{RE_s\left(\left(at_0^2 + T_0\right)\right)}{E_s + R\left(at_0^2 + T_0\right)}$$

where:

$W(x)$ – the Lambert $W$ function is defined as one of the real roots of equation

### Distribution function of activation energy

In Eq. (1), the entire integrand includes two terms: the double exponential function, and the initial distribution $p(E)$. The initial distribution is independent of time-dependent temperature history and depends on the distribution pattern function of activation energies of volatiles substances. The initial distribution is mainly pivoted around a mean value $E_0$, and it has a standard deviation (width) $\sigma$, both are constant with respect to time. In this study, the normal distribution is adopted to evaluate the influence of the parabolic regime on the predicted results. The relatively wide initial distribution in contrast to the width ($E_w$) of the double exponential function is assumed for the proposed study. In this case, the total integrand is initially dominated by the $p(E)$. However, as time proceeds, it is truncated from the left-hand side by the step-like function – the double exponential term. The wide distribution function characteristics can be known by the location of the total integrand maximum. It gets shifted with time, and the shape of entire integrand becomes quite skewed. $T_0$ demonstrate the simplification of the distribution function, the energy and the time are rescaled by the energy ($y$) and time ($\tau$) factors.

Defining '$y$' and '$\tau$' as:

$$y = \frac{E}{E_0} \text{ and } \tau = \frac{\left(a \cdot t^2 + T_0\right)A}{2a \cdot t}$$

The distribution function is defined as:

$$p(y) = \frac{1}{\sqrt{2\pi\sigma^2}} \exp\left(-\lambda(y-1)^2\right)$$

where:

$E_0$ – the mean activation energy , kJ·mol$^{-1}$

$p(y)$ – the distribution function

$\sigma^2$ – represents the variance, kJ·mol$^{-1}$

Introducing the energy factor in Eq. (1) for the first order reaction regime, we have the following:

$$1 - X = \sqrt{\frac{\lambda}{\pi}}\left(\int_0^{\infty} \exp\left[-\exp\left(\frac{y_s - y}{y_w}\right) - \lambda(y-1)^2\right] dy\right)$$

where:

$$\lambda = \frac{E_0^2}{2\sigma^2}$$

For the parabolic ramping rate, the energy correction factors for the central and the step values are defined as:

$$y_s = \frac{R\left(a \cdot t^2 + T_0\right)W(\tau)}{E_0} \text{ and } y_w = \frac{y_s}{(1 + W(\tau))}$$

To demonstrate the approximation process for $n^{th}$ DAEM equations, Heaviside step function $H(y - y_s)$ is adopted to separate the distribution of activation energies for the two different regions:

$$H(y - y_s) = \begin{cases} 0, & y < y_s \\ 1, & y \geq y_s \end{cases}$$

$$1 - X = \sqrt{\frac{\lambda}{\pi}} \int_0^{\infty} \exp\left[\left(-\exp\left(\frac{y_s - y}{y_w}\right)\right) - H(y - y_s)\right] \exp\left(-\lambda(y-1)^2\right) dy + \sqrt{\frac{\lambda}{\pi}} \int_{y_s}^{\infty} \exp\left(-\lambda(y-1)^2\right) dy \quad (9)$$

The second term of Eq. (9) can be easily computed, as it represents the complementary error function, while the exponential term $\exp(-\lambda(y-1)^2)$ is small everywhere in the whole domain but at the vicinity of $y_s$, so it is to be expanded with the help of the Taylor series expansion in the neighbourhood of $y = y_s$.

$$1 - X = \sqrt{\frac{\lambda}{\pi}} \int_0^{\infty} \left[\exp\left(-\exp\left(\frac{y_s - y}{y_w}\right)\right) - H(y - y_s)\right] \exp\left(-\lambda(y_s - 1)^2\right)\left(1 + 2\lambda(y - y_s)(y_s - 1) + \ldots\right) dy + \frac{1}{2} erfc\left(\sqrt{\lambda}(y_s - 1)\right) \quad (10)$$

After simplifying the Eq. (10), we have:

$$1 - X \sim \frac{1}{2} erfc\left(\sqrt{\lambda}(y_s - 1)\right) + \sqrt{\frac{\lambda}{\pi}} y_w \exp\left(-\lambda(y_s - 1)^2\right) \left[L_0 - 2\lambda y_w (y_w - 1)L_1 + \lambda y_w^2 \left\{2\alpha\left(y_s - 1\right)^2 - 1\right\} L_2 + \frac{2}{3} y_w^3 \lambda^2 \left\{2(y_s - 1) + 2\alpha(y_s - 1)^3 + 1\right\} L_3\right] \quad (11)$$

The Eq. (11) is the required expression for the first order reaction. The $L_i$ is to be evaluated as it is independent of other parameters and the first few estimated values are:

$$L_0 \approx -0.5722,\ L_1 \approx -0.98906,\ L_2 \approx -1.81496,\ L_3 \approx -5.89037$$

Remaining integral is to be evaluated by:

$$L_i \equiv \int_{-\infty}^{\infty} x^i \left(\exp\left(-\exp(-x)\right) - H(x)\right)dx \; i = 0,1,2,3...$$

Similarly, the generalised estimated solution of DAEM for the different values of n is derived using the binomial expansion of given function (Eq. (1)) up to the third term:

$$1 - X_n \equiv \int_0^{\infty}\left[1-(1-n)\int_0^t 2aA\exp\left(\frac{-E}{RT(s)}\right)ds\right]^{\frac{1}{1-n}} p(E)dE \qquad (12)$$

After incorporating the energy factor and the Heaviside step function in Eq. (12), we get:

$$\sim\left[1+\sqrt{\frac{\lambda}{\pi}}\left(\int_0^{\infty}\left[\exp\left(\frac{y_s-y}{y_w}\right)-H(y-y_s)\right]\right.\right. \qquad (13)$$

$$\exp\left(-\lambda(y-1)^2\right)dy+\frac{n}{2}\int_0^{\infty}\left[\exp\left\{2\left(\frac{y_s-y}{y_w}\right)\right\}-H(y-y_s)\right]$$

$$\exp\left(-\lambda(y-1)^2\right)dy+\frac{n(2n-1)}{6}$$

$$\int_0^{\infty}\left[\exp\left\{3\left(\frac{y_s-y}{y_w}\right)\right\}-H(y-y_s)\right]$$

$$\left.\left.\exp\left(-\lambda(y-1)^2\right)dy\right)+\left(\frac{n^2+n+3}{6}\right)erfc\left(\sqrt{\lambda}(y_s-1)\right)\right]$$

The final objective function for the $n^{th}$ order reaction is expressed as follows:

$$\sim\left[1+\sqrt{\frac{\lambda}{\pi}}y_w\exp\left(-\lambda(y_s-1)^2\right)\left\{\left(M_0-2\lambda y_w(y_s-1)\right.\right.\right. \qquad (14)$$

$$M_1+\lambda y_w^2\left\{2\alpha(y_s-1)^2-1\right\}M_2+\frac{2}{3}y_w^3\lambda^2$$

$$\left.\left\{2(y_s-1)+2\alpha(y_s-1)^3+1\right\}M_3\right)+$$

$$\frac{n}{2}\left(N_0-2\lambda y_w(y_w-1)N_1+\lambda y_w^2\left\{2\alpha(y_s-1)^2-1\right\}\right.$$

$$\left.N_2+\frac{2}{3}y_w^3\lambda^2\left\{2(y_s-1)+2\alpha(y_s-1)^3+1\right\}N_3\right)+$$

$$\frac{n(2n-1)}{6}\left(O_0-2\lambda y_w(y_w-1)O_1+\lambda y_w^2\left\{2\alpha(y_s-1)^2-1\right\}\right.$$

$$O_2+\frac{2}{3}y_w^3\lambda^2\left\{2(y_s-1)+2\alpha(y_s-1)^3+1\right\}O_3\Big)+$$

$$\left.\left.\left.\left(\frac{n^2+n+3)}{6}\right)erfc\left(\sqrt{\lambda}(y_s-1)\right)\right\}\right)$$

The independent parameters $M_i$, $N_i$ and $O_i$ can be computed with the help of the integral as follows:

$$M_i \equiv \int_{-\infty}^{\infty} x_i\left(\exp(-x)-H(x)\right)dx$$

$$N_i \equiv \int_{-\infty}^{\infty} x_i\left(\exp(-2x)-H(x)\right)dx$$

$$O_i \equiv \int_{-\infty}^{\infty} x_i\left(\exp(-3x)-H(x)\right)dx$$

$i = 0, 1, 2, 3...$

## Application and the computational scheme

The samples of pine needles were collected from Tehri Garhwal, Uttarakhand, India. The pine needles were kept under the influence of direct sunlight to expel the moisture so that it could undergo the series of experiments. The sample calorific value and chemical composition were assessed with the help of the bomb calorimeter and CHNO-S, respectively, whereas the thermal analysis was carried out with the help of the thermogravimetric analyser (horizontal) (TG/DTA) (Perkin Elmer Diamond TG/DTA, USA). The sample of weight 5.68 mg was heated in a crucible pan of alumina at a temperature range of 303–923 K. To prevent the buoyancy effect at the elevated temperature, the horizontal differential type of prototype analyser was selected. The thermocouple type '*R*' was used for measuring the temperature inside the furnace. The volumetric purge rate of nitrogen 200 mL·min$^{-1}$ was allowed to ensure that there is no oxygen left in the chamber. Indium and tin were used as reference materials for the differential thermal analysis of pine needles. Table 1 illustrates the elemental composition and higher heating values of the pine needles on dry basis.

For the computation and simulation purposes, MATLAB R2017b software was used. It is to be noted that the thermo-analytical data were used to predict the results for non-linear $n^{th}$ order DAEM. The given problem was solved for the different physical regimes. Thereafter, the computational script was programmed for multiple iterations. The objective functions of the given computation problem are represented by Eqs. (11) and (14). Each assigned value was selected after comparing it with the permissible limit of the root mean square error while running every iterative cycle. Unless the estimated value agreed with the end conditions, the iterative loop kept looking for the new possible value. Subsequently, the kinetic parameters were evaluated on the basis of the constraints imposed to the given problem. Since the calculation of the root mean square error and the coefficient of regression pivoted around the grey box modelling concept, the comparative analysis of non-linear thermal profile with linear ramping temperature history was inevitable. Table 2 shows the relative solution deviation at different heating profiles for similar distribution pattern.

**Table 1** Elemental composition of pine needles

| C% | H% | N% | O% | S% | Ash content (%) | Higher heating value (MJ·kg$^{-1}$) |
|---|---|---|---|---|---|---|
| 53.7 | 5.21 | 0.61 | 32.13 | 0.22 | 4.72 | 19.5 |

**Table 2** Comparative illustration of different non-isothermal profile

| Distribution type | Ramping profile (non-isothermal) | Root mean square error (RMSE) | $R^2$ (coefficient of regression) |
|---|---|---|---|
| **Normal distribution** | linear | 0.070 | 0.90 |
| | parabolic | 0.010 | 0.95 |

## Results and discussion

The qualitative and quantitative analysis of the non-linear, non-isothermal pyrolysis of biomass is carried out with the help of the Laplace approximations. The influence of the parabolic regime and the parametric values of frequency factors on the numerical solution is illustrated in Fig. 1. At the initial pyrolysis stage, the unreleased mass fraction $(1 - X)$ of the biomass must be in the vicinity of one. On the other hand, Fig. 1 indicates that the mass is less than one for all the frequency factor values. The increasing frequency factor trend causes an upward shift at the tail end of $(1 - X)$, albeit the prediction of the variation in the residual mass at the end of the pyrolysis is negligibly smaller than that of the linear ramping profile. The root mean square error at the end of the extremities of curves is drastically reduced with an increase in the degree of an equation of time (Dhaundiyal and Singh, 2017). For the value of $A$ (min$^{-1}$), 400 $\leq A \leq$2000, the curves show a good agreement with the experimental condition at the end of the pyrolysis.

The initial temperature effect $T_0$ (K) on the biomass pyrolysis numerical solution is depicted in Fig. 2. The initial sample temperature influence on the remaining mass fraction curves is demarcated by the change in the order of the reactions. For the first-order reactions (Fig. 2a), the decrease in the initial sample temperature causes the inflexion point to move to the right side. The rate of decomposition becomes faster for the same value of $\Delta T$ at the pyrolysis end. However, biomass dehydration varied rapidly with increasing initial temperature, and consequently, the remaining mass proportion gets reduced at the same temperature interval. On the contrary, the unreleased biomass sample mass fraction decreases continuously until the initial sample temperature reaches 329.57 K. After reaching the threshold of 329.57 K, the remaining mass fraction gets shifted towards the left side. It can be concluded from observation that the range of the initial temperature (300–330 K) provides a good solution for the given experimental conditions.

The effect of '$a$' and the experimental coefficient of nonlinear temperature history is shown in Fig. 3. The anomaly in the unreleased mass fraction curves is shown at the interval extremities of the total integrand function. The change in the value of activation energies increases with respect to $E_s$. It can be perceived that, at a higher value of '$a$',

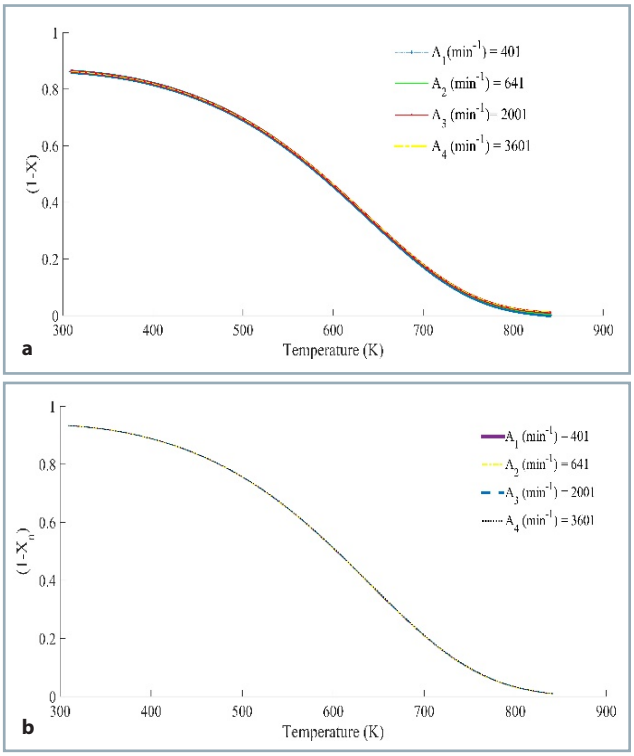


**Fig. 1** Effect of frequency factor ($A$) on the numerical solution of the $n^{th}$ order DAEM
a – the first order reaction; b – the $n^{th}$ order reaction ($a$ = 0.0175 °C·min$^{-2}$, σ$^2$ = 9.47 kJ·mol$^{-1}$, $n^{th}$ order = 0.7 and $T_0$ = 289.57 K)

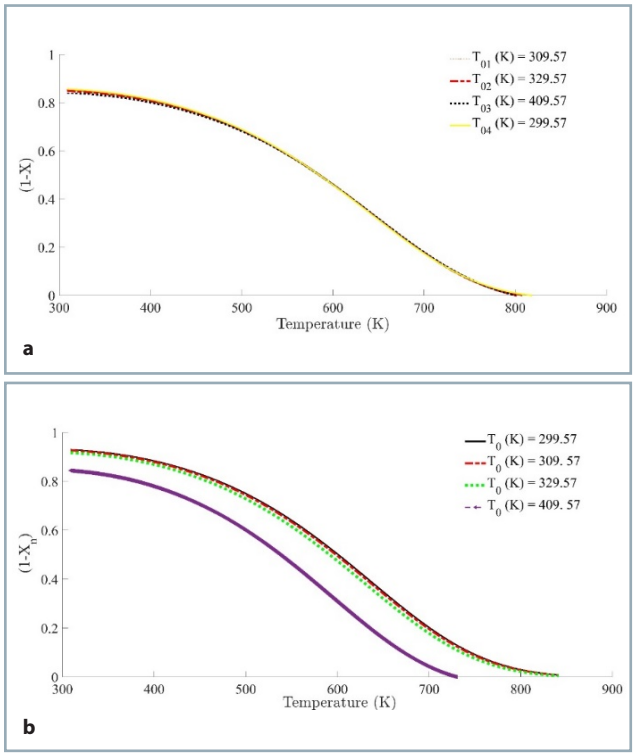


**Fig. 2** Influence of initial value condition '$T_0$' (K) on the numerical solution of nth order DAEM
a – the first order reaction, b – the $n^{th}$ order reaction ($a$ = 0.0175 °C·min$^{-2}$, σ$^2$ = 9.47 kJ·mol$^{-1}$, $n^{th}$ order = 0.7 and $A$ = 400 min$^{-1}$)

it should lie in the domain of $a \in [0.013, 0.027)$. Furthermore, the effect of '*a*' on the reactions with the order, less than one, does not provide an appreciable change in the total integrand variance.

However, the temperature shifting scales up at the tail end of the curves. With the increase in the value of '*a*', the slope of (1 – *X*) curve increases. Therefore, the same conversion is obtained at an elevated temperature. The reason for exhibiting the deviation is the heat transfer limitation between sample and furnace due to the insufficient time interval to overcome the relatively high thermal gradient.

The activation energy effect (Fig. 4) on the numerical solution is not as distinct as it is for the linear ramping temperature history (Dhaundiyal and Tewari, 2017). In case of the reaction order ($n$ <1), as the activation energy increases, the change rate of the remaining mass fraction is relatively accelerated in the region of the char formation for the same temperature interval. For the values of the activation energy 211 kJ·mol$^{-1}$ ≤ $E$, the results are much promising and show a close proximate to each other; hence 810 kJ·mol$^{-1}$ is used as the upper limit of the $dE$ kJ·mol$^{-1}$ integral. A similar set of solutions has been determined by using the bi-variant form of the distribution function, where the sets of reactions are separately defined as the series of event, but the thermal history used for the analysis purposes was linear (Dhaundiyal et al., 2018). The possible reasons for the high activation energy value can be either related to the acceleration in the secondary char formation (which is chemically quite stable), or the variation in the reaction

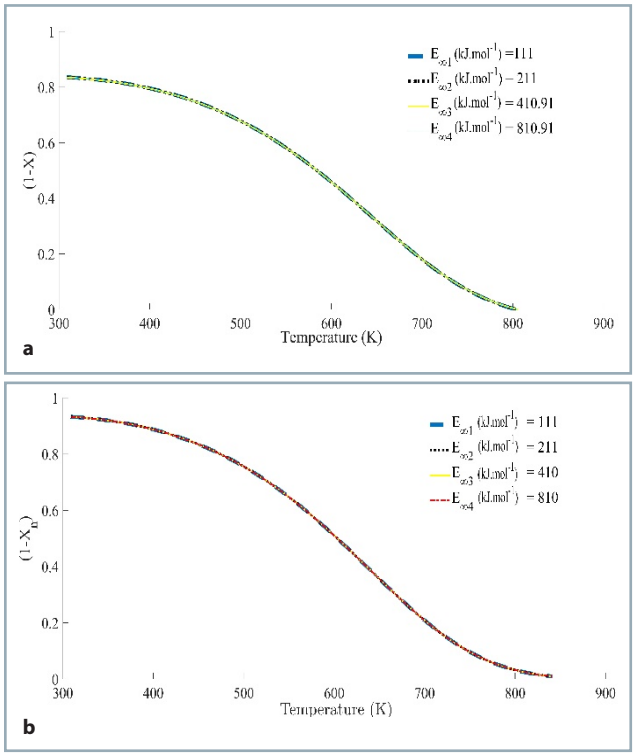


**Fig. 4** Effect of the upper limit ($E_\infty$) (kJ·mol$^{-1}$) on the numerical solution of $n^{th}$ order DAEM
a – the first order reaction, b – the $n^{th}$ order reaction ($T_0$ = 289.57 K, $n^{th}$ order = 0.7, $a$ = 0.0175 °C·min$^{-2}$, $\sigma^2$ = 9.47 kJ·mol$^{-1}$ and $A$ = 400 min$^{-1}$)

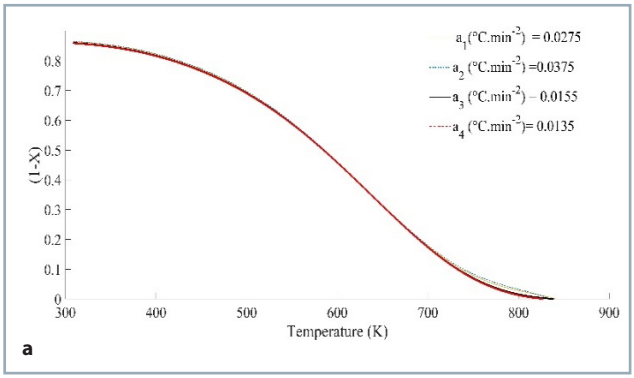


**Fig. 3** Effect of experimental coefficient '*a*' (°C·min$^{-2}$) on the numerical solution of nth order DAEM
a – the first order reaction, b – the $n^{th}$ order reaction ($T_0$ = 289.57 K, $\sigma^2$ = 9.47 kJ·mol$^{-1}$, $n^{th}$ order = 0.7 and $A$ = 400 min$^{-1}$)

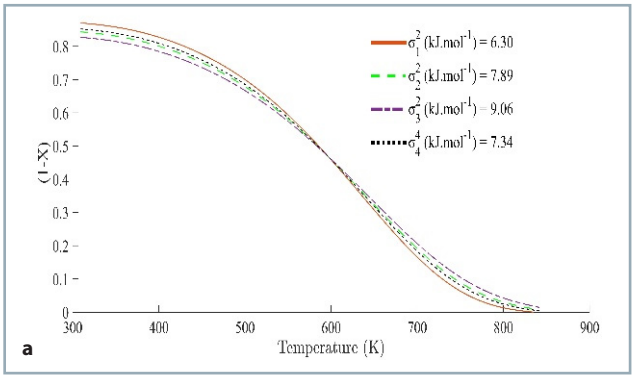


**Fig. 5** Effect of variance $\sigma^2$ (kJ·mol$^{-1}$) of the Gaussian distribution on the numerical solution of $n^{th}$ order DAEM
a – the first order reaction, b – the $n^{th}$ order reaction ($T_0$ = 289.57 K, $n^{th}$ order = 0.7, $a$ = 0.0175 °C·min$^{-2}$ and $A$ = 400 min$^{-1}$)

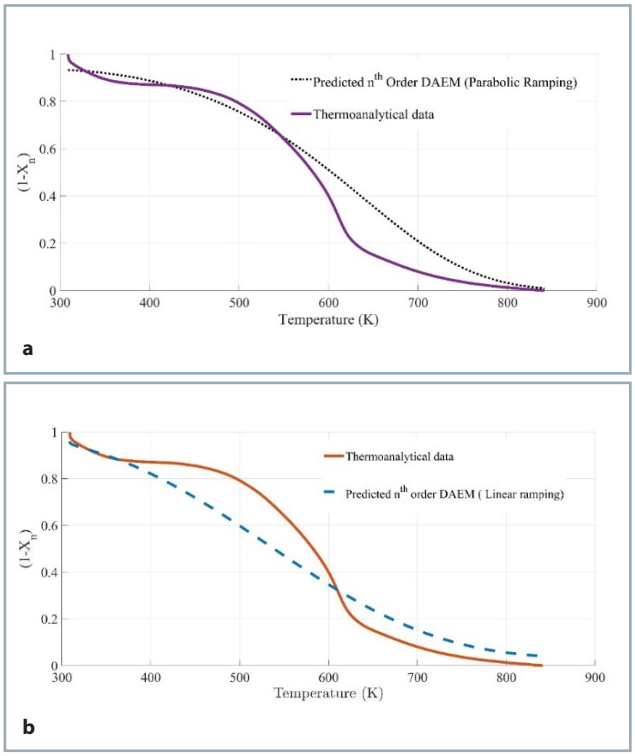


**Fig. 6** Comparative illustration of predicted $n^{th}$ order DAEM with thermo-analytical results
a – parabolic, b – linear

heat. Tinney (1965) reported that the structural breakdown might change the apparent kinetics of the reaction, which eventually increases the activation energy, as well as the heat of reaction. These changes occurred when the ratio of the bulk density $\rho_b$ (kJ·m$^{-3}$) at time $t$ to $\rho_b$ (kJ·m$^{-3}$) of wood at $t$ =0 varies from 0.5 to 0.33 while heating the wooden dowel. Therefore, it might be possible that the extent of the primary and secondary pyrolysis reactions would be influenced by selected thermal history.

The variance effect on the numerical results is illustrated in Fig. 5. It can be observed that the change in the normal distribution variance causes the slope of the remaining mass proportion curves to vary rapidly with temperature. The variance values $\sigma^2 \leq 6.30$ kJ·mol$^{-1}$ provide a good fitting with the thermo-analytical data, therefore, it can be used for the biomass pyrolysis modelling. However, the relative variance effects on the objective functions get subdued as the reaction order decreases (Fig. 5b). The curve range shrinking is due to the relative difference of $n(n + 1)/3$, therefore, the results obtained through the lower reaction order are closely approximated, and the variation about the mean value ys does not affect the overall attribute of $(1 - X)$.

The comparative experimental data illustration with predicted parabolic and linear temperature regimes is performed in Fig. 6. From Table 2, it is quite clear that the non-linear temperature ramping provides a better fitting than linear ramping. The linear ramping describes the biomass pyrolysis at its beginning and end. However, it has failed to provide sufficient information about the devolatilization region of the thermal decomposition. On the other hand, the parabolic regime is able to predict the drying, the limited devolatilization, and the char formation stage of the thermo-analytical curve. The numerical solution does not converge at the devolatilization end and the char formation beginning. But it can be solved by introducing the higher order regime of the temperature with time.

### Conclusion

For the numerical solution of the non-linear ramping temperature history, 810 kJ·mol$^{-1}$ is incorporated as the upper limit of the activation energies. The frequency factor ($A$) should lie in the range of $400 \leq A$ (min$^{-1}$) <2000, whereas the initial temperature must be $T_0$ (K) ≤300. For the given problem of the pine needles, the values of '$a$' (varying from 0.0275 to 0.0135 °C·min$^{-2}$) and distribution parameter '$\sigma^2$' (ranging from 6.30 to 7.34 kJ·mol$^{-1}$) are related to the experimental conditions and distribution pattern. Therefore, they merely affect the attributes of the remaining mass proportion. In case of the normal distribution of activation energies, the variance should not be more than 0.630 kJ·mol$^{-1}$ for the parabolic regime of temperature. The reaction order for the non-linear temperature profile lies in the domain of $0.1 \leq n <1$. The derived results are helpful to evaluate the influence of the higher degree equation along with the relevant parameters required for the modelling of the biomass pyrolysis. It can be concluded that the parabolic profile delineates the biomass pyrolysis process better than the linear ramping for the same parametric values.

## Results and discussion

ANTHONY, D. B. – HOWARD, J. B. – MEISSNER, H. P. 1976. Coal devolatilization and hydrogastification. In AIChE Journal, vol. 22, no. 4, 625–656.

CAI, J. M. – LIU, R. H. 2007. Parametric study of the nonisothermal $n^{th}$-order distributed activation energy model involved the Weibull distribution for biomass pyrolysis. In Journal of Thermal Analysis and Calorimetry, vol. 89, no. 3, pp. 971–975.

DHAUNDIYAL, A. – GUPTA, V. K. 2014. The analysis of pine needles as a substrate for gasification. In Hydro Nepal: Journal of Water, Energy, and Environment, vol. 15, 73–81.

DHAUNDIYAL, A. – SINGH, S. B. – HANON, M. M. 2018. Study of distributed activation energy model using bivariate distribution function, $f$ (E1, E2). In Thermal Science and Engineering Progress, vol. 5, pp. 388–404.

DHAUNDIYAL, A. – SINGH, S. B. 2017. Parametric study of $n^{th}$ order distributed activation energy model for isothermal pyrolysis of forest waste using Gaussian distribution. In Acta Technologica Agriculturae, vol. 20, no. 1, pp. 23–28.

DHAUNDIYAL, A. – TEWARI, P. 2017. Kinetic parameters for the thermal decomposition of forest waste using distributed activation energy model (DAEM). In Environmental and Climate Technologies, vol. 19, pp. 15–32.

DHAUNDIYAL, A. – TEWARI, P. C. 2015. Comparative analysis of pine needles and coal for electricity generation using carbon taxation and emission reductions. In Acta Technologica Agriculturae, vol. 18, no. 2, pp. 29–35.

DHAUNDIYAL, A. – TOTH, L. 2020. Modeling of hardwood pyrolysis using the convex combination of the mass conversion points. In Journal of Energy Resources Technology, Transactions of the ASME, vol. 142, no. 6, pp. 1–10.

DHAUNDIYAL, A. – TOTH, L. – BACSKAI, I. – ATSU, D. 2020.Analysis of pyrolysis reactor for hardwood (*Acacia*) chips. In Renewable Energy, vol. 147, pp. 1979–1989.

DI BLASI, C. 2008. Modeling chemical and physical processes of wood and biomass pyrolysis. In Progress in Energy and Combustion Science, vol. 34, pp. 47–90.

DING, Y. – EZEKOYE, O. A. – LU, S. – WANG, C. – ZHOU, R. 2017. Comparative pyrolysis behaviors and reaction mechanisms of hardwood and softwood. In Energy Conversion and Management, vol. 132, pp. 102–109.

MIURA, K. 1995. A new and simple method to estimate f(E) and ko(E) in the distributed activation energy model from three sets of experimental data. In Energy and Fuels, vol. 9, pp. 302–307.

LEE, Y. L. – AHMED, O. H. – WAHID, S. A. – AB AZIZ, Z. F. 2019. Characterization of tablets made from mixture of charred agricultural residues with and without embedded fertilizer. In Acta Technologica Agriculturae, vol. 22, no. 3, pp. 70–74.

TINNEY, E. R. 1965. The combustion of wooden dowels in heated air. In Tenth Symposium (International) on Combustion. Combustion Institute, pp. 925–930.

WHITE, J. E. – CATALLO, W. J. – LEGENDRE, B. L. 2011. Biomass pyrolysis kinetics: A comparative critical review with relevant agricultural residue case studies. In Journal of Analytical and Applied Pyrolysis, vol. 91, pp. 1–33.

XU, J. –ZUO, H. – WANG, G. – ZHANG, K. – GUO, K. – LIANG, W. 2019. Gasification mechanism and kinetics analysis of coke using distributed activation energy model (DAEM). In Applied Thermal Engineering, vol. 152, pp. 605–614.

DOI: 10.2478/ata-2021-0006



Acta Technologica Agriculturae 1
Nitra, Slovaca Universitas Agriculturae Nitriae, 2021, pp. 35–40

# DESIGN OF LABORATORY TEST EQUIPMENT FOR TESTING THE HYDROSTATIC TRANSDUCERS

Jozef NOSIAN[1]*, Ľubomír HUJO[1], Marcin ZASTEMPOWSKI[2], Romana JANOUŠKOVÁ[1]

[1]Slovak University of Agriculture in Nitra, Slovakia
[2]UTP University of Science and Technology, Bydgoszcz, Poland

The article presented describes a new design of measuring chains in laboratory test equipment, which are used for testing the hydrostatic transducers and hydraulic fluids. Laboratory test equipment allows simultaneous observation of parameters of hydrostatic transducers and hydraulic fluids by simulating the operating conditions under laboratory conditions, what can significantly reduce the testing time and economic costs. The new design functionality was verified via measurement of the basic parameters of hydrostatic transducers and changing the load of hydraulic fluids. Based on the results measured, the flow efficiency of tested hydrostatic transducer UD-25R was calculated and compared with the transducer parameters specified by the manufacturer using different types of operating hydraulic fluids. Verification measurements of the unloaded hydrostatic transducer were performed at various rotation speeds: $Q_{250}$ = 5.694 dm$^3$·rpm at speed of $n_1$ = 250 rpm; $Q_{500}$ = 12.286 dm$^3$·rpm at speed of $n_2$ = 500 rpm; $Q_{750}$ = 18.747 dm$^3$·rpm at speed of $n_3$ = 750 rpm. Based on the hydrostatic transducer flow rate, the UD-25R transducer flow efficiency was determined: at $n_1$ = 250 rpm, the flow efficiency was $\eta_{250}$ = 0.8946; at $n_2$ = 500 rpm, the efficiency was $\eta_{500}$ = 0.9651; at $n_3$ = 750 rpm, the flow efficiency was $\eta_{750}$ = 0.9812.

**Keywords:** hydraulic pump; hydraulic circuits; measuring chain; verification measurement; hydraulic equipment

Hydraulic systems and equipment have become an important part of almost all types of machines in order to increase the efficiency and energy transfer. Due to their wide use, increasing demands are put on hydraulic systems – this applies to both hydrostatic transducers and hydraulic fluids used in hydraulic systems. Kučera et al. (2016) reported that it is possible to determine the technical condition of hydraulic elements in hydraulic systems based on the operating fluid analysis. There are high requirements for hydraulic fluids that serve as energy carriers in hydraulic systems. Producers must take into account the demands for their quality improvement and environmental burden reduction (Kosiba et al., 2016a). A comprehensive analysis of the effects of biological fluids and mixtures has already been performed by Puškár et al. (2019). Čorňák (2018) has also dealt with this topic. Recently, the operation and development of hydraulic systems has focused on ecological operation, which uses hydraulic systems to mitigate the environmental pollution. For this reason, ecological fluid carriers are increasingly used in hydraulic circuits. The need for testing the agricultural machinery in terms of its suitability for agricultural use will continuously grow, because the machinery has direct impacts on agricultural production (Tkáč et al., 2017). The device proposed can be also used for tribodiagnostics of oil or individual hydraulic elements in hydraulic circuit. Tribodiagnostics utilizes the oils as media for obtaining the information on processes and changes in the systems, in which they occur (Halenár and Kuchar, 2017). The investigation of hydraulic devices used in industry was also dealt by Simikič et al. (2014) and Markiewicz-Patalon et al. (2018). The proposed device was used to test the parameters of hydrostatic converters. According to Kosiba et al. (2019), the design of the proposed device must meet certain requirements under measurement conditions, i.e., the oil temperature and speed of the hydrostatic transducers are especially important.

## Material and methods

According to Tkáč et al. (2010), when determining the correct function of the hydrostatic transducer, it is important to monitor the flow rate, which can be used for calculation of the flow efficiency. The measuring chain measures the parameters of hydrostatic transducers. The proposed laboratory test equipment allows more options for connecting the measuring chain consisting of two hydraulic circuits – there is one primary and one secondary measuring chain, enabling continuous and simultaneous test of two pumps or two types of hydraulic under the same conditions.

In accordance with the SAE J745 standard, prior to verification measurement, the working fluid PARAMO HM 46 was heated to a working temperature of 50 °C in the secondary hydraulic circuit of measuring chain. Subsequently, the required rotation was set, at which the verification was to be performed. The pump was measured at following rotations:

– $n_1$ = 250 rpm,

**Contact address:** Jozef Nosian, Slovak University of Agriculture in Nitra, Department of Transport and Handling, 949 76 Nitra, Slovakia, e-mail: jozef.nosian@uniag.sk

– $n_2$ = 500 rpm,
– $n_3$ = 750 rpm.

At each of these rotations, the measurements were performed; based on the measured values, three critical values were determined and then compared and evaluated afterwards.

The minimum necessary number of repetitions was determined as follows:

$$n = t_a^2 \frac{s}{\Delta^2} \quad (1)$$

where:
$n$ – the number of repetitions
$t_a$ – critical value of the normal distribution for a bilateral estimate
$\Delta$ – selected value of the required accuracy
$s$ – estimated standard deviation of the base set

Table 1 shows the results of mathematical and statistical analysis necessary to determine the minimum required number of repetitions when measuring the flow of the hydrostatic transducer.

The determination of the individual hydraulic device components for assessing the operation of hydraulic pumps and energy carriers is as follows (Tkáč et al., 2017):

Hydrostatic transducer flow:

$$Q = \frac{V_g \cdot n}{1000} \cdot \eta_{fl}, \quad \mathrm{dm^3 \cdot rpm} \quad (2)$$

where:
$V_g$ – hydrostatic transducer volume, $dm^3$
$n$ – hydrostatic transducer rotation speed rotation, rpm
$\eta_{fl}$ – hydrostatic transducer flow efficiency

Hydrostatic transducer power:

$$P = \frac{V_g \cdot n \cdot p}{60 \cdot 1000 \cdot \eta_c}, \quad \mathrm{W} \quad (3)$$

where:
$p$ – pressure, MPa
$\eta_c$ – overall effectiveness Inner diameter of the pipe:

$$d = \sqrt{\frac{4 \cdot Q}{\pi \cdot w}}, \quad \mathrm{mm} \quad (4)$$

where:
$w$ – resistance to flow rate, $m \cdot s^{-1}$

Cooling power:

$$P_0 = P_{01} \cdot 1.1, \quad \mathrm{W \cdot °C^{-1}} \quad (5)$$

Specific cooling power:

$$P_{01} = \frac{P_v}{T_1 - T_2}, \quad \mathrm{W \cdot °C^{-1}} \quad (6)$$

where:
$P_v$ – cooling power, W
$T_1$ – maximum temperature, °C
$T_2$ – minimum temperature, °C

Measurement of physical quantities in the hydraulic system under operating conditions was performed using associated sensors (HYDAC International EVS 3 100). Following quantities are the most frequently measured qualities in hydraulic circuits: pressure, temperature, and

**Table 1** Results of mathematical and statistical analysis for determination of the minimum required number of repetitions when measuring the hydrostatic transducer flow

| **Input parameters** | |
|---|---|
| **Required accuracy $\Delta$ ($dm^3 \cdot rpm$)** | 0.9 |
| **Maximum permissible error $\delta$ (%)** | 4.0 |
| **Critical value of normal distribution, $t_\alpha$ – 90%** | 1.645 |
| **Critical value of normal distribution, $t_\beta$ – 90%** | 1.282 |

| **The resulting calculated parameters of the minimum number of repetitions** | | | |
|---|---|---|---|
| | **rotation speed of hydrostatic transducer nH (rpm)** | | |
| | **250** | **500** | **750** |
| **For the value of the normal distribution $t_\alpha$** | 2 | 2 | 2 |
| **For the value of the normal distribution $t_\beta$** | 1 | 1 | 1 |
| **For $\delta \cdot v_k^{-1}$** | 1 | 1 | 1 |

**Table 2** Technical data of the HYDAC EVS 3 100 sensor

| **Input data** | |
|---|---|
| **Measuring ranges ($dm^3 \cdot rpm$)** | **Operating pressure (MPa)** |
| **1.2–20** | 40 |
| **6.0–60** | 40 |
| **15.0–300** | 40 |
| **40.0–600** | 31.5 |
| **Input data** | |
| **Output signal, allowable load resistance** | 4–20 mA, $R_{L\ max} = (U_B$ - 10 V/20 mA, kΩ) |
| **Accuracy** | ≤2% real value |
| **Additional data** | |
| **Compensated temperature range** | from -20 to +70 °C |
| **Operating temperature range** | from -20 to -70 °C |
| **Fluid temperature range** | from -20 to -90 °C |
| **Protection class** | IP 65 |
| **Supply voltage** | 10–32 V |
| **Residual ripple of the supply voltage** | ≤5% |
| **Viscosity range** | 1–100 $mm^2 \cdot s^{-1}$ |
| **Calibration viscosity** | 30 $mm^2 \cdot s^{-1}$ |

**Table 3** Technical parameters of hydraulic pump UD-25R

| Parameter | Unit | Value |
|---|---|---|
| **Rated rotation** | rpm | 1500 |
| **Maximum rotation** | | 3200 |
| **Minimum rotation** | | 450 |
| **Maximal pressure at the inlet** | MPa | 0.05 |
| **Minimum inlet pressure** | | 0.03 |
| **Nominal outlet pressure** | MPa | 20 |
| **Maximum outlet pressure** | | 23 |
| **Geometric volume** | $dm^3$ | 0.02546 |
| **Maximum oil viscosity** | $mm^2 \cdot s^{-1}$ | 1t200 |
| **Minimum oil viscosity** | | 10 |
| **Maximum oil temperature** | °C | 80 |
| **Minimum oil temperature** | | -20 |

**Table 4** Characteristics of PARAMO HM 46 oil

| Parameter | Unit | PARAMO HM 46 |
|---|---|---|
| **Point of fluidity** | °C | -27 |
| **Flash point** | °C | over 190 |
| **Inflammability** | – | fourth hazard class |
| **Vapour pressure at 20 °C** | Pa | <10 |
| **Relative density at 15 °C** | $kg \cdot m^{-3}$ | 865 |
| **Solubility** | – | insoluble in water |
| **Auto-ignition temperature** | °C | over 320 |
| **Kinematic viscosity at 40 °C** | $mm^2 \cdot s^{-1}$ | 41.4–50.6 |
| **Explosive properties** | – | it is not explosive |
| **Oxidizing properties** | – | it is not oxidizing |

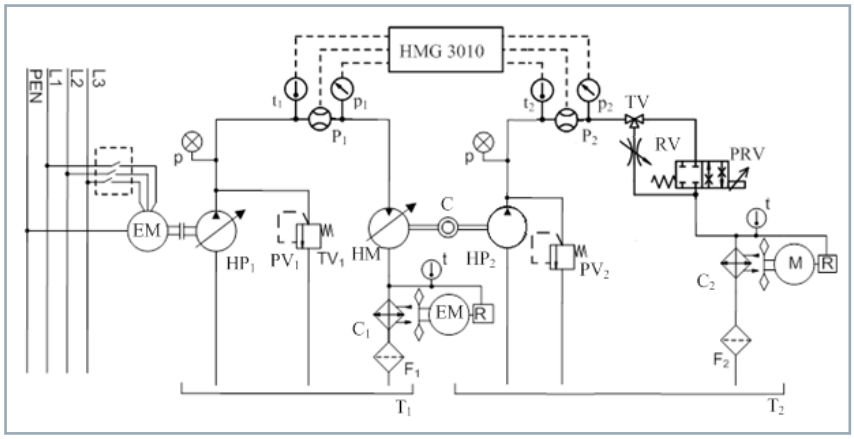


**Fig. 1** Laboratory equipment for measuring the parameters of hydrostatic transducers

EM – electromotor; $HP_1$ – regulatory hydraulic pump; $PV_1$, $PV_2$ – pressure valve; HM – regulatory hydraulic motor; $HP_2$ – tested hydraulic pump; $C_1$, $C_2$ – cooler; t – temperature sensor for tanks; p – pressure gauge; RV – reducing valve; TV – three-way valve; PRV – proportional reducing valve; C – coupler; R – regulator of electric motor; $t_1$, $t_2$ – ETS 4148-H-006-000 temperature sensors; $P_1$, $P_2$ – EVS 3108-H-0300-000 flow rate sensors; p1, p2 – HDA 4748-H-0400-000 pressure sensors; HMG 3010 – recording unit

flow, since they are the main indicators of technical condition of hydraulic circuit elements. Associated sensors were used for measuring the physical quantities and recorded values were transmitted to the HYDAC HMG 3010 recording unit. These sensors were in the primary and secondary hydraulic circuit and their technical are given in Table 2.

HYDAC HMG 3010 measuring device was used to record and display the measured values. The device contains: advanced voltage measurement in ranges from -10 to +10 V and from 0 to 50 V. It offers the possibility of recording signals on two inputs in 0–50 V range, and on one input from -10 to +10 V range. The device protection class is IP 40. The device maximum inaccuracy is ±1%.

The aforementioned relations determine the basic element parameters of laboratory test equipment hydraulic circuit. Other elements of the measuring chain were dimensioned based on the technical data in the product catalogue of hydraulic elements. Table 3 shows the technical parameters of the UD-25R hydrostatic transducer specified by the manufacturer.

PARAMO HM 46 hydraulic fluid was used as the hydraulic charge in the secondary hydraulic circuit. It is mainly intended for hydrostatic hydraulic mechanisms. Its properties are listed in Table 4.

## Results and discussion

Fig. 1 shows a schematic circuit of newly designed laboratory test equipment for measuring and testing the hydrostatic transducers and working fluids used in hydraulic equipment. The proposed device consists of two hydraulic circuits: the primary circuit is connected to the electric motor (EM), and the secondary circuit is connected to the hydraulic pump (HP2).

Fig. 2 shows the equipment for measuring the parameters of hydrostatic transducers and hydraulic fluids, which was used for performing the life tests of hydrostatic transducers in parallel using two different working fluids. According to Kosiba et al. (2016b), it is important to monitor the parameters of hydrostatic transducers under operating conditions.

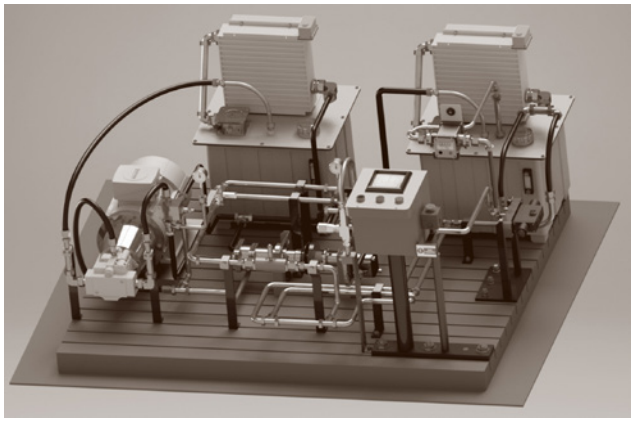

**Fig. 2** Test equipment for measuring the parameters of hydrostatic transducers

The measuring chain is used to measure the parameters of hydrostatic transducers and allows several possibilities of its connection. The proposed design allows to test two hydrostatic transducers or two types of hydraulic fluids in parallel, either under the same conditions, or to simulate the operating load. An asynchronous electric motor connected to a hydrostatic transducer via a mechanical coupling was used to drive the pump in the primary circuit. The circuit includes a pressure valve, which is in both the primary and secondary circuits, and performs the function of a safety valve and prevents the occurrence of a hazardous condition. A cooler for temperature regulation of working fluids is included in both the primary and secondary circuits. This also applies to a filter and a tank with the same volume in each circuit. A hydro-engine for conversion of pressure energy to mechanical energy is included in the primary circuit and connected to a hydrostatic transducer in the secondary circuit via a mechanical coupling. Considering the secondary circuit, a three-way valve for fluid flow control and a throttle valve for deriving the load in hydraulic circuit are included. Furthermore, there is also a proportional valve for deriving the load and simulating the operating pressures. Sensors for recording rotation, temperature, flow and pressure were added to the hydraulic circuit. These sensors are connected to the HYDAC HMG 3010 recording unit, through which the parameters during the verification measurement were recorded.

Experimental measurements of hydrostatic transducers under laboratory conditions are of great importance, especially in relation to the testing of basic parameters. In these measurements, it is possible to simulate various states and test the transducers before they are put into practice, and the same applies to hydraulic fluids. This means that the manufacturers of hydrostatic transducers and hydraulic fluids can modify their products based on the measurement results. Concurrently, experimental measurements can also be used to create dynamic flow models of hydrostatic transducers in order to compare individual parameters.

Verification of the measuring chain for measuring and testing of hydrostatic transducers was conducted in order verify whether the pump, hydraulic circuit elements and designed measuring chains operate appropriately. Prior to verification measurement itself, it was necessary to calibrate the sensors and, during the verification measurement, the flow of the UD-25R pump in the secondary hydraulic circuit of the measuring chain was observed.

Flow and flow efficiency values were used to create dynamic flow models in hydrostatic transducers using numerical simulation to protect the environment (Puškár et al., 2015). When verifying the measurement of a given measuring chain, the first step is to heat the working fluid to an operating temperature of 50 °C. Based on the settings of the HYDAC HMG 3010, the hydrostatic transducer flow was measured for 1 minute, with 0.100 ms sampling, and recorded 600 samples of hydrostatic transducer flow data. For a given measurement of the measuring chain, the hydraulic circuit was observed without load. At each rotation speed, measurements were performed and three critical values were determined for comparison and evaluation.

Flow efficiency of hydrostatic transducer in verification measurement UD-25 R (sample calculation) is as follows:

$$\eta = \frac{Q}{V_G \cdot n} 100 = \frac{5.694}{0.02546 \cdot 250} \cdot 100 = 89.46\% \qquad (7)$$

The measured data with basic statistics are shown in Table 6.

**Table 5** Verification of average flow value obtained in verification measurement with a constant given by the hydrostatic transducer manufacturer

| Input parameters | | |
|---|---|---|
| **Parameter** | **Marking** | **Value** |
| **Significance level** | $\alpha$ | 0.050 |
| **Set of values** | n | 50 |
| **Critical value** | $\mu_0$ | 1.960 |
| **Calculated values of the test criterion m** | | |
| **Rotation speed of hydrostatic transducers nH, rpm** | | |
| **250** | **500** | **750** |
| **18.80** | **51.92** | **73.70** |

Legend: cells indicating the increased flow rates in contrast to values specified by the manufacturer; cells indicating the reduced flow rates in contrast to values specified by the manufacturer

**Table 6** Measured data with basic statistics

| Rotation speed | 250 rpm | 500 rpm | 750 rpm |
|---|---|---|---|
| **Arithmetic mean** | 5.694 | 12.286 | 18.747 |
| **Maximum value** | 5.930 | 12.390 | 18.850 |
| **Minimum value** | 5.330 | 12.130 | 18.590 |
| **Medium value** | 5.760 | 12.300 | 18.760 |
| **Number of measurements** | 50 | 50 | 50 |
| **Modus** | 5.850 | 12.300 | 18.760 |
| **Median** | 5.760 | 12.300 | 18.760 |
| **Standard deviation** | 0.176 | 0.061 | 0.0550 |
| **Coefficient of variation (%)** | 3.100 | 0.499 | 0.294 |

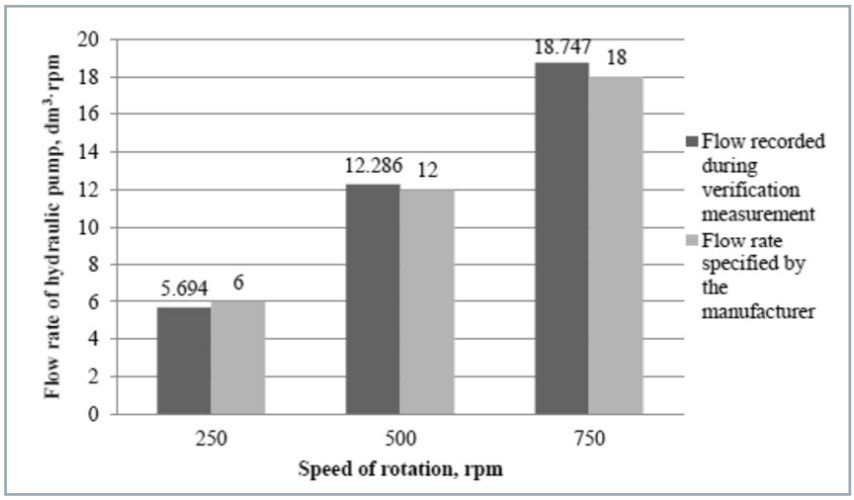


**Fig. 3** Hydraulic pump flow values recorded during the verification measurement and flow values specified by the manufacturer

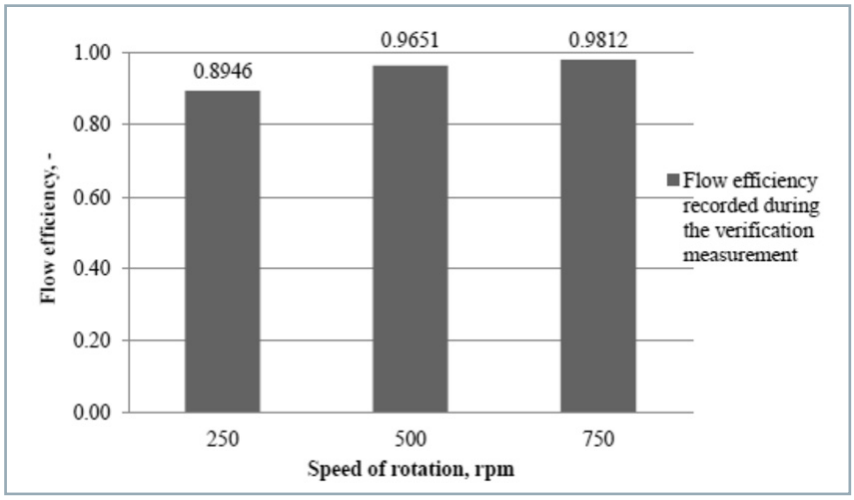


**Fig. 4** Flow efficiency values of the UD-25 R hydraulic pump calculated from the values obtained during the verification measurement

During data evaluation from verification measurement, there was observed a decrease in flow of hydrostatic transducer by 5.1% at $n_1$ = 250 rpm compared to the data given by manufacturer. At rotation speeds $n_2$ = 500 rpm and $n_3$ = 750 rpm, there was an increase in flow by 2.38% and 4.15%, respectively, compared to the data provided by manufacturer.

Fig. 3 shows the hydrostatic transducer flow data observed during the verification measurement and the flow data provided by manufacturer. The differences in values can be explained by different measurement conditions: the manufacturer assumes a temperature of 45 °C, while the verification measurement was performed at an operating temperature of 50 °C. According to Tulík et al. (2015), temperature has a fundamental effect on the hydraulic fluid properties during the measurement, which may lead to different resulting values recorded during the measurement. Halenár and Kuchar (2017) observed the hydrostatic transducer flow of 7.64 dm$^3$·rpm at 500 rpm, and 11.75 dm$^3$·rpm at 750 rpm. The difference results from the fact that Halenár and Kuchar (2017) used a hydraulic pump QHD-17R, which cyclically loaded the circuit with pressure.

Fig. 4 shows the UD-25 R pump flow efficiencies during verification measurement. The pump manufacturer does not state the pump efficiency at the rotation that was set during the verification measurement, to which the speed was intentionally set in the first third of the pump rotation range. Minav et al. (2017) recorded the maximum gear hydraulic pump flow efficiency at the level of η = 0.91, however, based on the experiment conducted, higher values were recorded. Differences in values can be due to several factors, e.g. Minav et al. (2017) used a different type of hydraulic fluid in their measurement and loaded the hydraulic pump with a working pressure of 5 MPa at the same time. Kosiba et al. (2019) recorded the rotary gear hydraulic pump flow efficiency with external gearing of η = 0.9745 at 1500 rpm. The authors used a UD-20 pump with a different type of hydraulic fluid than it was used in the verification measurement presented. Simultaneously, they carried out the measurement in practice, i.e., during the tractor operation. Rizzo et al. (2015) observed the efficiency of hydraulic pump loaded with pressure at the level of 0.92.

Test laboratory equipment for measuring the parameters of hydrostatic transducers and hydraulic fluids allows the connection of several types of measuring chains. After modifications, it is possible to connect other types of measuring chains to the given device, making it usable for measuring the parameters of hydrostatic transducer, pumps or hydro-engine, or determination of properties of hydraulic fluids. For one type of measuring chains, it is possible to test the parameters of hydrostatic transducers or hydraulic fluids depending on the operating pressure and temperature, or the maximum pressure and temperature. The next measuring chain monitors the properties of hydraulic fluids during a step change in pressure in the hydraulic system. The designed test equipment allows several options for the connection of hydrostatic transducers and controls due to its modularity. For this reason, the proposed device can be used to test the parameters of hydrostatic transducers, hydraulic elements, or properties of hydraulic fluids depending on different conditions.

The results obtained point out the following benefits:

– on the basis of proposed laboratory test equipment, it is possible to

shorten the operational testing time of hydrostatic transducers, hydraulic fluids and hydraulic elements;
- utilizing the laboratory test equipment, it is possible to simultaneously test the parameters of two hydrostatic transducers;
- on the basis of acquired knowledge and measurement results of the hydrostatic transducer, it is possible to make changes in the construction of devices in question prior to their introduction to the production process;
- at the same time, it is possible to use the obtained hydrostatic transducer flow results to create dynamic flow models.

## Conclusion

The aim of presented research was to design a device that will be used for testing the parameters of hydrostatic transducers and properties of hydraulic fluids. Thanks to the designed laboratory test equipment, it is possible to shorten the testing time of hydrostatic transducers and hydraulic fluids, and, at the same time, the equipment allows repeatability of measurements. The device proposed allows the connection of several types of measuring chains for measuring and testing the parameters of hydrostatic transducers and hydraulic fluids. The device described can test two hydraulic fluids simultaneously under the same or different conditions and allows to repeatedly simulate the operating conditions of agricultural and forestry machinery.

With the help of verification measurement, the functionality of the subject measuring chain used for measuring and testing the parameters of hydrostatic transducers and hydraulic fluids in laboratory conditions was demonstrated. The test laboratory equipment proposed allows the creation of several types of measuring chains, which can be used to measure and test the properties of hydraulic fluids, parameters of hydrostatic transducers and hydraulic circuit elements. Utilizing the proposed laboratory test equipment, it is possible to shorten the operational testing time of hydrostatic transducers, hydraulic fluids and hydraulic elements.

## Acknowledgements

This work was supported by project VEGA 1/0155/18 "Applied research of the use of ecological energy carriers in agricultural, forestry and transport technology".

This work was supported by project KEGA 028SPU–4/2019 "Practical utilization of design and testing knowledge of transmission systems of hydraulic mechanisms of mobile agricultural and forestry machinery".

This work was supported by project APVV SK-PL-18-0041 "The development of scientific cooperation in the study of the effects of biofuels in road transport, including environmental impact".

## References

ČORŇÁK, Š. 2018. Identification of operating fluids with fingerprint method utilization. In 17th International Scientific Conference "Engineering for Rural Development", Jelgava, Latvia, pp. 2048–2053.

HALENÁR, M. – KUCHAR, P. 2017. Research of biodegradable fluid during operating test. In 24th International PhD Students Conference for Undergraduate and Postgraduate Students (MendelNet), Brno, Czech Republic, pp. 784–789.

KOSIBA, J. – ČORŇÁK, Š. – GLOS, J. – JABLONICKÝ, J. – VOZÁROVÁ, V. –PETROVIČ, A. – CSILLAG, J. 2016a. Monitoring oil degradation during operating tests. In Agronomy Research, vol. 14, no. 5, pp. 1626–1634.

KOSIBA, J. – JABLONICKÝ, J. – BERNÁT, R. – KUCHAR, P. 2016b. Effect of ecological hydraulic fluid on operation of tractor hydraulic circuit. In Trends in Agricultural Engineering 2016, pp. 317–322.

KOSIBA, J. – JABLONICKÝ, J. – BERNÁT, R. – ZÁLEŽÁK, Z. 2019. Flow characteristics of the tractor hydraulic circuit by application of the biodegradable synthetic fluid. In Trends in Agricultural Engineering 2019, pp. 269–274.

KUČERA, M. – ALEŠ, Z. – PEXA, M. 2016. Detection and characterization of wear particles of universal tractor oil using of particles size analyzer. In Agronomy Research, vol. 14, no. 4, pp. 1351–1360.

MARKIEWICZ-PATALON, M. – MUŚLEWSKI, L. – KASZKOWIAK, J. – SÓJKA, M. 2018. Analysis of efficiency of the vehicle transport facilities powered with diesel oil with additive of biocomponent. In IOP Conference Series Materials Science and Engineering, vol. 421, no. 4. pp. 1–8.

MINAV, T. – HEIKKINEN, J. – PIETOLA, M. 2017. Direct driven hydraulic drive for new powertrain topologies for non-road mobile machinery. In Electric Power Systems Research, vol. 152, pp. 390–400.

PUŠKÁR, M. – BRESTOVIČ, T. – JASMINSKÁ, N. 2015. Numerical simulation and experimental analysis of acoustic wave influences on brake mean effective pressure in thrust-ejector inlet pipe of combustion engine. In International Journal of Vehicle Design, vol. 67, no. 1, pp. 63–67.

PUŠKÁR, M. – JAHNÁTEK, A. – KURIC, I. – KÁDÁROVÁ, J. – KOPAS, M. – ŠOLTÉSOVÁ, M. 2019. Complex analysis focused on influence of biodiesel and its mixture on regulated and unregulated emissions of motor vehicles with the aim to protect air quality and environment. In Air Quality, Atmosphere and Health, vol. 12, no. 7, pp. 1–10.

RIZZO, G. – MASSAROTTI, G. P. – BONANNO, A. – PAOLUZZI, R. – RAIMONDO, M. – BLOSI, M. – VERONESI, F. – CALDARELLU, A. – GUARINI, G. 2015. Axial piston pumps slippers with nano-coated surfaces to reduce friction. In International Journal of Fluid Power, vol. 16, pp. 1–10.

SIMIKIČ, M. – DEDOVIČ, N. – SAVIN, L. – TOMIČ, M. – PONJIČAN, O. 2014. Power delivery efficiency of a wheeled tractor at oblique drawbar force. In Soil and Tillage Research, vol. 141, pp. 32–43.

TKÁČ, Z. – ČORŇÁK, Š. – CVIKLOVIČ, V. – KOSIBA, J. – GLOS, J. – JABLONICKÝ, J. – BERNÁT, R. 2017. Research of biodegradable fluid impacts on operating of tractor hydraulic system. In Acta Technologica Agriculturae, vol. 20, no. 2, pp. 42–45.

TKÁČ, Z. – MAJDAN, R. – DRABANT, Š. – JABLONICKÝ, J. – ABRAHÁM, R. – CVÍČELA, P. 2010. The accelerated laboratory test of biodegradable fluid type "ERTTO". In Research in Agricultural Engineering, vol. 56, no. 1, pp. 18–25.

TULÍK, J. – KOSIBA, J. – SZABÓ, M. – VARGA, F. – KANGALOV, P. – MAREČEK, J. 2015. Analysis of new biodegradable fluid during of the operating test. In Agricultural, Forest and Transport Machinery and Technologies, vol. 2, no. 1, pp. 11–15.

DOI: 10.2478/ata-2021-0007



Acta Technologica Agriculturae 1
Nitra, Slovaca Universitas Agriculturae Nitriae, 2021, pp. 41–47

# FORMATION OF CROP YIELDS OF ENERGY CROPS DEPENDING ON THE SOIL AND WEATHER CONDITIONS

Maroš KORENKO[1]*, Volodymyr BULGAKOV[2], Vasyl KURYLO[3], Maksym KULYK[4], Alexander KAINICHANKO[4], Yevhen IHNATIEV[5], Eva MATUŠEKOVÁ[1]

[1]Slovak University of Agriculture in Nitra, Slovakia
[2]National University of Life and Environmental Sciences of Ukraine
[3]Vinnytsia National Agrarian University, Vinnytsia, Ukraine
[4]Poltava State Agrarian Academy, Poltava, Ukraine
[5]Tavria State Agrotechnological University, Ukraine

The article presented discusses the need to use plant biomass made of energy crops grown in marginal soils as an alternative energy source. Variability of biometric indicators of the plant vegetative parts (productivity elements) was experimentally established: stem quantity per area unit and stem height depending on the soil and weather conditions. Based on the five-year research, there was observed a significant influence of soil and climatic growing conditions (average daily air temperature; rainfall; soil fertility) on formation of crop energy productivity. Results showed that the variability of stem density and height; dry phytomass productivity of millet switchgrass and giant miscanthus during observed years depended on the studied factors. Correlation-regression analysis proved and characterized the influence of soil and climatic conditions during the growing season of energy crops on the yield of dry phytomass of millet switchgrass and giant miscanthus in the central part of the Ukraine forest-steppe. The impact proportion share of weather conditions and plant productivity elements on the level of energy crops yields was calculated.

**Keywords:** millet switchgrass; giant miscanthus; biometric indicators of plants; phytomass productivity

Currently, there is a tendency for the gradual depletion of non-renewable energy resources (oil, gas, coal) all over the world. As Tian et al. (2017) pointed out, nowadays, world energy demand is covered using oil (35%), coal (23%), natural gas (21%) and by nuclear fuel (7%). All these resources are non-renewable. Given the significant projected increase in energy demand, experts estimate that coal reserves will last for 250–300 years, natural gas reserves for 50–70 years, and oil reserves for 30–40 years, which is why the world scientific community puts so much emphasis on alternative energy sources, especially on potential of plants (Mehmooda et al, 2017). At the same time, there is a significant number of biomass energy sources for biofuel production in Ukraine: crop residues, waste from wood industry, and energy crops (Kurylo et al., 2013). The last type is represented mainly by perennial plants, which are acclimated to the growing conditions and it is possible to produce a high yield of phytomass by their cultivation in low-yielding soils. Among them, the following crops are distinguished: perennial sorghum, miscanthus (ivory), switchggrass (millet rod), willow, etc. Energy crops are herbs, shrubs, fast-growing trees, or other plants, the phytomass of which can be used as biofuel feedstock. The most common are miscanthus, millet (switchgrass) and willow (Costanza et al., 2017). Millet switchgrass belongs to the family of cereals (Gramineae); it has hollow stems of different colours reaching up to 3 meters in height, forms an inflorescence – paniculate – that can have 15–50 cm length, and reproduces by seeds and rhizome division. Miscanthus belongs to the cereal family (Gramineae); the most frequent species are Miscanthus giganteus, Miscanthus sinensis, and Miscanthus sacchariflorus.

Plants of the Miscanthus giganteus species (giant miscanthus) are very tall – up to 5 meters – they form a powerful phytomass, with an average winter hardiness and drought resistance. Giant miscanthus was an allotriploid derived from Miscanthus sinensis and Miscanthus saccharifolius and its mother form was Miscanthus saccharifolius (Chramiec-Głąbik et al., 2012). It reproduces only vegetatively and is the most common species in Ukraine (Kulyk et al., 2019). Samson et al. (2005); Christian and Elbersen (1998) identified the benefits of using biomass made of millet switchgrass and miscanthus in energy and fibre production: high clean energy production per hectare; low costs; low plant nutrient requirements; low ash content in raw materials, high moisture utilization; wide spread; easy cultivation, easy adaptation to growing conditions for cultivation in low-yielding soils, and ability to store carbon in the soil. They recommend growing energy crops in low-productive soils and degraded lands (Matías et al., 2019), which can be considered marginal soils – these are soils, at which the agricultural production is economically inefficient due to the low soil fertility and environmental restrictions that result from soil degradation, hydrophobicity, etc.

**Contact address:** Maros Korenko, Faculty of Engineering, Slovak University of Agriculture in Nitra, e-mail: maros.korenko@uniag.sk

Furthermore, multiple scientists (Tang et al., 2010; Thakrar et al., 2018) associate the term "marginal soils" with the trends of land utilization, and later – with soil quality. Thakrar et al. (2018) has determined the level of soil organic carbon and its amount obtained from plant material. Their research in the US and India showed that the conversion of crop residues to organic carbon and $CO_2$ is more of a conservation process occurring around the world. Mathematical calculations determined that the carbon intensity and the amount of $CO_2$ from plant residues per unit of energy in biofuels does not depend on the amount of residue removed and the location of the raw materials (Macák et al., 2015). According to Thakrar et al. (2018), the economic impact of the use of bio resources is partially dependent on the ability of the management to strategically identify land for the transition from current use to obtaining of raw materials for bio resource production.

Along with the findings of Baxter et al. (2014) regarding the use of agricultural biomass for energy purposes, Tang et al. (2010) analysed the current status and future potential of China's marginal land resources, energy savings and energy reductions of harmful emissions. At the same time, the findings indicate that the country has enormous energy potential in terms of marginal land resources. Kulyk (2019) observed changes in soil at multiyear plantations of energy crops: the soil level in the layer 0–30 cm decreases, the content of available phosphorus in soil increases by 8–13%, changes in calcium and magnesium are minor (except for miscanthus plantations in which the first indicator decreased), changes in total nitrogen content are relatively large (4% more than in control samples).

Simultaneously, Čedík et al. (2018) pointed out the need to study environmental factors of the most common alternative fuel production – biodiesel biofuels made of bio-raw materials.

Given the significance of the aforementioned, this paper pays attention to:

- determination of variability of the plant productivity elements of millet switchgrass and giant miscanthus depending on the growing conditions;
- determination of relationship between the plant biometrics and yield of dry phytomass of these energy crops;
- determination of influence of the soil and weather conditions on the yield of conditionally wet and dry phytomass of millet switchgrass and giant miscanthus.

## Material and methods

Experimental work was carried out at Poltava State Agrarian Academy on the basis of scientific international project "P4R" (2010–2013) established between the Netherlands and Ukraine, state research topic "Agro-ecological principles of cultivation of energy crops in Ukraine" (2014–2017), and the applied research scientific project of the Ministry of Education and Science of Ukraine "Development of optimal energy systems taking into account the existing potential of renewable energy sources in the conditions of the forest-steppe of Ukraine" (2017–2019). Experiment with energy crops (millet switchgrass and giant miscanthus) took place in the central part of the forest-steppe of Ukraine at the state agricultural enterprise "Jubilee" in Poltava district, village Brychkivka. Annual precipitation in this area is 450–550 mm; irrigation rate ranges from 1.9 to 1.3. Crops were planted in the experimental plot in 2010, and experimental studies were conducted during the period since 2012 to 2016. The experiment observed the cultivation of energy crops (millet switchgrass and giant miscanthus):

- option 1 – high-yielding soils – FS (humus content over 1.5%);
- option 2 – marginal lands soils – MF (humus content less than 1.5%).

In terms of climate and soil, the conditions were typical for this region and all technological operations were carried out simultaneously in both plots with energy crops: soil cultivation (autumn and spring); sowing of millet switchgrass seeds and planting giant miscanthus with the weeding in the optimal time, as weeds appear in the first and beginning of the second year of a plant vegetation. Further soil cultivation was not carried out, since the energy crops shaded row spacing with their phytomass, thus suppressing the weeds.

Over the research years, the energy crops were subjected to conventional (Dospehov, 1985), as well as special research methods (Kurylo et al., 2013). Each year since 2012 to 2016, the experiments were repeated four times, the options were placed randomly, the total plot area for each crop was 60 $m^2$, and the area of the reference plot was 50 $m^2$.

In order to ensure the experiment reliability, the numbers of stems and plant heights of millet switchgrass and giant miscanthus plants were determined as the arithmetic average of 50 plants of each crop from the selected sheaf samples for each variant and this process was repeated four times in each year.

In order to prevent errors during the experiment, the productivity and yield of phytomass of energy crops were determined from the sheaf samples, which were diagonally sampled four times and weighed. Subsequently, the selected average sample was dried, and the dry weight mass was calculated taking into account the moisture content of the raw material at the end of the growing season (Ben Fradj et al., 2020; Kulyk et al., 2019).

The obtained research results were processed by means of analysis of variance in Statistaca 6.0.

The theoretical value of the Fisher test ($F$) was found based on the degrees of freedom for the variance of options and degrees for error. If the actual Fisher criterion is more than theoretical ($F_a > F_{05}$), then there are significant variations in the experiment and the null hypothesis is rejected.

On order to determine the significant differences, the following was calculated:

1. experiment error ($S_x$) and the difference of the standard deviation ($S_d$):

$$S_x = \sqrt{\frac{s^2}{n}}, \quad S_d = \sqrt{\frac{2s^2}{n}} \tag{1}$$

where:

$s^2$ – dispersion
$n$ – number of repetitions

2. the least significant difference for the 5% significance level ($HIP_{05}$) in absolute and relative terms:

$$HOP_{05} = t_{05} S_d \quad (2)$$

$$HIP_{05} = \frac{t_{05} S_d}{\bar{x}} 100 \quad (3)$$

where:
$t_{05}$ – tabular values of the criterion $t$ for a 5% significance level
$\bar{x}$ – arithmetic mean value

The coefficient of variation was determined as the ratio of the standard deviation ($S$) to the average level ($x$):

$$V = \frac{s}{\bar{x}} 100 \quad (4)$$

The smaller the coefficient of variation, the smaller the fluctuation of the trait in the aggregate and more homogeneous aggregate, and vice versa. The following values of relative fluctuations (variations) were used: insignificant – $V$ <10%; average – $V$ = 10.1–30%; large – $V$ >30%.

The correlation coefficients between the quantitative indices of plants (number of stems, plant height) and the dry phytomass yield of millet switchgrass and giant miscanthus were determined using the correlation-regression analysis. The linear correlation dependence was expressed by the regression equation $y = a + bx$.

To estimate the reliability of the correlation coefficient, its error ($sr$) and materiality criteria ($t_r$) were calculated as follows:

$$sr = \sqrt{\frac{1-r^2}{n-2}}, \quad t_r = \frac{r}{s_r} \quad (5)$$

where:
$r$ – correlation coefficient

If $t_r > t_{theor}$ (theoretical value of the criterion), then correlation is significant and vice versa. It was accepted that if $r$ <0.3, the correlation is weak; if $r$ = 0.3–0.7, the correlation is average, and if $r$ >0.7, then the correlation is strong.

## Results and discussion

Weather conditions during the vegetative period of energy crops since the third to seventh year (2010–2016) were dynamically changing and showed values of temperature and rainfall that differed from the average long-term data (Figs. 1–2).

The aboveground vegetative mass of millet switchgrass and giant miscanthus for biofuel purposes was harvested after the third year of vegetation – this is due to rooting, growth rate and plant development, which determines the yield potential (Fig. 3). For this very reason, the study results for energy crops are presented since 2012.

Under the conditions of the central forest-steppe, the number of plant stems of millet switchgrass varied from 24.0 to 70.1 pcs. when cultivated in high-productive soils (the coefficient of variation V was 42.1%); the number of plant stems of giant miscanthus varied from 12.1 to 23.4 pcs. ($V$ = 39.3%). Considering the marginal soils, this indicator varied from 21.3 to 34.1 pcs. with a coefficient of variation $V$ = 17.8% for millet switchgrass and from 11.4 to 21.3 pcs. with a coefficient of variation $V$ = 25.8% for giant miscanthus. When cultivated in high-productive soils, the height of millet switchgrass plants since the third to seventh year of vegetation varied from 110.3 to 172.1 cm ($V$ = 34.7%); in marginal soils, this indicator varied from 112.4 to 179.3 cm ($V$ = 15.4%).

Considering the giant miscanthus, there was observed a tendency to increase the plant height (since the

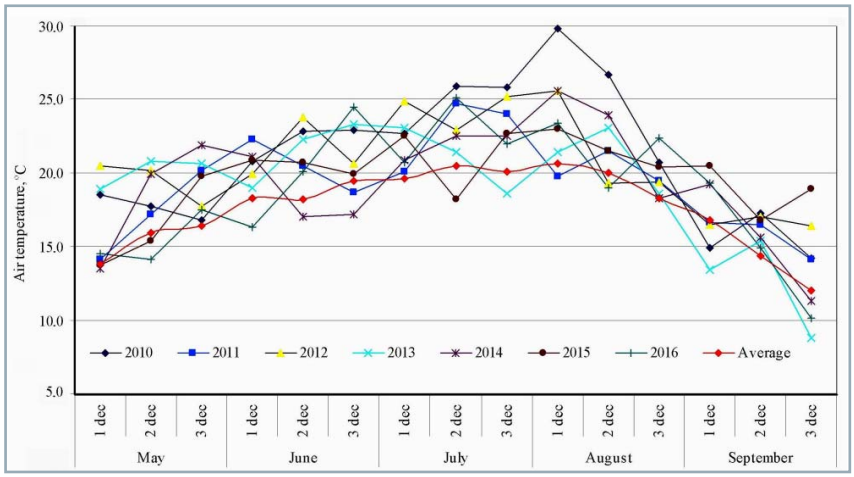


**Fig. 1** Average decade air temperature in comparison to long-term average data (average *b/d*) during the vegetation of energy crops (2010–2016)

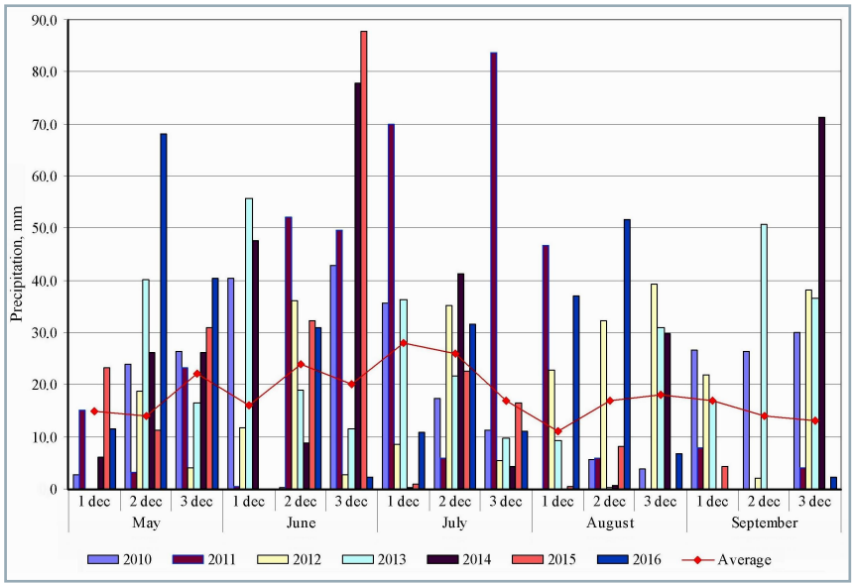


**Fig. 2** Average decade rainfall in comparison to the long-term average data (average *b/d*) during the vegetation of energy crops (2010–2016)

| Cultures | 2010 year | | | | 2011 year | | | | 2012 year | | | | 2013 year | | | |
|---|---|---|---|---|---|---|---|---|---|---|---|---|---|---|---|---|
| | s* | su | a | w | s | su | a | w | s | su | a | w | s | su | a | w |
| Millet switchgrass | | | | | | | | | | | | | | | | |
| Giant miscanthus | | | | | | | | | | | | | | | | |
| *Marking:* | | | | | | | | | | | | | | | | |
| | | sowing / planting | | | | | | | plant care | | | | | | | |

| Cultures | 2014 year | | | | 2015 year | | | | 2016 year | | | | 2017 year | | | |
|---|---|---|---|---|---|---|---|---|---|---|---|---|---|---|---|---|
| | s | su | a | w | s | su | a | w | s | su | a | w | s | su | a | w |
| Millet switchgrass | | | | | | | | | | | | | | | | |
| Giant miscanthus | | | | | | | | | | | | | | | | |
| *Marking:* | | | | | | | | | | | | | | | | |
| | | harvesting | | | | | | | | | | | | | | |

**Fig. 3** Logistic chain of cultivation, plant care and harvesting of energy crops, 2010–2017
s – spring period, su – summer period, a – autumn period, w – winter period

third to seventh year of vegetation) in high-productive soils – from 172.1 to 345.8 cm ($V$ = 41.2%); the number of plant stems varied from 15.3 to 202.3 pcs. ($V$ = 64.7%). In marginal soils, the plant height varied from 162.2 to 325.5 cm ($V$ = 24.4%) and the number of plant stems varied from 12.1 to 23.4 pcs. ($V$ = 26.8%).

The greatest increase in plant height for millet switchgrass was observed during the spring and summer, and in the spring for giant miscanthus, with an increase in growth rates in the spring and summer and a gradual decrease in July–August. This is primarily due to the amount of precipitation during this period and is confirmed by the conclusions of previous studies (Kulyk et al., 2019) and the results of other authors (Wang et al., 2015), who conducted similar research.

Along with the results of previous studies regarding the characteristics of the formation of energy crop yields (Kulyk et al, 2019), Kurylo et al. (2013), Ben Fradj et al. (2020), and Macák et al. (2015) argue that, in contrast to agro-technical measures, cultivation conditions make a significant contribution to the yields of millet switchgrass and giant miscanthus. Therefore, this publication focuses on the study of the influence of soil and weather conditions of vegetation on the energy crop yields.

The highest values of quantitative indicators (density and height of the stem) for millet switchgrass and giant miscanthus were obtained during the period of the third to fifth year of vegetation when grown in high-productive soils. When cultivated in marginal soils, the productivity indicators (number of stems, plant height, etc.) were significantly lower in contrast to the high-productive soils. Regardless of the growing conditions, the highest values of plant quantitative indicators were obtained during the period of the sixth to seventh year of vegetation, which was also confirmed by previous study (Kulyk et al., 2019).

It was determined that during the cultivation of millet switchgrass, the phytomass moisture content varied from 23.1 to 25.0% in high-productive soils, and from 20.0 to 25.2% in marginal soils. The higher yield of dry phytomass was recorded with the cultivation of millet switchgrass in high-productive soils during the period since the third to seventh year of vegetation (14.7–19.3 t·ha$^{-1}$; Fig. 4).

The moisture content in giant miscanthus phytomass was slightly different compared to millet switchgrass, and the productivity of the stem and plants increased since the third to seventh year of the vegetation under different growing conditions. Its moisture content varied from 24.2 to 33.1% when cultivated in high-productive soils, and from 29.1 to 33.0% when cultivated in marginal soils and depended on the weather conditions. The highest yield of dry miscanthus phytomass was shown by samples cultivated in high-productive soils during the fourth and sixth year of vegetation (16.7–23.9 t·ha$^{-1}$).

According to the results of the correlation and regression analysis at a 5% level of significance, it was determined that the number of stems of one plant has the greatest influence on the productivity of dry phytomass of millet switchgrass and giant miscanthus (Figs. 5–8).

The established regression dependence indicates that the increase in yield of dry phytomass of millet switchgrass under the Central Forest Steppe conditions is more determined by the number of stems per unit area ($R$ = 0.78) than the height of plants ($R$ = 0.39).

In terms of giant miscanthus, the following dependence was established: with an increase in its stem density ($R$ = 0.85) and height ($R$ = 0.75), the dry phytomass yield will increase and vice versa.

Weather conditions (average daily air temperature and precipitation amount during the growing season May–September) also significantly contribute to the formation of the phytomass yield of energy crops taken for the study (Table 1).

The yield of energy crops in marginal soils showed a strong inverse

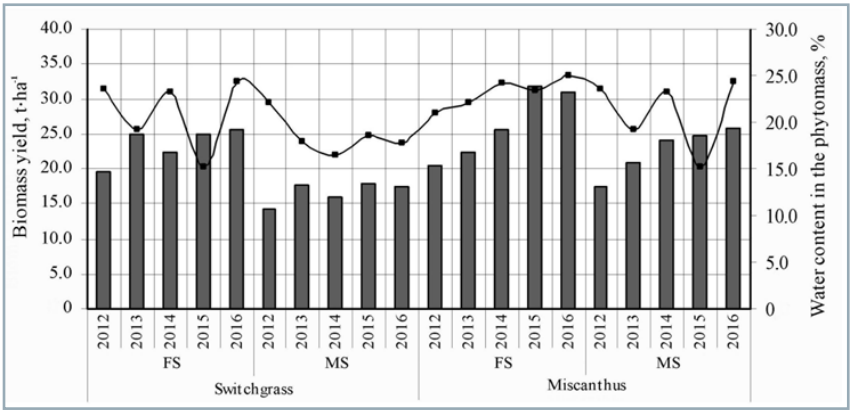


**Fig. 4** Productivity and moisture content in the phytomass of energy crops during the period of 2012–2016
$HIP_{05}$ (cultures) = 2.71; $HIP_{05}$ (soils) = 5.04; $HIP_{05}$ (years) = 1.68; FS – highly-productive soils; MS – marginal soils

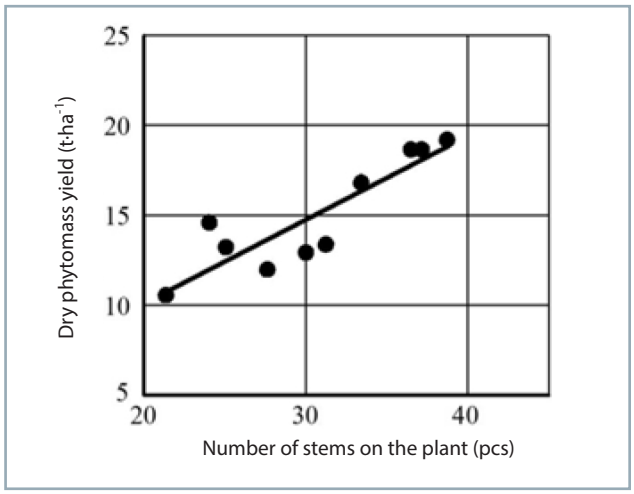


**Fig. 5** Relationship between stem density and phytomass yield of millet switchgrass (2012–2016)

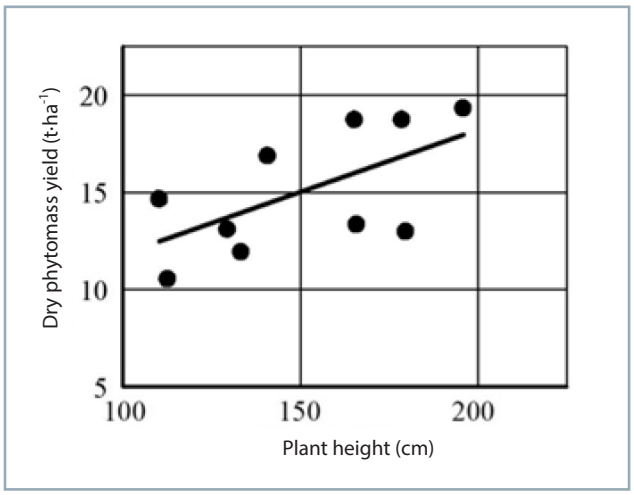


**Fig. 7** Relationship between plant height and phytomass yield of millet switchgrass (2012–2016)

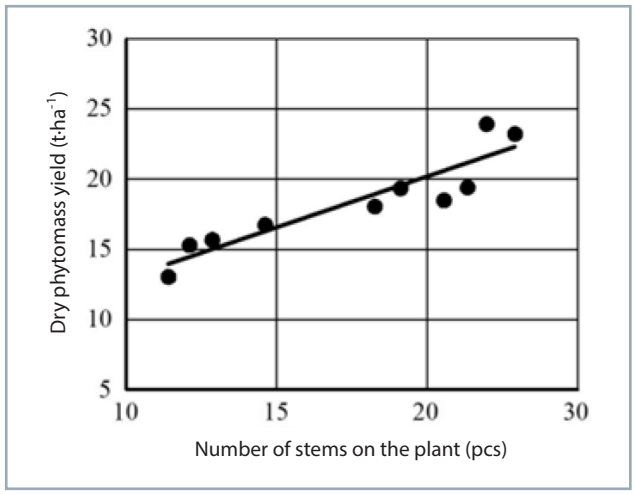


**Fig. 6** Relationship between stem density and yield of giant miscanthus phytomass (2012–2016)

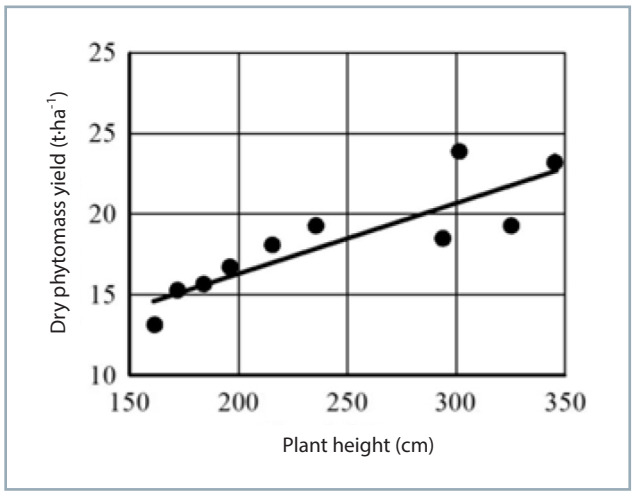


**Fig. 8** Relationship between plant height and phytomass yield of giant miscanthus (2012–2016)

relationship with the average daily air temperature, which indicates that the increase in one indicator will decrease the other and vice versa. To a moderate degree, the yield of giant miscanthus was influenced by the volume of precipitation during plant vegetation in high-productive soils; when grown in marginal soils, this relationship disappeared.

Determining the degree of influence of studied factors on dry phytomass yield of energy crops made it possible to single out the most significant among them (them (Figs. 9a and 9b).

Considering the long-term cultivation of millet switchgrass in high-productive soils and marginal soils, their yield was determined by the number of stems per unit area (38.3 and 35.0%, respectively), the average daily air temperature during the growing season (31.2 and 30.3%) and the dry content substances in phytomass (15.3 and 15.0%); the productivity was affected to a lesser extent by

**Table 1** Coefficients of linear correlation between weather conditions and dry phytomass yield of energy crops (Pearson), 2012–2016

| Crops | Conditions | The average daily air temperature (°C) | Correlation relationship | Precipitation (mm) | Correlation relationship |
|---|---|---|---|---|---|
| **Millet switchgrass** | high-productive soils | -0.87* | strong | 0.08 | weak |
| | marginal soils | -0.79* | strong | 0.03 | weak |
| **Giant miscanthus** | high-productive soils | -0.54* | average | 0.46* | average |
| | marginal soils | -0.77* | strong | - 0.07 | weak |

* Note: relationships are significant at 5% significance level

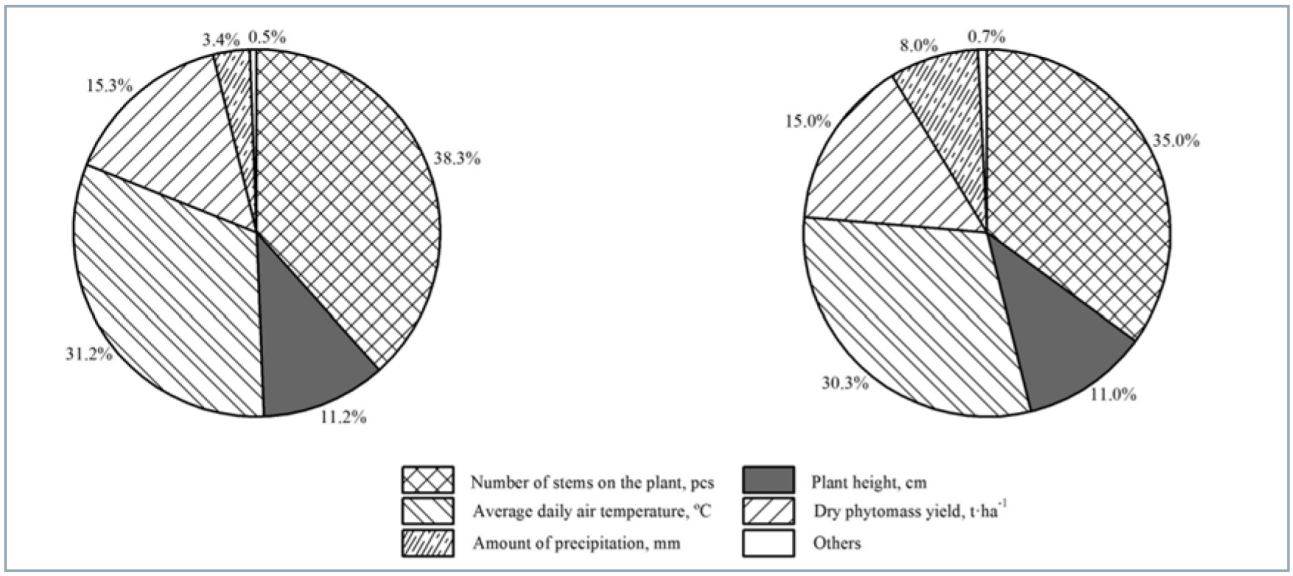


**Fig. 9** Effect of plant quantitative indicators and weather conditions on the dry phytomass yield of millet switchgrass in 2012–2016 when cultivated in a) high-productive soils; b) marginal soils

plant height (11.2 and 11.0%), the precipitation amount during the growing season (3.4 and 8.0%), rest of the factors showed effect less than 0.7%.

The phytomass yield of giant miscanthus over the research years in high-productivity soils and marginal soils was produced thanks to the height of plants (23.9% and 25.6%, respectively), the number of stems per unit area (20.9% and 28.8%, respectively), average daily temperature during the growing season (16.9% and 22.5%), dry matter content in the phytomass (14.0% and 14.1%), and the amount of precipitation during the growing season (23.3% and 7.9%), other factors showed significance less than 0.8%.

## Conclusion

It has been determined that at present, cultivation possibility of multiyear energy crops (millet switchgrass and giant miscanthus) in marginal soils as a raw material for the purposes of biofuel production in both Ukraine and abroad was investigated. In the long-term run, this should reduce energy dependence of Ukraine on imported energy sources by utilization of renewable energy sources.

Over the years of research, there was observed a significant variation in the biometric characteristics of energy crops when cultivated in high-productive soils and marginal soils; differences in productivity indicators were of average values. Millet switchgrass showed the largest increase in the productivity indicators: the highest stem density and plant height occurred from the fourth to sixth vegetation year. Considering the giant miscanthus plants, these indicators increased since the third to seventh vegetation year. Another trend was observed in the cultivation of these crops in marginal soils – there was a clear trend towards an increase in biometric indicators starting since the third to seventh vegetation year.

An increase in plant biometric parameters at the end of the vegetation season, especially the plant height in more fertile soils, is more characteristic for giant miscanthus than for millet switchgrass. Millet switchgrass showed an increase in plant density during cultivation in more fertile soils (with humus content greater than 1.5%) in contrast to less fertile marginal soils (with humus content less than 1.5%), in which the increase in plant height was recorded at the cost of stem density reduction.

In marginal soils, millet switchgrass showed a trend towards an increase in the yield since the third to seventh vegetation year ranging from 10.6 to 13.0 t·ha$^{-1}$; giant miscanthus showed yield increase from 13.1 to 19.3 t·ha$^{-1}$. In relation to high-productive soils, giant miscanthus showed an increase in this indicator in the fourth to sixth vegetation year – from 16.7 to 23.9 t·ha$^{-1}$ compared to millet switchgrass, yield of which increased in the third to seventh vegetation years under these conditions – from 14.7 to 19.3 t·ha$^{-1}$.

In general, under the conditions of the central forest-steppe of Ukraine, the yield of phytomass of energy crops depends on the productivity of each plant regarding the phytocenosis, biometric indicators and growing conditions. The increase in the dry phytomass yield of millet switchgrass, depending on soil conditions of cultivation, is more determined by the number of stems per unit area. Considering the giant miscanthus, it is additionally determined by the plant height. The yield of energy crops in marginal soils depends on the average daily air temperature; the precipitation amount has a less significant effect on this indicator, with the exception of the giant miscanthus.

## References

BAXTER, X. C. – DARVELL, L. I. – JONES, J. M. – BARRACLOUGH, T. – YATES, N. E. – SHIELD I. 2014. Miscanthus combustion properties and variations with Miscanthus agronomy. In Fuel, vol. 117, part A, pp. 851–869. doi.org/10.1016/j.fuel.2013.09.003

BEN FRADJ, N. – ROZAKIS, S. – BORZECKA, M. – MATYKA, M. 2020. Miscanthus in the European bio-economy: A network analysis. In Industrial Crops and Products, vol. 148, 112281. doi.org/10.1016/j.indcrop.2020.112281

ČEDÍK, J. – PEXA, M. – PETERKA, B. – HOLŮBEK, M. – MADER, D. – PRAŽAN, R. 2018. Effect of biobutanol-sunflower oil-diesel fuel blends on combustion characteristics of compression ignition engine. In Acta Technologica Agriculturae, vol. 21, no. 4, pp. 130–135. doi.org/10.2478/ata-2018-0024

COSTANZA, J. K. – ABT, R. C. – McKERROW, A. J. – COLLAZO, J. A. 2017. Bioenergy production and forest landscape change in the southeastern United States. In GCB Bioenergy, vol. 9, pp. 924–939. doi.org/10.1111/gcbb.12386.

CHRAMIEC-GŁABIK, A. – GRABOWSKA-JOACHIMIAK, A. – SLIWINSKA, E. – LEGUTKO, J. – KULA, A. 2012. Cytogenetic analysis of Miscanthus × giganteus and its parent forms. In Caryologia, vol. 65, no. 3, pp. 234–242.

CHRISTIAN, D. G. – ELBERSEN H. W. 1998. Switchgrass (*Panicum virgatum* L.). In: BASSAM N. El. Energy Plant Species. Their Use and Impact on Environment and Development. London: James and James Publishers, pp. 257–263. https://www.researchgate.net/publication/229013519_Switchgrass_variety_choice_in_Europe

DOSPEHOV, B. A. 1985. Field Experience Technique. USSR, Moscow: Agropromizdat, 336 pp. (In Russian: Metodika polevogo opyita).

KULYK, M. – GALYTSKA, M. – SAMOYLIK, M. – ZHORNYK, I. 2019. Phytoremediation aspects of energy crops use in Ukraine. In Agrology, vol. 1, no. 4, pp. 373–381. http://dspace.pdaa.edu.ua:8080/handle/123456789/4157

KURYLO, V. L. – ROIK, M. V. – HANZHENKO, O. M. 2013. Bioenergy in Ukraine: status and prospects for development. In Bioenerhetyka, vol. 1, pp. 5–10. (In Ukrainian: Bioenerhetyka v Ukraini: stan ta perspektyvy rozvytku).

MACÁK, M. – NOZDROVICKÝ, L. – HUSSEIN, A. O. 2015. Effect of preheating and different moisture content of input materials on durability of pellets made from different phytomass content. In Acta Technologica Agriculturae, vol. 18, pp. 22–27.

MATÍAS, J. – CRUZ, V. – GARCÍA, A. – GONZÁLEZ, D. 2019. Evaluation of rice straw yield, fibre composition and collection under mediterranean conditions. In Acta Technologica Agriculturae, vol. 22, pp. 43–47.

MEHMOODA, M. A. – IBRAHIMB, M. – RASHIDC, U. – NAWAZD, M. – ALIB, S. – HUSSAINA, A. – GULLE, M. 2017. Biomass production for bioenergy using marginal lands. In Sustainable Production and Consumption. vol. 9, pp. 3–21. doi.org/10.1016/j.spc.2016.08.003

SAMSON, R. – MANI, S. – BODDEY, R. – SOKHANSANJ, S. – QUESADA, D. – URQUIAGA, S. 2005. The potential of C4 perennial grasses for developing a global BIOHEAT industry. In Critical Reviews in Plant Sciences, vol. 24, pp. 461–495. doi.org/10.1080/07352680500316508

TANG, Y. – XIE, J. S. – GENG, S. 2010. Marginal land-based biomass energy production in China. In Journal of Integrative Plant Biology, vol. 52, pp. 112–121. doi.org/10.1111/j.1744-7909.2010.00903.x

THAKRAR, S. K. – GOODKIND, A. L. – TESSUM, C. W. – MARSHALL, J. D. – HILL, J. D. 2018. Life cycle air quality impacts on human health from potential switchgrass production in the United States. In Biomass and Bioenergy, vol. 114, pp. 73–82. doi.org/10.1016/j.biombioe.2017.10.031

TIAN, S. – CACHO, J. F. – YOUSSEF, M. A. – CHESCHEIR, G. M. – FISCHER, M. – NETTLES, J. E. – KING, J. S. 2017. Switchgrass growth and pine–switchgrass interactions in established intercropping systems. In GCB Bioenergy, vol. 9, pp. 845–857. doi.org/10.1111/gcbb.12381

WANG, L. – QIAN, Y. – BRUMMER, J. E. – ZHENG, J. – WILHELM, S. – PARTON, W. J. 2015. Simulated biomass, environmental impacts and best management practices for long-term switchgrass systems in a semi-arid region. In Biomass and Bioenergy, vol. 75, pp. 254–266. doi.org/10.1016/j.biombioe.2015.02.029.

DOI: 10.2478/ata-2021-0008



Acta Technologica Agriculturae 1
Nitra, Slovaca Universitas Agriculturae Nitriae, 2021, pp. 48–54

# ARTIFICIAL INTELLIGENCE-DRIVEN AUTONOMOUS ROBOT FOR PRECISION AGRICULTURE

Ivan BELOEV, Diyana KINANEVA, Georgi GEORGIEV, Georgi HRISTOV*, Plamen ZAHARIEV

University of Ruse "Angel Kanchev", Ruse, Bulgaria

In the recent years, robotic systems became more advanced and more accessible. This has led to their slow, but stable integration and use in different processes and applications, including in the agricultural domain. Nowadays, agricultural robots are developed with the aim to replace the human labour in the otherwise exhausting, time-consuming or dangerous activities. Agricultural robotic systems provide many advantages, which can differ based on the type of the robot and its sensors, actuators and communication systems. This paper presents the design, the construction process, the main characteristics and the evaluation of a prototype of a small-scale agricultural robot that can be used for some of the simplest activities in agricultural enterprises. The robot is designed as an end-user autonomous mobile system, which is capable of self-localization and can map or inspect a specific farming area. The decision-making capabilities of the robot are based on artificial intelligence (AI) algorithms, which allow it to perform specific actions in accordance to the situation and the surrounding environment. The presented prototype is in its early development and evaluation stages and the paper concludes with discussions on the possible further improvements of the platform.

**Keywords:** computer vision algorithms; robotics; simultaneous localization and mapping; visual navigation; visual odometry; smart farming

Precision agriculture, and more specifically precision farming, involves the use of modern information and communication technologies, which are implemented with the aim to increase crop yields and profitability. At the same time, precision agriculture leads to an overall decrease of the amount of investments and resources, in terms of arable land, water, fertilizers, herbicides, insecticides, etc., which are needed to grow the crops. Some of the technologies that are used in the precision agriculture domain, include online weather forecasts, sensor systems and networks, satellite systems, NDVI and photographic systems, systems for weed detection, etc. The information provided by these solutions needs to be analysed before it can produce agronomic recommendations or instructions, but in this way precision agriculture can provide farmers with the knowledge about the needed resources, as well as with information in what amount and when they should be applied.

The timely delivery of the agronomical recommendations is a key factor for the improvement of the quality and the quantity of yields. However, these recommendations typically involve or require a specific action to take place. Of course, farmers do not have to perform these activities by hands or on their own – they can use robots and mobile autonomous systems (Krastev and Georgiev, 2015). The use of robots for precision agriculture is not a new trend. Over several decades, the robots for precision agriculture have been subject to developments and upgrades and their modern versions are smarter and can make decisions on their own by using different input parameters (Amer et al., 2015).

There are several different types of precision agriculture robots (Cheein and Carelli, 2013). The ground-based open space robots are probably the most widely distributed and used (Cosgrove, 2017). The robots for greenhouse or indoor farming form the second group. The possibility to monitor the crops from the air has provided priceless information to farmers in the past and has increased the yields significantly (Yaghoubi et al., 2013). For this reason, the aerial unmanned robotic platforms have slowly defined a standalone category of precision agriculture robots. In the last decade, the main research efforts in the precision agriculture area are focused on the development of small-scale flexible and highly mobile solutions, which can be used both indoors and outdoors, and even in urban conditions, like for example on the rooftops of the buildings (Farmaid, 2020) or in backyards.

The improvement of the autonomous movement and navigation capabilities of precision agriculture robots is one of the most widely researched areas (Bakker et al., 2010). The most trivial navigation method is based on satellite triangulation and allows the robot to move through the open field towards the desired endpoint (Bakker et al., 2010). Due to numerous disadvantages of this approach and its inaccuracy, many of the modern agricultural machines (Claas 700, 2020; Fendt, 2020; John Deere, 2020) have also visual feedback control – using optical or electro-optical cameras (Pierpaoli et al., 2013), ultrasonic proximity sensors or Light Imaging, Detection and Ranging (LIDAR) systems. The movement of the robots in the field is also a significant challenge for the ground-based robots

**Contact address:** Georgi Hristov, University of Ruse "Angel Kanchev", Department of Telecommunications, Ruse, Bulgaria, e-mail: ghristov@uni-ruse.bg

(Hernández et al., 2013), as well as the improvement of the tools used for seeding, transplanting, fertilizing and harvesting (Claas Isaria, 2020). The indoor robots also suffer from many disadvantages and are usually limited to the manipulation on just one fruit or vegetable, mainly due to the limitations of the technological solutions and the restricted working spaces (Belforte et al., 2006, Farmaid, 2020). On the other hand, Unmanned Aerial Vehicles (UAVs), like the T16 by DJI (DJI Agras T16, 2020), can be used for insect and weed control for a variety of crops, such as rice, wheat, corn, citrus trees, cotton, and much more. Nevertheless, these robotic systems are very difficult to control and sometimes require special permits to be operated (Hristov et al., 2016).

In this paper we present our efforts to develop a small-scale mobile robot for precision agriculture that can be used both indoors and outdoors. Our aim is focused on the evaluation of modern technologies that can be used for the construction of the robot, and we are driven by the goal to produce the cheapest possible solution, which will be easy to operate and will be able to perform the basic tasks, like weed detection, spraying, etc. To solve the navigation issues described above, we have investigated the possibility to use both GPS-based navigation solution and a visual navigation solution that is based on depth and tracking cameras.

## Material and methods

The presented robot prototype is a highly efficient autonomous small-scale, ground-based mobile platform that uses advanced computer vision methods to distinguish different objects, colours and plants and can apply a liquid mixture using its on-board sprinklers. The general architecture of the robot, its hardware layers and the connections between them are presented in Fig. 1.

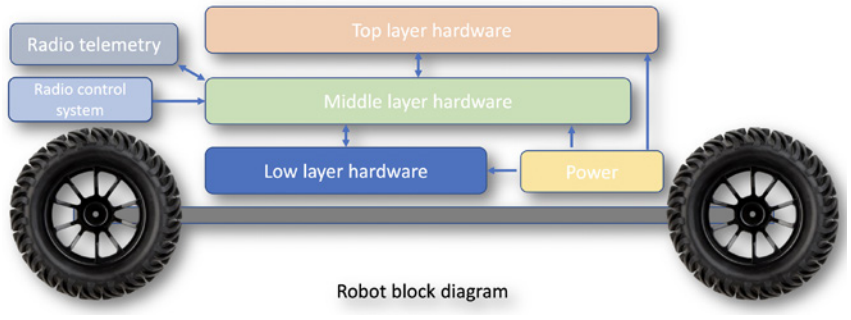


**Fig. 1** Block diagram of the general architecture of the agricultural robot prototype

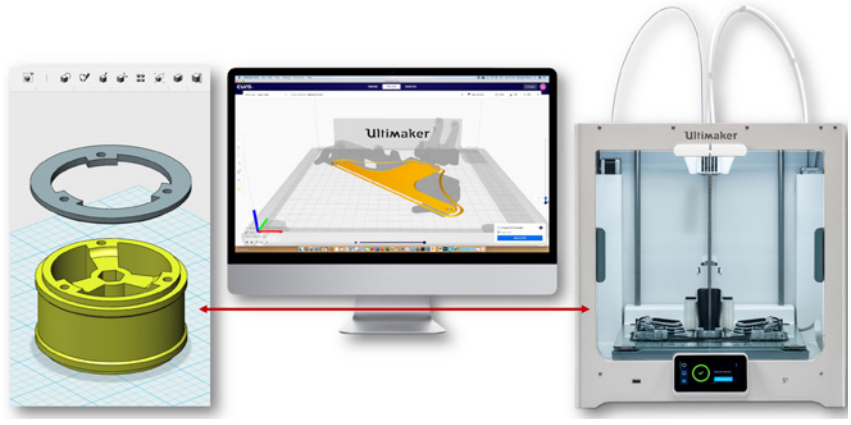


**Fig. 2** Design of the different elements of the robot chassis, adjustment of the components, positioning and preparation of the models in the software for 3D printing

The lower layer of the presented hardware architecture includes the motors and the motor drivers. This layer is responsible for the propulsion and the steering of the robot. The middle hardware level provides the robot with its autonomous movement and path-planning capabilities. To provide communication redundancy and remote control, the robot was equipped with numerous communication systems, which are under the control of the autopilot board. Some of these systems, like the GPS system, are part of the middle layer hardware and are directly used by the autopilot board, while the others, like the telemetry system and the remote control receiver, are communicating with the autopilot board using different interfaces. The top layer of the presented architecture includes a microcomputer and an optical camera, which are responsible for the computer vision tasks.

Designing a complete robot from scratch is not an easy task – the process requires significant knowledge in the areas of computer modelling, computer aided design (CAD), electronics, radio communications, mechanics and automation, and in our case – in the area of additive technologies and 3D printing. From application point of view, the robot must be able to cope up with clods and bumps, as well as to move between the furrows using appropriate algorithms and without damaging the plants. For this reason, the robot has a four-wheeled off-road chassis with front and rear suspension and high clearance. The parts for the body of the robot are modelled in Autodesk 123D Design (123D Design, 2020) and then printed using 3D printers (Fig. 2).

The propulsion system of the robot is implemented using two brushed DC motors with integrated encoders. They have metal gearboxes and are intended for operation at a nominal voltage of 12V. The motors have gear ratio of 19:1, which provides 500 rpm without load. The motors are powered using a Polulu VNH5019 dual motor driver shield, designed to control two bidirectional, high-power brushed DC motors. For turning left and right, the prototype of the smart robot uses a steering servomotor HDKJ D3625, which is extremely suitable for the

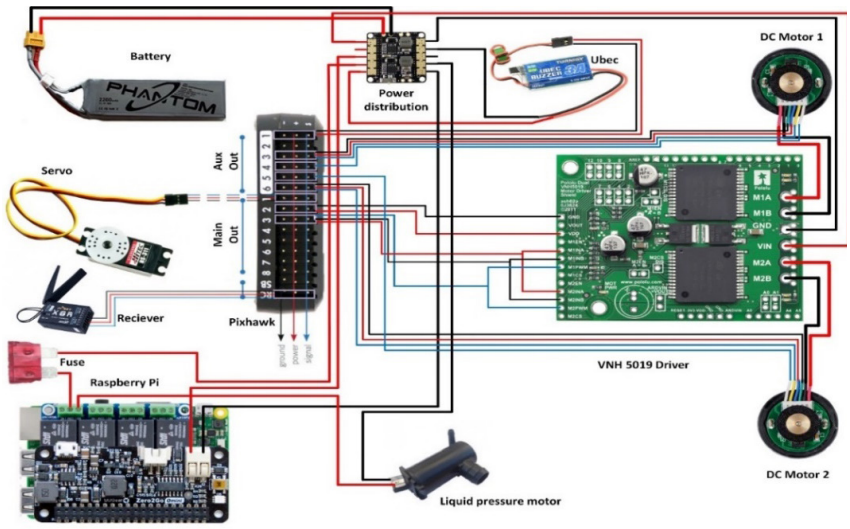


**Fig. 3** Wiring and power supply diagram of the smart agricultural robot

purpose of the robot, as well as for remotely controlled drones and cars.

Figure 3 presents the wiring and power supply diagram of the robot. Additionally, the figure shows how the DC motors are connected to the driver board and how the connection between the board and the Pixhawk microcontroller is made. The drivers are installed in a mirror configuration, so it was required to reverse the polarity of the power supply to one of the motors. Since the motors are DC, the change of the polarity will reverse the direction of rotation of the motor shaft and will synchronize the direction of rotation of both motors. The Pixhawk autopilot controls the motor driver via PWM signals. These signals have different levels, in order to determine the direction of the movement. A high-level signal will drive the robot forward, while a low-level signal will drive the robot backwards. The Pixhawk microcontroller controls all the hardware components of the middle layer, which are above the DC motors, the motor driver shield and the servo controller. Some of the connected components are required, while others are optional. For example, the primary GPS and compass are required to provide the autopilot with positioning data during movement, while the secondary GPS system is an optional component and is used to improve the localization precision.

The precision agriculture robotic platform that is presented in this paper relies on computer vision and image processing algorithms for the automatic detection of weeds and colours, as well as for the visual navigation and the avoidance of obstacles. Supervised machine learning approaches, which are relevant to the functionality of the robot, were investigated and used for the evaluation of its performance. They include four machine learning problems, namely classification, localization, object detection and segmentation, which are somewhat common, but differ in the produced outputs (Fig. 4).

In order to perform the object detection tasks, we use deep neural classification models. Their convolutional layers are the key component, which enables image processing and object detection. Usually, they are referred to as filters, which extract features from the previous layers in order to transform the input data in a form that is more useful for representation.

The workflow for the training of the robot to recognize weeds in a field with agricultural crops is presented in Fig. 5. The TensorFlow object detection API (Huang, 2017) is used as training platform. The workflow contains four main stages – preparation of the environment, preparation of the datasets, training and then implementation of the object detection model (Fig. 5).

The input dataset is required to contain images that have objects of interest – for the agricultural robot the images must contain different kind of weeds that are often found in the field. To train a good detection model, TensorFlow requires hundreds of thousands of images. However, instead of training a model from scratch, it is possible to retrain a pre-trained neural network model and then use smaller amounts of images. We have used more than 300 photographs of different

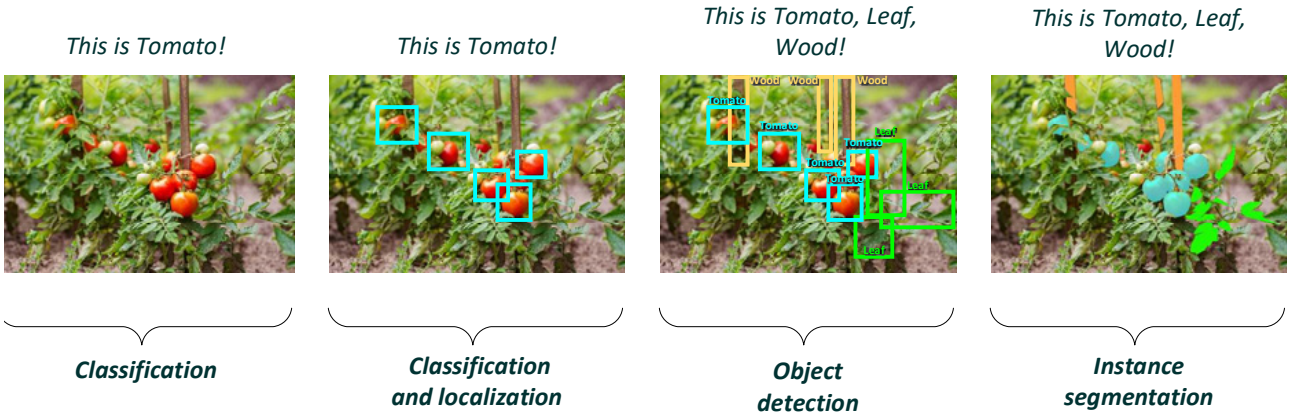


**Fig. 4** Comparison among the classification, localization, object detection and segmentation problems

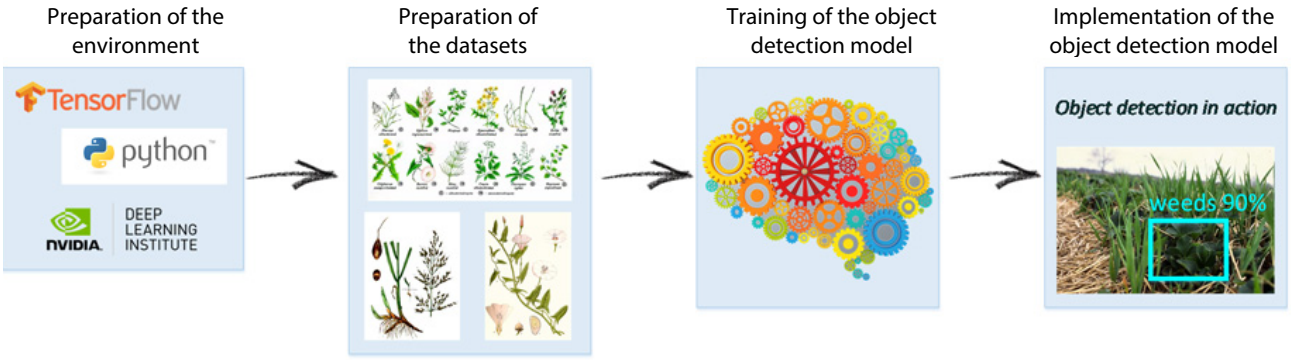


**Fig. 5** Workflow for development of a computer vision solution for weed detection

weeds for the training of our solution. Twenty percent of the images were set aside for testing and to avoid overfitting the model, while the rest were used for the training process, like in Abbaspour-Gilandeh (2019). After collecting the desired number of images, they were labelled to show the classifier where the object of interest resides in the image. As a training model, the Faster R-CNN with Inception version 2 was used. It is available online in the TensorFlow model zoo (TensorFlow object detection zoo, 2017). The Faster R-CNN is canonical model for deep-learning object detection. The time it takes to train the model depends on the number of images, their resolution and the hardware parameters of the computing unit. After the training, the last step in the process is to export the trained model and use it in practice.

In specific situations, the robot might have to implement autonomous tasks that are more complex. To do this, the robot can be configured to navigate on its own and without any predefined routes, but again without damaging the crops. In this case, the goal of the robot is to construct a map of the unknown environment and to localize itself on it. In the computer sciences, this problem is known as the Simultaneous Localization and Mapping (SLAM) problem. It is also considered to be fundamental for the robotics domain and the solution to it allows the robots to become truly autonomous (Bailey and Durrant-Whyte, 2006). SLAM actually combines two problems – the localization problem and the mapping problem, which are easy to solve on their own. Nowadays, it is somewhat simple to create a map that is based on a known position, which is the mapping problem, and it is also relatively easy to obtain your own location within the known map – the localization problem. However, if both problems exist at the same time and if they have to be solved simultaneously, their combination proves to be challenging and complex. Fortunately, there are several known algorithms that can solve the SLAM problem, so the research efforts in this area are concentrated on their improvement in terms of computational efficiency, as well as on the provisioning of consistent and accurate estimate about the map and the position of the robot (Durrant-Whyte and Bailey, 2006).

The most recent scientific efforts to solve the SLAM problem are based on visual methods for positioning, also known as visual odometry. This approach allows the estimation of the location of the robot based on the 3D motion of the camera in space. There are two main ways to implement a visual odometry solution – by single camera (monocular) or by two cameras (stereoscopic). The later calculates the depth by estimating the disparities between the matching key points in the images from both cameras. The visual odometry is a robust technique for autonomous navigation, motion tracking and obstacle detection and avoidance (Cviklovič et al., 2016). It allows a robot to localize itself by using only a stream of images captured by the camera attached to it. For this reason, we have decided to proceed with the implementation of this solution for the developed platform.

## Results and discussion

For the implementation of the computer vision tasks by the developed small-scale agricultural robot, we have used the widely available Raspberry Pi 3 Model B+ microcomputer (Raspberry 3, 2020). It is the core of the top-level hardware layer of the robot (Fig. 1). This specific version of the Raspberry Pi supports several cameras, including the commercially available Raspberry Pi cameras and the more advanced Intel Real Sense Depth and Tracking Cameras.

To detect different colours with the robot, we have developed a custom Python script that allows the detection of a specific predefined colour. For the purpose of the experiment, we have assumed that the red colour is representing the presence of weeds. After their detection, the robot will treat the weeds locally by spraying them with a liquid solution. The running of the programming script requires a pre-installed version of OpenCV. The code that is used for the tests of the computer vision algorithm is expected to recognise only colours. The process of colour recognition requires the conversion of the colour diagram of the images from the camera from RGB (red-green-blue) colour format to HSV (hue-saturation-value) format. The need to convert the colour formats comes from the fact that when describing the RGB colours, the colour components of a given object in the image are related to the amount of light that falls on the object. This significantly obstructs the colour distinction of the objects. On the other hand, the HSV colour system is much better for image description, because it uses hue, saturation and value. The computer vision algorithm that is used by the robot in the evaluation scenario is presented in the block diagram below (Fig. 6).

The algorithm is set to recognize two colours – red and green, which are very common for the agricultural

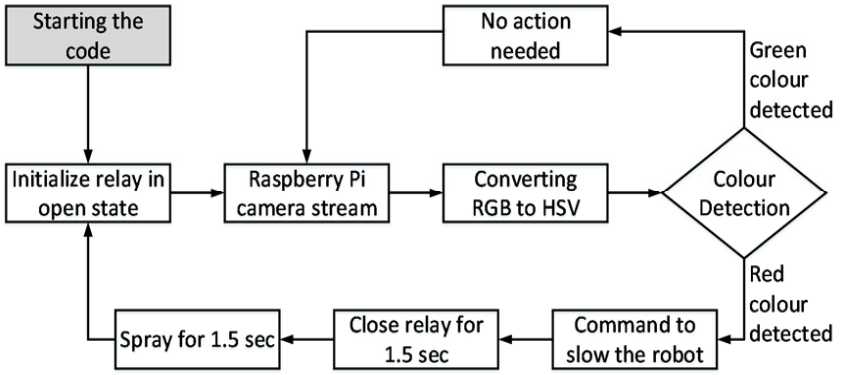


**Fig. 6** Block scheme of the algorithm used for the colour detection experiment

processes. The green colour represents fresh leaves and healthy plants, while the red colour signalizes for damaged plants. The boundaries for both colours are defined in the code with small tolerance thresholds. This allows the computer vision algorithm to recognise several different shades of colours.

The detection of the red and green colours in the images requires the comparison of the values of the image pixels with the pre-defined values. If the algorithm detects the green colour or any other colour except red, no actions are invoked, and the algorithm continues to compare the other pixel values of the image. If the red colour is detected, the setAngle function is executed. With this function, a low-level signal is sent to the electrical relay switch of the robot. The duration of the signal is just 1.5 seconds and during this low-level signal, the relay is closed, which activates the motor of the sprinklers and the spraying starts. Once the 1.5 seconds have elapsed, a high-level signal is sent to the relay, which causes the spraying to stop. The duration of the process is defined in correlation to the robot speed of 12 km·h$^{-1}$.

For our experiments, the Mission Planer software is used to make the robot navigation autonomous. This application allows the user to predefine a specific route that the robot will follow using its GPS navigation system. Once the predefined mission is uploaded to the robot, it can navigate itself along the field and can follow the planned route. During the mission, the computer vision algorithm is running constantly on the robot. Fig. 7 presents the conducted experiments – from the route planning, through the detection of the objects and then the spraying of the targeted area. Fig. 7 also presents two images with the real-time video feed from the robot and it is visible how the computer vision system of the robot has detected the green colour in the video feed (the green bench on the left), as well as the red target (red square on the right). The middle image displays the robot in the moment of spraying of the target. The experiments were conducted with a red square target with size of 20 cm × 20 cm. More than fifty tests were conducted with the speed of the robot ranging between 10 and 15 km·h$^{-1}$ and the distance to the target being changed from 10 to 60 cm. All tests were successful, and the robot was able to detect the red target and execute the spraying process.

To provide the robot with the capability to solve the SLAM problem and navigate autonomously in an unknown environment or in an environment with no or poor GPS coverage, we have developed a visual navigation solution that is based on the Intel® RealSense™ Depth Camera D435i (D435i Depth Camera,

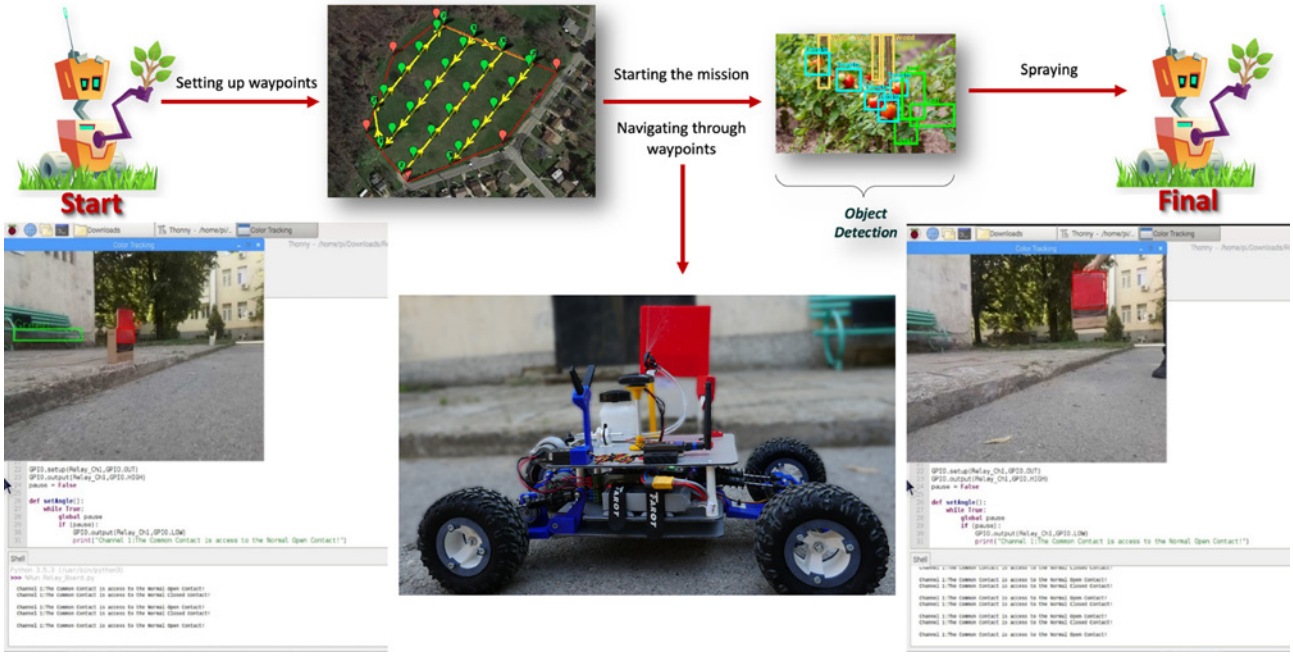


**Fig. 7** Detection of green (left) and red objects (left and right) during the experiments

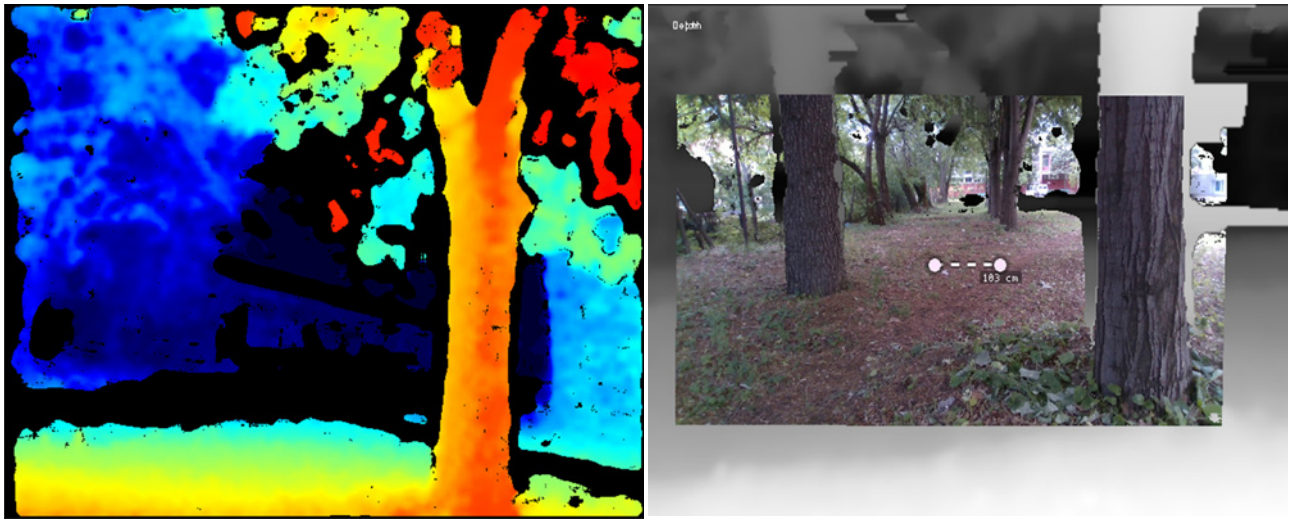


**Fig. 8** Obstacle detection and avoidance using the visual navigation solution

2020) in combination with the Intel® RealSense™ Tracking Camera T265 (T265 Tracking Camera, 2020) and the Intel® RealSense™ LiDAR Camera L515 (L515 LiDAR Camera, 2020). The use of these cameras (Fig. 8) eliminates the need for a GPS system, which otherwise is used by the robot for navigation. Being able to construct the route and not following the navigation instructions provided by the Mission planer software makes the robot fully autonomous.

Figure 8 shows how the depth camera can help the robot navigate. It shows in colour (Fig. 8 left) the distance to the objects in the field of view of the robot. In this way, the robot can move towards the farthest object to avoid any obstacles along the way. In addition, the camera gives the robot the capability to calculate the width between the objects (Fig. 8 right). The robot is also capable of providing a feedback that contains information about the distance to the object (Fig. 9). The robot is able to cope with clods of earth and bumps along its way, as well as to move from row to row without damaging the plants. To avoid any obstacles, the robot will stop moving when an object is detected at a predefined distance, for example at 50 cm.

Another benefit of the visual navigation system is the fact that the robot can track the rows of crops in the field completely autonomously, as it can be noticed by the results shown in Fig. 10. By using this capability, the robot can create a map of the area and save it for future missions.

As the visual navigation solution is not based on the GPS location data, the robot creates its own relative coordinate system and stores its initial position. The map of the agricultural field is then created based on this initial position. The self-localization of the robot is performed by its current coordinates, which are relative to its initial position (Fig. 11) and in this way the robot can return back to its initial point of departure. The robot is also in constant communication with its control station and can send periodic messages about its position (Fig. 11), which allows the user to remotely track it in the field.

```
The camera is facing an object 11.226 meters away
```

**Fig. 9** Obstacle avoidance notification

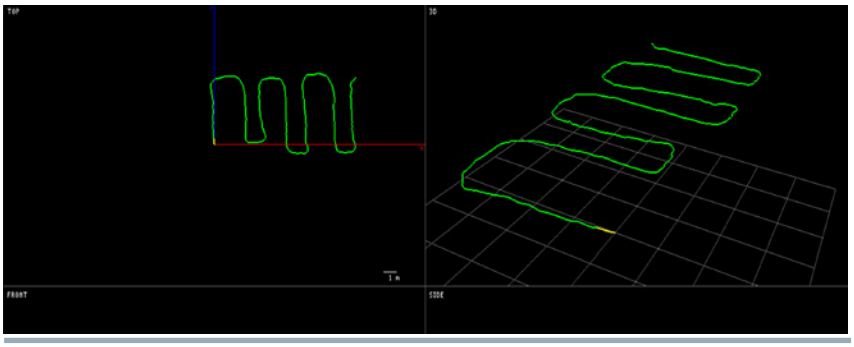

**Fig. 10** The capability of the robot to track and map its own route

```
Device Position: 0.497 -0.286 -1.540 (meters)
```

**Fig. 11** Information on the current position of the robot in a relative 3D coordinate system

## Conclusion

Artificial Intelligence, Computer Vision and Robotics are among the technologies that are redefining our everyday live. Their potential is huge and they are slowly being introduced in areas where it was considered to be impossible to do so. In the precision agriculture domain, these technologies have been used for several decades, but with the recent technological advances, they have proven to be more reliable, more flexible and more

adaptive to the requirements and needs of the sector. To confirm this assumption, in the paper we have presented a prototype of a small-scale agricultural robot for precision farming. The developed prototype is in its early evaluation stage, but so far it has managed to surpass all expectations and has proven to be able to perform the basic tasks it was envisioned to do. Based on this, we can state that it is possible to develop small-scale inexpensive solutions for precision farming, based on the current information and communication technologies. The robot presented in this paper cannot fully replace the expensive commercial solutions, but can be a supplementary to them and is suitable for use both outdoors and indoors, as well as on rooftops and in urban areas. This robot also has off-road capabilities due to its high clearance and is suitable for use in farm fields. In the upcoming months, the robot will be further tested and evaluated in controlled and real environments. It will also be upgraded to perform actions that are more advanced, like weed removal, etc. The robot will also be equipped and tested to operate with manipulators, like arms, which will allow it to harvest small fruits and vegetables.

**Acknowledgment**

This publication is developed with the support of Project BG05M2OP001-1.001-0004 UNITe, funded under Operational Programme "Science and Education for Smart Growth", co-funded by the European Union trough the European Structural and Investment Funds.

The work presented in this paper is completed as partial fulfilment of Project 2020 – FEEA – 03 "Design and Development of a Multifunctional Robot for Implementation and Evaluation of Autonomous Navigation Algorithms", financed under the Scientific and Research Fund of the University of Ruse "Angel Kanchev".

## References

123D DESIGN, 2020. Official website available at: https://www.autodesk.com/solutions/123d-apps

ABBASPOUR-GILANDEH, Y. – ABBASPOUR-GILANDEH, M. 2019. Application of computational intelligence methods for predicting soil strength. In Acta Technologica Agriculturae, vol. 22, no. 3, pp. 80–85.

AMER, G. – MUDASSIR, S. M. M. – MALIK, M. A. 2015. Design and operation of Wi-Fi agribot integrated system. In IEEE International Conference on Industrial Instrumentation and Control, pp. 207–212. ISBN 978-1-4799-7165-7.

BAILEY, T. – DURRANT-WHYTE, H. 2006. Simultaneous localization and mapping (SLAM): Part II. In IEEE Robotics & Automation Magazine, vol. 13, no. 3, pp. 108–117.

BAKKER, T. – ASSELT, K. – BONTSEMA, J. – MULLER, J. – VAN STRATEN, G. 2010. A path following algorithm for mobile robots. In Autonomous Robots, vol. 29, pp. 85–97.

BELFORTE, G. – DEBOLI, R. – GAY, P. – PICCAROLO, P. – RICAUDA AIMONINO, D. 2006. Robot design and testing for greenhouse applications. In Biosystems Engineering, vol. 95, no. 3, pp. 309–321.

CHEEIN, F. A. A. – CARELLI, R. 2013. Agriculture robotics: Unmanned robotic service units in agriculture tasks. In IEEE Industrial Electronics Magazine, vol. 7, no. 3, pp. 48–58.

CLAAS 700. 2020. Official website of the Claas 700 series combiners available at: https://www.claas.co.uk/products/combines/lexion780-740-2018

CLAAS ISARIA. 2020. Official website of the CLAAS ISARIA crops sensor available at: https://www.claas-group.com/press-corporate-communications/press-releases/the-highly-proficient-optical-plant-sensor-from-claas/304426

COSGROVE, E. 2017. The state of play for farm robotics. Article available at: https://agfundernews.com/farm-robotics-startups.html

CVIKLOVIČ, V. – OLEJÁR, M. – HRUBÝ, D. – PALKOVÁ, Z. – LUKÁČ, O. – HLAVÁČ, P. 2016. Navigation algorithm using fuzzy control method in mobile robotics. In Acta Technologica Agriculturae, vol. 19, no. 1, pp. 19–23.

D435i DEPTH CAMERA. 2020. Technical data available at: https://www.intelrealsense.com/depth-camera-d435i/

DJI AGRAS T16. 2020. Official website available at: https://www.dji.com/bg/t16

DURRANT-WHYTE, H. – BAILEY, T. 2006. Simultaneous localization and mapping: Part I. In IEEE Robotics & Automation Magazine, vol. 13, no. 2, pp. 99–110.

FARMAID. 2020. Official Farmaid project page available at: https://www.hackster.io/teamato/farmaid-plant-disease-detection-robot-55eeb1

FENDT. 2020. Official company website available at: https://www.fendt.com

HERNÁNDEZ, J. D. – BARRIENTOS, J. – DEL CERRO, J. – BARRIENTOS, A. – SANZ, A. 2013. Moisture measurement in crops using spherical robots. In Industrial Robot, vol. 40, no. 1, pp. 59–66.

HRISTOV, G. – ZAHARIEV, P. – BELOEV, I. 2016. A review of the characteristics of modern unmanned aerial vehicles. In Acta Technologica Agriculturae, vol. 19, no. 2, p. 33–38.

HUANG, J. 2017. TensorFlow object detection api, available at: https://github.com/tensorflow/models/tree/master/research/object_detection

JOHN DEERE. 2020. Official website available at: https://www.deere.com/en/agriculture

KRASTEV, G. – GEORGIEV, T. 2015. A prototype of autonomous mobile robot. In European Science and Technology – Materials of the X International Research and Practice Conference, vol. II, Munich, Germany, Vela Verlag Waldkraiburg, pp. 310–314. ISBN 978-3-941352-46-9.

L515 LiDAR CAMERA. 2020. Technical data available at: https://www.intelrealsense.com/lidar-camera-l515/

PIERPAOLI, E. – CARLI, G. – PIGNATTI, E. – CANAVARI, M. 2013. Drivers of precision agriculture technologies adoption: A literature review. In Procedia Technology, vol. 8, pp. 61–69.

RASPBERRY 3. 2020. Official website of the Raspberry 3 Model B+ at the Raspberry Pi Foundation, available at: https://www.raspberrypi.org/products/raspberry-pi-3-model-b-plus/

T265 TRACKING CAMERA. 2020. Technical data available at: https://www.intelrealsense.com/tracking-camera-t265/

TENSORFLOW OBJECT DETECTION ZOO. 2017. TensorFlow object detection zoo. Available at: https://github.com/tensorflow/models/blob/master/research/object_detection/g3doc/tf1_detection_zoo.md

YAGHOUBI, S. – AKBARZADEH, N. A. – BAZARGANI, S. S. – BAZARGANI, S. S. – BAMIZAN, M. – ASL, M. I. 2013. Autonomous robots for agricultural tasks and farm assignment and future trends in agro robots. In International Journal of Mechanical & Mechatronics Engineering, vol. 13, no. 3, pp. 1–6.